EXPERIMENTAL INVESTIGATION AND MODELLING OF MAGNETO RHEOLOGICAL ELASTOMER FOR TORSIONAL VIBRATION ISOLATION

Thesis

Submitted in partial fulfillment of the requirements for the Degree of

DOCTOR OF PHILOSOPHY

by

PRAVEEN SHENOY K

DEPARTMENT OF MECHANICAL ENGINEERING

NATIONAL INSTITUTE OF TECHNOLOGY KARNATAKA

SURATHKAL, MANGALORE – 575025

MARCH, 2021

DECLARATION

I hereby declare that the Research thesis entitled **"EXPERIMENTAL INVESTIGATION AND MODELLING OF MAGNETO RHEOLOGICAL ELASTOMER FOR TORSIONAL VIBRATION ISOLATION"** which is being submitted to the **National Institute of Technology Karnataka, Surathkal** in partial fulfillment of the requirements for the award of the Degree of **Doctor of Philosophy** in the **Department of Mechanical Engineering** is a *bonafide report of the research work carried out by me*. The material contained in this Research thesis has not been submitted to any other Universities or Institutes for the award of any degree.

Register Number: **145052ME14F12**

Name of the Research Scholar: **PRAVEEN SHENOY K**

Signature of the Research Scholar:

Department of Mechanical Engineering
National Institute of Technology Karnataka Surathkal

Place: NITK-Surathkal
Date: 26/03/2021

CERTIFICATE

This is to certify that the Research synopsis entitled **"EXPERIMENTAL INVESTIGATION AND MODELLING OF MAGNETO RHEOLOGICAL ELASTOMER FOR TORSIONAL VIBRATION ISOLATION"** submitted by **Mr. PRAVEEN SHENOY K (Register Number: 145052ME14F12)** as the record of the research work carried out by him, *is accepted as the Research thesis submission* in partial fulfillment of the requirements for the award of the Degree of **Doctor of Philosophy.**

Prof. K V GANGADHARAN
Research Guide
Date:

Department of Mechanical Engineering
National Institute of Technology Karnataka Surathkal

Chairman-DRPC

Date: 26 MAR 2021

ACKNOWLEDGEMENTS

It gives me immense pleasure and honor to express my sincere gratitude to my Mentor and supervisor, **Prof. K V Gangadharan**, Professor, Department of Mechanical Engineering, National Institute of Technology Karnataka, Surathkal. He is the perfect role model of the term *"Guru"*, who guided me not only with the technical stuff but also on the general aspects of being a humble being. From being a newbie in the area of experiments to somewhat improved by a delta value, he allowed me to realize my flaws (*Both technical and others*) on my own, giving me the necessary *"Hints"* all along the way. While I was allowed to explore as much as possible, I still remember his words that he would always be there for me whenever I would tumble on my path, be it research or otherwise. I can surely say that his exemplary guidance, inspiration and constructive criticism during research work will always stay with all of his students. One quote which I will always try to abide: *"We have thousands of reasons for not doing our work. Let us find one reason to do it"*

I wish to express my sincere gratitude to **Prof. S.M.Kulkarni** , Head, Department of Mechanical Engineering, and all former HOD's, faculty members, technical and administrative staff of the Department of Mechanical Engineering, National Institute of Technology Karnataka, Surathkal for their kind help in providing the facilities as and when needed.

I sincerely thank my thesis reviewers, **Prof. Kantesh Balani**, Professor, Dept. of Material science Engineering, IIT Kanpur, and **Prof. S.K. Dwivedy**, Professor, Dept. of Mechanical Engineering, IIT Guwahati for taking their precious time and effort in reviewing my thesis. Also I would like to thank my DTAC members, **Dr. Jeyeraj P**, Associate Professor, Dept. of Mechanical Engineering and **Prof. Krishna Bhat**, Professor, Dept. of Chemistry and my RPAC members, **Dr. Hemantha Kumar**, Associate Professor, Department of Mechanical Engineering, National Institute of Technology Karnataka, Surathkal and **Prof**. **Anandhan Srinivasan**, Professor, Department of Metallurgical and Materials Engineering, National Institute of Technology Karnataka, Surathkal for providing valuable suggestions.

They say that good research community not only consist of a good mentor, but also team members who always strive for the success of each other. In this aspect, I am

incredibly thankful and ever grateful to **Dr. Umanath Poojary** and **Mr. SusheelKumar** for their everlasting support in the journey of uncertainties. If the former provided me with the necessary launch pad and the timely help with the experimental setup and proofreading, the latter was instrumental in being there at all my times, discussing everything, from concepts to fully fledged discussions on the technical aspects. Both of them provided the necessary critiques at the required instances, which helped me to elucidate my objectives.

I wish to thank all the **Centre for System Design (CSD) members** for their constant help and encouragement during research work. I also wish to thank my friends **Mr. Sai Aditya RK, Mr. Kiran Anginthaya, Mr. Anarghya Murthy, Mr. Rohit Rajpal, Mr. Subhasankar D, Mr. Praveen Kumar, Mr. Ashish D, Mr. Abhay K, Dr. Gururaj Udupa, Mr. Kiran Katari, Mr. Balanarasima G, Mr. Mallikarjuna Balichakra, Mr. Ravikumar, Dr. Gurubasavaraj TM, ,** from the Department of Mechanical Engineering and **Dr. SriHarsha Hegde** from MIT, Manipal for their everlasting support at various stages of my research work. Also, thanks are due to my professors who taught me during my course work at the Mechanical Engineering dept., and to the members of the Machine shop and M/s Stamina Engineering and Boring works for their help in the fabrication of the setup. Thanks are also due to M/s Crystal Refrigerator works for the timely help with the Electromagnet.

I thank **Mr. Jayaram Thumbe**, who has inspired me right from my graduate days of engineering. He always gave me the necessary guidance at significant instances along the way. In fact, he was the one who kindled my interest towards the field of experimentation.

I am thankful to the **Director and administration** of the National Institute of Technology Karnataka, Surathkal, for providing all the necessary facilities and funds to carry out my research work.

Finally, I would like to thank my **family members** for their undying love, encouragement and support throughout my life and education.

(**PRAVEEN SHENOY K**)

Abstract

Torsional vibration isolation is an effective method to mitigate unwanted disturbances arising from dynamic loading conditions. Typically this is achieved with conventional passive isolators such as centrifugal pendulum absorbers, torsion springs, sprocket dampers, fluid cased vibration dampers and others. A drawback of the existing passive isolators is the inability to tune themselves to varying operating conditions. With smart materials as suitable substitutes, the conventional passive systems have attained attributes of semi-active and active control isolators. Of the various available smart materials, the Magnetorheological Elastomers (MRE) offers a field-dependent property variation for variable operating parameters. Though the MRE has been effectively studied to isolate the structures in the linear/translatory systems, its capabilities as an effective torsiocal isolator are yet to be understood fully. In lieu of the same, in the present study, Magnetorheological Elastomers' attributes as an effective torsional vibration isolator have been explored.

To comprehend the isolation capabilities of Magnetorheological Elastomers, a thorough understanding of the influencing parameters is necessary. Hence, the initial part of the current study focuses on the dynamic property characterization of the Magnetorheological Elastomers under torsional loading conditions. The dynamic properties of Magnetorheological Elastomers are predominantly affected by variation in the input displacements, applied magnetic fields and input frequency. Though the characteristics have been extensively studied under lateral shear, the property variations under torsional shear have not been explored. The present study develops a novel method to study the influence of angular displacement, applied magnetic fields and input frequency on the dynamic properties of Magnetorheological Elastomers under torsional loading conditions. The experimental setup is developed according to the ISO 10846-2 standard to evaluate the dynamic torsional stiffness and loss factor variations. Viscoelastic properties represented in-terms of complex torsional stiffness and loss factor are estimated from the Lissajous curves within the linear viscoelastic (LVE) limit. Experiments are conducted for varying input angular displacements (in the Linear Viscoelastic limit) and input frequency (in the range of 10Hz to 30Hz). The frequency range corresponds to the torsional frequency range of shafts rotating in the lower speed

range under 2000 rpm. Magnetic field sensitive characteristics are evaluated under the field produced by a custom-made electromagnet in the range of 0T to 0.3T. The volume fraction of the CIP is set at 27% for the RTV based isotropic MRE.

The results reveal a strong influence of field-dependent variations on the complex stiffness compared to the input frequency. Variations observed in the loss factor suggest a dominance of the imaginary part of the complex stiffness on the energy dissipation. The reduced field-induced enhancements in the complex stiffness are interpreted from the Magneto-static and structural based numerical simulations using ANSYS 19.1. The angular displacement dependent variations highlight the effectiveness of the developed method in capturing the rheological properties under torsion. Changes in the dynamic torsional stiffness suggest the dominant behaviour of the input angular displacement. The bound rubber theory is used to interpret the displacement-dependent variations on the torsional stiffness. It is also observed that the MRE's damping capacity depends on the angular displacement and the dissipation capacity of the elastomer is evaluated in terms of loss factor. Results indicate a significant contribution of the interfacial damping over the intrinsic and magneto-mechanical hysteresis damping.

To formulate the actual implementation of the MRE as a semi-active isolator, it is required to model the complex behaviour of the MRE through its stiffness and damping. Though much research has been carried out in understanding MR fluids' behavior, the same cammt be said of its elastomer counterparts. The constitutive relationship between the operating parameters is derived using a viscoelastic parametric modelling technique based on the Kelvin-Voight model. Results highlight the derived model's effectiveness in predicting the experimentally obtained viscoelastic behaviour of the Magnetorheological Elastomers regarding the stiffness and the energy dissipation capacity.

To evaluate the Magnetorheological Elastomer isolator's isolation capabilities, a novel, custom-made SDoF torsional isolation system is developed. Field-dependent reduction in the transmissibility ratio highlights the semi-active vibration capabilities of the isolator and a maximum reduction of 42% is observed in the transmitted amplitudes. Further, a shift in the natural frequency is detected due to the field-induced

variations in the isolator's torsional stiffness. The isolation capabilities are calculated for different input angular displacements, inertia and magnetic fields and the effect of the individual parameters is studied. The torsional stiffness and the damping factor are ascertained individually for the individual parameters. Also, a model-based PID control strategy is adopted to assess the semi-active vibration capabilities of the Magnetorheological Elastomer isolator.

Table of Contents

List of Figures

List of Tables

Acronyms

MRE : Magnetorheological Elastomer

MRF : Magnetorheological Fluid

SDoF : Single Degree of Freedom

PID : Proportional Integral Derivative

CIP : Carbonyl Iron Particles

HTV : High Temperature Vulcanized

RTV : Room Temperature Vulcanized

CNT : Carbon Nano tubes

DMA : Dynamic Mechanical Analyser

ISO : International Standard Organization

DVA : Dynamic Vibration Analyser

ATVA : Adaptive Tuneable Vibration Absorber

SLS : Standard Linear Solid

FEMM: Finite Element Method Magnetics

SEM : Scanning Electron Microscope

SAA : Serial Arrangement of Accelerometers

PAA : Parallel Arrangement of Accelerometers

Nomenclature

K_t^*	Complex Stiffness (N.m rad^{-1})
K'	Real part of the Complex Stiffness (stiffness term) (N.m rad^{-1})
$K^{"}$	Imaginary part Complex Stiffness (energy dissipating term) (N.m rad^{-1})
K^*_{t5}	Complex Stiffness corresponding to $5A$ (N.m rad^{-1})
K^*_{t0}	Complex Stiffness corresponding to $0A$ (N.m rad^{-1})
$K^*_{t(30Hz)}$	Complex Stiffness corresponding to $30Hz$ (N.m rad^{-1})
$K^*_{t(10\mathrm{Hz})}$	Complex Stiffness corresponding to $10Hz$ (N.m rad^{-1})
T_0	Amplitude of torque (N.m)
$T_{out}(t)$	Output Torque (N.m)
θ_0	Amplitude of angular displacement (rad)
$\theta(t)$	Input angular displacement (rad)
ω	Operating Frequency (rad. sec^{-1})
φ	Phase Angle (rad)
η	Loss factor
T_a	Positive torque at the maximum positive angular displacement (N.m)
T_b	Torque at zero angular displacement (N.m)
E_{12}	Interaction energy between two iron particles (N.m)
μ_0	Permeability of the vacuum (H.m^{-1})
μ_1	Relative permeability of the elastomer
$m_1 m_2$	Dipole moment of the two iron particles (A.m^2)
r_0	Separation distance between the two particles without the presence of field (mm)
r	Separation distance between the two particles with the presence of field (mm)
R	Particle radius (mm)
F	Force between the two particles (N)
α'	Angle between the displaced position with the un-displaced position of the CIP
C	1.2
t_h	Elastomer sample thickness (mm)
r_s	elastomer sample radius (mm)

G'	shear modulus of bound rubber (MPa)
G_0	zero-field shear modulus (MPa)
R	radius of the CIP (mm)
t	thickness of the bound rubber (mm)
ϕ	volume fraction of the particles
w	Power coefficient
D_C	Intrinsic damping capacity
D_m	damping ratio of the matrix
D_s	interfacial damping capacity
D_{mf}	magneto-mechanical damping
D	total damping capacity
ν	Poisson's ratio of the matrix material
K	coefficient which defines the number of interfaces which reach the critical strain value during the movement
f	friction force between the CIP and the matrix (N)
ξ	stress coefficient (i.e., the ratio of the applied stress to the developed normal stress
ϵ_0	applied strain
α	change of elastic modulus with the external strain (MPa)
$E(B)$	field-dependent elastic modulus (MPa)
E_s	interfacial damping energy (N.m)
n	the number of carbonyl iron particles in a given unit volume of the MRE
s	relative displacement occurring between the surfaces of CIP and polymer chains (mm)
$T_{KV}(t)$	total torque experienced by the elements of the Kelvin-Voight Model (N.m)
$K_1\ K_2\ K_3$	torsional stiffness element of the modified Poynting Thomson model (N.m rad^{-1})
$C_2\ C_3$	damping constant element of the Kelvin-Voight Model (kg.m^{2}rad^{-1}sec^{-1})
T_{fd}	torque acting on the spring-pot (N.m)
$c,\ \alpha$	fractional parameters
$K_{KV}{}^*$	complex stiffness for the Kelvin-Voight model (N.m rad^{-1})
$K_{pt}{}^*$	complex stiffness for Poynting Thomson model (N.m rad^{-1})

A	objective function
$T_{mdi}(t)$	model-predicted torque values (N.m)
$T_{exi}(t)$	experimentally obtained torque values (N.m)
S_{ij}	harmonic response in SAA measurement
$\theta_{ri}\theta_{rj}$	the angular displacement values for SAA
T_j	harmonic torque (N.m)
η'	frequency ratio
ζ	damping ratio
γ	output angular displacement (rad)
Ω_r	torsional natural frequency (rad.sec^{-1})
T_{0T}	the transmissibility of the system
T_{mb}	Transmissibility of the system at a given field corresponding to the base frequency
J_b	Inertia of the base (kg.m^2)
$\theta_b, \ddot{\theta}_b, \dot{\theta_b}$	Angular Displacement, velocity and acceleration of base
k_{tb}	Torsional Stiffness of the base (N.m rad^{-1})
k_{ti}	Torsional Stiffness of the isolator (N.m rad^{-1})
$\theta_i, \ddot{\theta}_i, \dot{\theta}_i$	Angular Displacement, velocity and acceleration of the SDoF system
J_i	Inertia of the SDoF system (kg.m^2)

1. Introduction

1.1. Dynamics of Rotating systems

Rotating members are susceptible to torsional vibrations originating from various forces like asymmetric defects, gyroscopic effects, internal damping and forces inherent within the system. These vibrations are often seen as a cause for concern in power transmission systems and may lead to severe damage or failure under uncontrolled conditions. Rotatory elements often experience torsional vibrations to variable degrees, either during start-up, shutdown or even during continuous operation (Ran et al. 1996). The severity of these vibrations is minimum under a shorter dwell time in the resonance region. However, exposure to a sustained interval of time may lead to catastrophic failure of the rotating shafts. Hence, to ensure the reliability and safety of rotating systems, it is crucial to analyze their response characteristics and employ effective vibration attenuation techniques.

Conventional approaches employed for vibration mitigation in dynamic systems are either through the vibration absorbers (Yao et al. 2018)(Gao et al. 2018) or the vibration isolators (Rao 2010)(Leng et al. 2018). Vibration absorbers (Figure 1-1, a) work on the principle of adding a secondary spring-mass unit to the primary system. The natural frequency of the secondary system is designed to coincide and resonate with the excitation frequency resulting in the reduction of vibration of the primary system

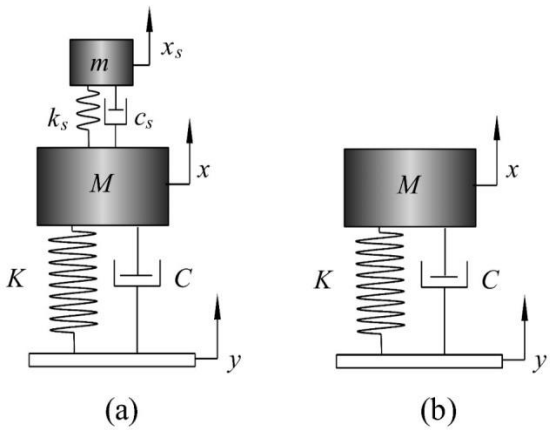

Figure 1-1: Schematic of vibration attenuation techniques (a) Absorber (b) Isolator

vibration isolation (Figure 1-1, b) mitigates the vibration by decoupling the vibration source from the primary structures. To achieve these mitigations, isolators generally employ resilient members (viscoelastic mounts) or isolators (metal springs) between the source of vibration and the system of interest. In practice, vibration isolation can be achieved by active, passive or semi-active methods. Passive vibration isolation Figure 1-1 is relatively simpler from the economic and maintenance point of view. However, it fails to function effectively for systems subjected to broader frequency ranges. Active isolators overcome these issues by providing a feedback force to the primary system through an actuation unit. Nevertheless, due to the bulky nature and relatively higher sophistication, they are prevalent only within a limited branch of dynamics. Semi-active isolation forms a potential approach to overcome the above limitations. The ability to change its mechanical properties under the influence of an external force makes the Semi-active isolation process more suitable for dynamic systems.

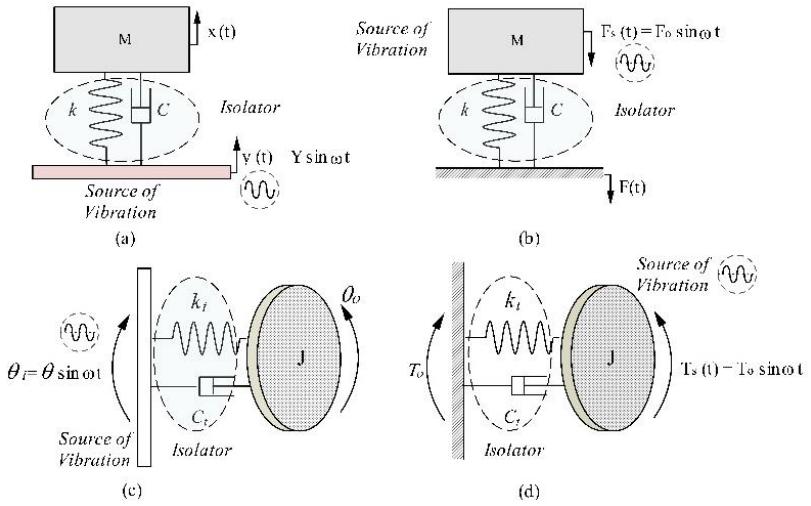

Figure 1-2: SDOF passive isolator system

1.2. Principle of Semi-Active Vibrations control

Traditional springs and rubber isolators mitigate the vibrations of a dynamic system over a fixed range of frequencies. Properties of these isolators are fixed and thus, they cannot be tuned under varying dynamic working conditions. This limits their applications in actual applications. The passive nature of the isolators is illustrated using a Single Degree of Freedom (SDoF) torsional isolation system. For a system with a

shaft of stiffness k_t and damping coefficient, c with a rotor of inertia J, the (Figure 1-1) equation of motion is given as

$$J\ddot{\theta} + c\dot{\theta} + k_t\theta = k_t\theta_1 + c\dot{\theta_1} \tag{1.1}$$

θ and θ_1 be the angular displacements seen at the rotor end and the base, respectively, $\ddot{\theta}$ and $\ddot{\theta}_1$ be the angular acceleration at the rotor end and the base.

For a harmonic input, the angular displacements are given as,

$$\theta = \theta_0 sin\omega t;$$

$$\theta_1 = \theta_{10} sin\omega t$$

where θ_0 and θ_{10} are the amplitudes of angular displacements with ω the operating frequency of the system. The amount of angular displacement transmitted is expressed in terms of the displacement transmissibility (Ratio of transmitted displacement to the input displacement) and is given as

$$\frac{\theta_0}{\theta_{10}} = \frac{k_t + j\omega c}{k_t - J\omega^2 + j\omega c} \tag{1.2}$$

The response plot for the SDoF system is shown in Figure 1-3. Curve-1 represents the frequency response of the system with the passive isolator, and ω_1 is the torsional natural frequency of the system. Correspondingly, the operating frequency range can be selected from the transmissibility curve. The response of the system is unaffected until the natural frequency of the system remains unchanged. However, if the stiffness of the system changes, the natural frequency shifts to a newer value (represented as ω_2). The passive isolator, designed for the frequency ω_1, fails to adapt to the change which renders it ineffective.

The adaptiveness to varying frequencies is achieved by employing semi-active vibration isolators. Corresponding to the variations in the frequencies, the semi-active isolators tune themselves with the application of a force. Hence, isolators, whose rheological properties could be altered, are extremely necessary to subdue the excessive vibrations in dynamic systems. This has resulted in the popularity of smart materials, viz. materials capable of varying their inherent properties.

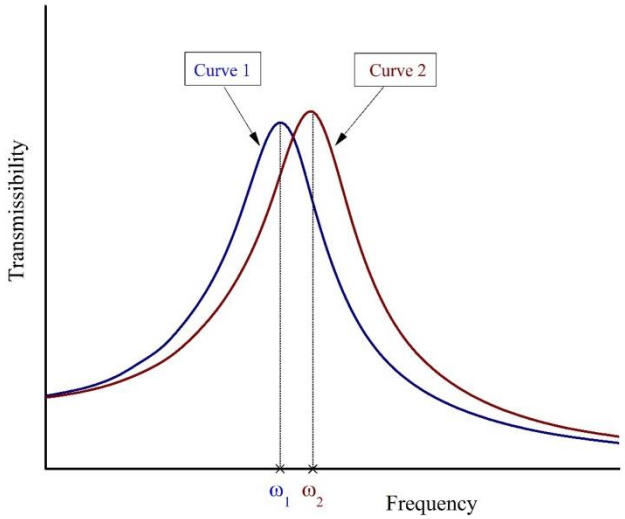

Figure 1-3: Transmissibility curves for varying frequencies

1.3. Magnetorheological Elastomer

As seen in the previous section, under varying dynamic conditions, the passive isolation system has lesser advantages to its inherent drawback. Thus, there is a need for isolation materials to have variable properties to accommodate for changing working conditions. Among the available smart materials, Magnetorheological Elastomer forms one of the potential replacement for the conventional isolators due to its magnetic field dependent rheological properties.

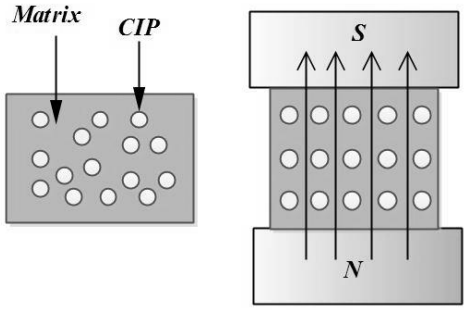

Figure 1-4. Magnetorheological elastomer without and with the magnetic field

Magnetorheological Elastomers or MRE (Figure 1-4) are viscoelastic based composites whose dynamic properties can be controlled quickly, continuously and reversibly under the influence of a magnetic field. Similar to the Magnetorheological Fluids (MRF), the MRE consists of a non-magnetic viscoelastic base (in lieu of carrier fluid) in which micron to nano-sized iron particles are embedded during the curing process (Rigbi and

Jilkén 1983). MRE offers several advantages over its fluid counterpart, predominantly the absence of sedimentation issues, reduction in environmental contamination, and leakage due to sealing issues(Dong et al. 2009)(Yang et al. 2015). On the flip side, MRE requires a higher magnetic field (at about 0.2 to 0.3 T) intensity to affect the viscoelastic properties substantially.

A typical MRE contains microsized to nanosized magnetic particles (Usually Carbonyl iron particles (CIP)) distributed in elastomers where the particles form chainlike structures within the polymer matrix during the process of curing. Under the influence of an external magnetic field, the particles get aligned in the direction of the applied field, resulting in the formation of interaction forces between the constituent particles. When the MRE is deformed, these constituent forces resist the deformation, suggesting the increase in the complex stiffness of the MRE (Lu et al. 2018).

This field-dependent property of the MRE makes it one of the potential dampers with variable complex stiffness for the semi-active vibration attenuation. Apart from the influence of an external magnetic field, the isolation capabilities of the MRE depend on several factors such as particle size, the volume percentage of the constituent members, operating frequency and strain amplitude. In the present study, an attempt is made to understand the torsional shear properties of the MRE and its role as an effective isolator for torsional vibrations.

1.4. Theses Outline

The present chapter presented a brief overview of the requirement of semi-active based vibration attenuators with an outline to Magnetorheological elastomer. The second chapter highlights the available work in dynamic characterization procedures, modeling and the MRE based vibration attenuation techniques. For the successful implementation of the MRE isolator, it is extremely important to comprehend the effect of various operating parameters on the viscoelastic behavior of the MR elastomer; Chapter 3 presents a detailed methodology for the dynamic characterization of the Magnetorheological elastomer-based isolator under torsional loading conditions. The succeeding chapters discuss the results of the dynamic characterization and the application of the Magnetorheological elastomer isolator. Chapter 4 assesses the influence of the magnetic field and frequency on the torsional complex stiffness and

loss factor of the elastomer. The influence of the angular displacement on the rheological properties of the isolator is elaborated and discussed in chapter 5. Chapter 6 features the fractional derivative-based phenomenological modeling technique for the Poynting Thomson model. The constitutive relationship between the parameters is discussed. Chapter 7 describes the application of the elastomer in isolating the torsional vibrations for a SDoF torsional system. The detailed methodology of constructing a SDoF torsional isolator is discussed, followed by the effect of inertia, displacement and field on the isolation capabilities of the Magnetorheological elastomer is addressed. Chapter 8 explores developing a model-based PID control strategy for the Magnetorheological elastomer-based torsional isolation system. Chapter 9 provides a summary of the work and suggestions for carrying out future research in the field

2. Literature Survey

2.1. Introduction

As briefly outlined in the previous chapter, torsional vibration attenuation forms one of the most important aspects of a rotating system. Various types of passive attenuators are in use to control the excessive amplitudes of vibration, which work efficiently well for a defined range of frequencies but fail otherwise. The passive nature in the isolation system is addressed using semi-active isolators such as Shape memory alloys, Piezoelectric materials, Electrorheological materials, and Magnetorheological materials capable of changing the inherent properties of the system under the influence of external stimuli.

Shape alloys are versatile, however the nonlinearity of the relationship of the stiffness and temperature complexes the control of the natural frequency and limits its usage. (Sun et al. 2015a). The principle of piezoelectric actuator is the inverse piezoelectric effect.(Bazinenkov and Mikhailov 2015). The advantages are low positioning error and a small response time. it has a small load capacity with a small range of motion. Magnetorheological Elastomer (MRE) has been researched extensively in semi-active vibration attenuation.

To comprehend the underlying factors that make MRE a potential vibration attenuator, understanding the rheological properties under various operating parameters needs to be addressed. The present chapter revisits past literature and gives an overview of the work carried out in the dynamic characterization, modeling and applications of the Magnetorheological Elastomers in vibration attenuation. Initial discussions focus on the constituent materials and the effect of additives on the rheological properties of MRE. Subsequently, the field-dependent property variations, operating frequency and input displacement dependent variations are discussed. Effective parametric models based on conventional viscoelastic theory is explored next. Furthermore, the use of Magnetorheological Elastomer as an effective vibration attenuator is addressed. Finally, the use of MRE in semi-active control strategies is summarized.

2.2. Constituent Materials

The constituent members of a typical MRE consist of the matrix and filler particles, which form the bulk of the elastomer. To improve its rheological properties, a selection of additives is available, which increases various parameters such as the surface area of the iron particles, bonding between the iron particles and the matrix, to name a few. The present section explores the various constituent particles and additives used in the study of the Magnetorheological elastomers.

2.2.1. Filler particles

The rheological properties of the MRE are substantially affected by choice of the filler particles. The particles chosen for the MRE must be of higher magnetic permeability (above 6 $\mu H.m^{-1}$) with high magnetic saturation (1T) and low remanence (Lokander and Stenberg 2003a); due to which the Carbonyl iron particles (CIP) have attained much prominence rather than the various alloys of iron. Irregular and regular-shaped micron-sized iron particles have been extensively used to synthesize MRE (Gong et al. 2005)(Lokander and Stenberg 2003a). Due to its larger size (average diameter above 60 μm) in comparison with the regular-sized particles, irregularly shaped particles have a better field-induced dipole interaction under a similar level of reinforcement. However, irregularly shaped particles have a lower reinforcing effect, which leads to a reduction in the zero-field modulus. Contrarily, the regular-shaped particles which are lesser in diameter often lead to agglomeration. This, however, enhances the rheological properties of the MRE in the direction of the applied magnetic field. Of the various geometrical shapes available for the regular-sized particles, the spherical-shaped regular iron particles are preferred due to its ease in mixing and its pre-structure arrangement during the preparation of the MRE. Apart from the spherical shaped particles, other shapes such as rod-shaped (Kumar and Lee 2017) have also been used but to a lesser extent.

The variations in the size of the particles have an observable effect on the properties of the MRE. Generally, the regular-sized particles consist of Nanosized to micro-sized particles. The finer Nano-sized particles are more prone to agglomerations, resulting in reduced interactions between the free matrix and the individual fillers' surface area (Hegde et al. 2014). However, these agglomerations are beneficial in the

direction of the applied field, as it increases the total surface area of contact with the interlaying matrix. Various ferromagnetic particles ranging from 5 to 100 μm in diameter have been used as filler materials. Past literature attests that Carbonyl Iron Particles, with the average diameter in the range of 1 - 9 μm, forms the ideal filler material with an optimum particle volume concentration of 25-30% (Hegde et al. 2015) (Lokander and Stenberg 2003a). These particles provide a more effective area of interface adhesion between the matrix and the particle. Besides, Nanowire fillers have also been used (Padalka et al. 2010); however, it is reported that the most considerable amount of nanowires is less than 10% by volume, beyond which the addition of nanowires results in the reduction of the curing of the MRE (Bell et al. 2010).

Another aspect on which the rheological properties of MRE are largely dependent is the concentration of filler particles (Kallio 2005). Filler concentration is expressed either in terms of volume fraction or weight fraction of the MRE. The volume and weight fraction of the composite is inter-related by the density of the constituents. The addition of filler results in the reinforcing effect to the base matrix, thereby increasing the zero-field modulus of the MRE. Further incorporation of filler results in better field-induced variations in the storage modulus of MRE. For better field-induced variations on the MRE properties, an optimal percentage of the filler is required. Past research highlights the reduction in the variations of the field-induced properties at lower concentrations of the filler (less than 20% by volume). The reduction is attributed to the availability of lesser particles within the unit area of the MRE, resulting in reduced dipole interactions between the individual filler particles. An increase in the filler volume concentration increases the active dipoles providing a better force of attraction between the particles. However, these variations saturate beyond a certain volume fraction of the filler. Further increase in the filler (above 35% by volume) results in the reduction of availability of the matrix and renders the material brittle resulting in the reduction of the MR effect. Literature highlight an optimum level of 25% to 35% of the filler volume beyond which the properties of the MRE reduce. It is reported that for a 27% volume fraction of the filler, the field-dependent variations saturate beyond 0.4T under translatory shear loading (Poojary et al. 2016). Variations in the volume fraction also influence the energy dissipation capacity of the MRE(Chen

and Gong 2008). Though filler-filler interactions on the damping are less due to the reduced surface area of the fillers, the damping due to the filler-matrix interactions is predominant. The increase in the filler volume fraction increases the interfacial damping of the MRE.

2.2.2. Effect of type of matrix

For the various viscoelastic based polymers (silicone, natural rubber, polyurethane-based rubbers), the variations in the formation of the Long chains of cross-linked polymers determine the type of the elastomer. Based on the density of the cross-links, the elastomers are classified as "Hard" and "Soft" (Chertovich et al. 2010) (Hoang et al. 2011). Hard matrices (Young's modulus > 10kPa) are composed of a higher density of cross-linked polymers, which results in larger shore hardness. They offer higher zero-field stiffness, but the damping capability reduces. Soft matrix (Young's modulus < 4kPa), on the other hand, is more flexible owing to the reduced cross-linked chains. The filler particles have a relatively larger movement under the effect of the magnetic field, resulting in a higher field-induced stiffness. However, in the process, the load-bearing capacity and fatigue life of the MRE is compromised (Zhu et al. 2012) (Li et al. 2012a). Additionally, the hard and the soft matrix influences the transition of the MRE from linear to nonlinear state. Harder matrices have reduced field-dependent variations and thus, the nonlinearity in the dynamic response occurs at a relatively lower displacement. For softer matrices, however, the influence of fillers is detected at a relatively higher displacement, before which the nonlinear behavior is observed.

Elastomers are also classified based on the type of vulcanization process as High-Temperature Vulcanized (HTV) rubber, also known as Unsaturated Elastomers and Room Temperature Vulcanized (RTV) rubber alternately known as Saturated Elastomers. Preparation of the HTV elastomers involves the mastication of rubber, and the curing process is carried out at high temperatures (as high as 180°C), thus making it a temperature-sensitive elastomer (Li and Gong 2008a)(Liao et al. 2013)(Liao et al. 2012). on the contrary, RTV elastomer does not require higher temperatures and the curing occurs at room temperatures with the addition of curing agents (Poojary et al. 2017)(Johnson et al. 2018). Since the elastomer-based matrix is present in its viscous state, the entrapped particles suspend and distribute easily in the matrix. The mixing of

the constituent particles often results in entrapped air bubbles that need to be removed by degasification (Palacios-Pineda et al. 2017). Due to the ease of manufacturing, the RTV-based MRE has gained much prominence over the past years (Ubaidillah et al. 2015).

The damping characteristics of the matrix are often termed intrinsic damping due to the inherent behavior of the crosslinked polymer chains(Yang et al. 2012). In the absence of any filler particles, the polymeric chains are susceptible to the applied input displacement and frequency, resulting in the energy dissipation by the viscoelastic member. In the presence of filler particles, the intrinsic damping of the elastomer reduces due to the dominance of the filler-particle interfacial damping.

Apart from the above, the viscoelastic properties of the MRE depend significantly on the temperature (Wen et al. 2020), wherein, increase in temperature leads to a reduction in the modulus.

2.2.3. Additives

The inclusion of additives usually enhances the performance of the Silicone-based MR elastomers by promoting the compatibility of the constituent particles of the MRE. Additives either improve the interfacial bonding between the filler and the matrix, or they enhance the properties of the viscoelastic matrix. Generally, the type of additives used for the preparation of the MRE is in liquid form (plasticizers, coupling agents) or powder form (carbon black, graphite, carbon nanotubes).

Plasticizers are used during the curing of the MRE, which alters the rheological properties of the elastomer (Ahmad Khairi et al. 2017). Moreover, they help in increasing the affinity of filler particles to the matrix by modifying the surface of the filler particles (Chen et al. 2007). In the absence of plasticizers, short linkages of the elastomer constraints the movement of the interlaying filler particles. The reduced filler movements decrease the field-induced stiffness of the MRE. With the addition of plasticizers (at 10% weight), the elasticity of the MRE composite increases, facilitating the movement of the filler particles. These unique properties of the additives increase the field-induced rheological properties of the MRE. It further helps in uniform distribution of the filler particles.

The addition of coupling agents can enhance the compatibility between the constituent components of the MRE. Coupling agents get adsorbed within the interface, thereby increasing the chemical bonding between the elastomer and the filler. Most often, silane (Pickering et al. 2015) and titanate couplings (Li et al. 2012b) are commonly used. While silane, with a weight percentage of 6%, increases the loss factor by 20%, the titanate couplings enhances the MR effect by as much as 180% for isotropic MRE. They further increase the strength of the MRE with improved dispersion of the filler particles. However, the couplings decrease the actual particle content within the given area of the MRE, thereby increasing the particle-particle distance, which subsequently reduces the field-induced interactions. This reduces the MR effect. Along with the liquid-based couplings, powder-based couplings are also used. Nano-sized powder couplings adhere to the surface of the filler particles, decreasing the space between the constituent particles, in turn, enhancing the filler-matrix interaction. This enhances the stiffness of the MRE. Besides, they also increase the magnetic properties of the composites. Under the influence of an external magnetic field, the coupling agents reduce the distance between the constituents, thereby increasing the dipole interactions. Increased dipole interactions increase the field-induced interactions compared to the base MRE. Commonly used coupling agents are Graphene, CNT and carbide-based agents(Bica et al. 2014)(Poojary et al. 2018)(Kumar and Lee 2019).

The performance of the powder-based additives depends on the size of the particles. Smaller sized additives of less than 0.6 μm form an aggregate with the surrounding filler particles resulting in a stronger particle cluster. Larger sized additives obstruct the movement of the interlaying polymer chains by locking them in place. Reduced motion decreases the rheological properties of the MRE under dynamic loading conditions. However, it is to be noted that the additives have optimal range, beyond which the rheological properties tend to reduce. With an increase in the content of additives, the amount of particle-particle bonding decreases, subsequently reducing the stress transfer between the polymer chains and the filler particles. The reduced stress transfer results in lower field-dependent variations even under higher magnetic fields. This calls for a need to optimize the use of additives based on the constituent filler-matrix fractions.

2.3. Working parameters

While the selection of the constituent materials plays an essential role in the rheological properties of the MRE, the dynamic properties are dependent on the working parameters, namely the magnetic field, operating frequency, and the input displacement. The present section discusses the effect of the aforementioned parameters on the properties of the MRE.

2.3.1. Field dependent characteristics

Field dependent variations in the properties of Magnetorheological materials were studied as early as 1948 (Rabinow 1948). Microscopic ferrous particles were added to certain carrier fluids and their properties changed under the influence of the magnetic field. However, it was not until the influential work carried out by (Rigbi and Jilkén 1983) that the idea of MRE was first conceived. In the absence of an external magnetic field, the MRE acts as a passive, filled viscoelastic member with no change in its rheological properties. However, under the influence of the magnetic field, the filler particles align in the direction of the applied field, which in turn changes the rheological properties. Termed as "MR Effect," the field-dependent variations in the properties of MRE was first studied extensively by (Jolly et al. 1996b) and (Carlson and Jolly 2000). The phenomenon was further illustrated by adopting the dipole model of the filler particles, which adequately explained the field stiffening property of the MRE.

The field-induced variations on the rheological properties of the MRE are assessed from the dynamic tests and the resulting force-displacement curves are studied. The response is expressed in terms of complex stiffness, which expresses the effectiveness of the viscous nature of the fluid component (in terms of energy lost) and the elastic nature of the solid elastomer (energy stored). Mathematically it is represented as (Poojary et al. 2016),

$$K^* = K' + i\,K''$$

Where, K^* represents the complex stiffness, K' represents the real part or the stiffness part of the elastomer and K'' represents the imaginary part of the energy dissipated part of the elastomer

Past literature reveals that the complex stiffness of the elastomer increases with an increase in the magnetic field. Characterization studies confirm an increase of the complex stiffness till 0.4 to 0.5 T, beyond which saturation is attained (Chen et al. 2016) (Poojary and Gangadharan 2016). However, it is also observed that the field-dependent saturation largely depends upon the type of matrix (Hard matrix show saturation at a lower field), the amount of filler particles (Higher fraction reduces saturation limit) and the presence of additives. Moreover, the MR effect is influenced by the size and shape of the iron particles (Hegde et al. 2014), the temperature of operation (Wan et al. 2019) and the introduction of magnetic field during the curing process (Vatandoost et al. 2020).

Application of the magnetic field to the MRE during its curing process often results in the enhancement of its rheological properties. Under normal curing processes, micron-sized iron particles are locked into the base matrix, increasing the complex modulus of the MRE. However, if sufficient magnetic field (as high as 0.8 T) is applied during the process, the particles get aligned in the direction of the applied field, resulting in the enhancement of the complex stiffness of MRE. This type of MRE is termed as Anisotropic (Li et al. 2010)(Agirre-Olabide et al. 2014a)(Nayak et al. 2015)(Bellelli and Spaggiari 2019), while the absence of magnetic field during the curing process results in Isotropic MRE (Gong et al. 2005)(Hegde et al. 2015)(Yarra et al. 2019)(Agirre-Olabide and Elejabarrieta 2018). Though the Anisotropic MRE offers advantages such as path specific enhancement in dynamic properties of complex stiffness and loss factor, the requirement of a constant magnetic field during the curing process restricts its applications(Lu et al. 2012). Besides, the fabrication of a thick anisotropic MRE is impractical since the amount of magnetic field required to uniformly distribute the iron particles would be huge. Moreover, recently, researchers have developed anisotropic MRE using the additive manufacturing process without the need for applying an external magnetic field (Bastola et al. 2020).

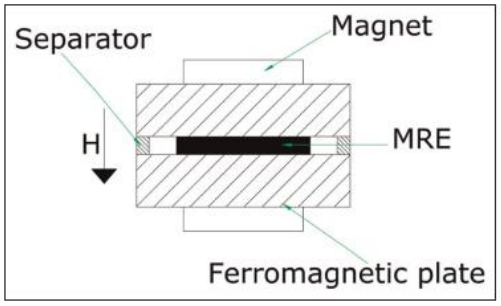

Figure 2-1 Anisotropic MRE (Agirre-Olabide et al. 2014b)

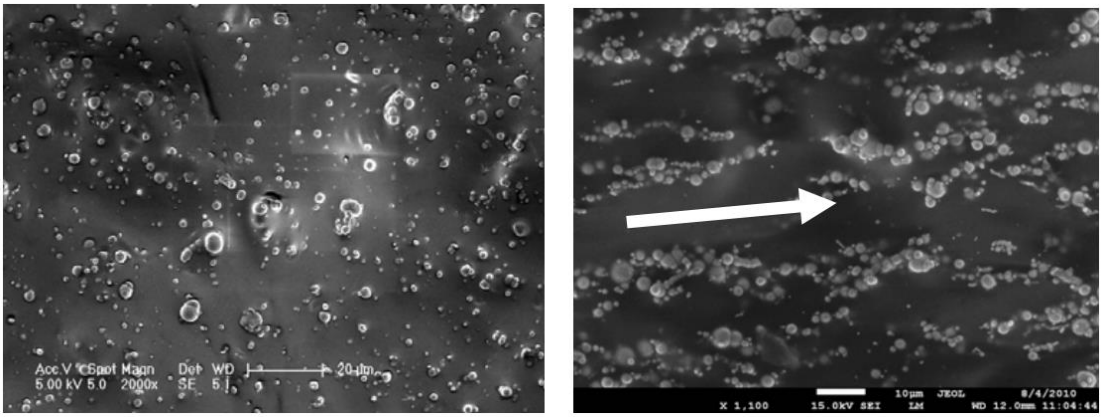

Figure 2-2: Isotropic and Anisotropic MRE (Li et al. 2012a)

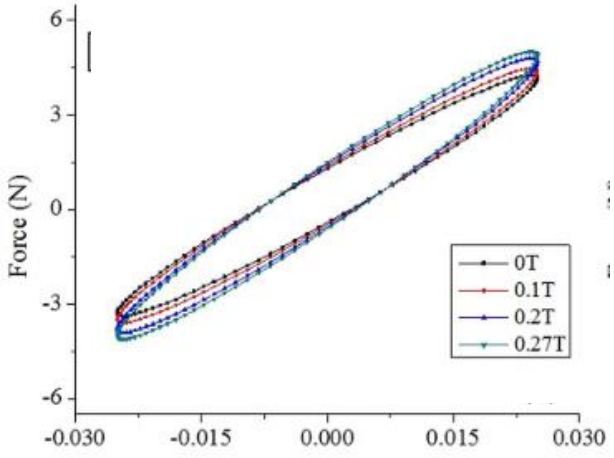

Figure 2-3: Effect of field on the rheological properties (Poojary et al. 2018)

Similar to the field-dependent stiffness variations, the damping characteristics of the MRE is also dependent on the applied magnetic field. However, past researches reveal an inconsistent trend for the field-dependent energy dissipation variations. Some

studies conclude that the damping follows a similar trend as that of the variations observed in the stiffness, i.e., it increases with an increase in the applied field (Song et al. 2009)(Fu et al. 2016)(Poojary and Gangadharan 2017). However, other researches reveal the trend to be negligible as the variations are inconsistent(Dong et al. 2009) (Ge et al. 2013) (Yang et al. 2014). Alternately, some results reveal a reduction in the damping after an initial increase (Li and Gong 2008b). The field-induced damping is less significant compared to interfacial damping, which exists between the matrix and the filler interface. However, the magnetic field's influence on the interfacial damping is pronounced (Ju et al. 2012a).

2.3.2. Frequency and Displacement dependent studies

The frequency dependence of the MRE is derived from the viscoelastic nature of the base matrix(Johnson et al. 2018). Based on its applications, MRE has been developed as an effective vibration attenuator for frequencies ranging from as low as 0.5 Hz to as high as 100 Hz. The frequency-dependent behavior of the MRE is associated with the slower response of the polymer chains under the external cyclic loads. The slower response results in a lag between the input displacement and the output force response. As a result of the slower response, the complex stiffness of the MRE is reduced at lower frequencies of excitation. With increasing frequencies, however, the response is quicker, resulting in the complex stiffness of the system to increase.

For filled elastomers like the MRE, the effect of operating frequency on the complex stiffness is not as predominant as that of an unfilled elastomer. Furthermore, research reveals a prominent influence on the complex stiffness at lower frequencies compared to that at higher frequencies where saturation is observed. Additionally, variations in the operating frequency result in the enhancement of the damping of MRE. It is observed that less energy is dissipated at lower operating frequencies compared to the higher operating frequencies. The reduced dissipation is attributed to the dominance of the filler-matrix based interfacial damping with an increase in the frequency.

Due to the characteristic of a filled elastomer, the input displacement (strain) has a significant impact on the properties of MRE. Various theories have been proposed to explain the dependency, of which the Payne effect (Borin and Stepanov 2015) (Agirre-Olabide and Elejabarrieta 2017) and the Bound rubber theory (Zhang et al.

2007)(Poojary et al. 2017) (Agirre-Olabide and Elejabarrieta 2018) have been prominent. While the Payne effect explains the variations in stiffness due to the agglomeration of the filler particles, the bound rubber theory focuses on the matrix layers' formation and flexibility around the filler particles. Past literature also studies the magnetic field's influence on the cross-links at varying amplitudes of displacements (Poojary and Gangadharan 2017). Moreover, it is reported that delamination occurs under very high displacements (Xu et al. 2017). Type of the matrix plays an essential role in the MRE performance under large strain applications (Yarra et al. 2019). Input displacement affects the energy dissipation capacity of MRE. Increasing displacement results in an increase of the relative movement between the polymer chains and the filler particles. This increases the interfacial damping between the constituent particles. The introduction of the field does tend to decrease the displacement induced variations.

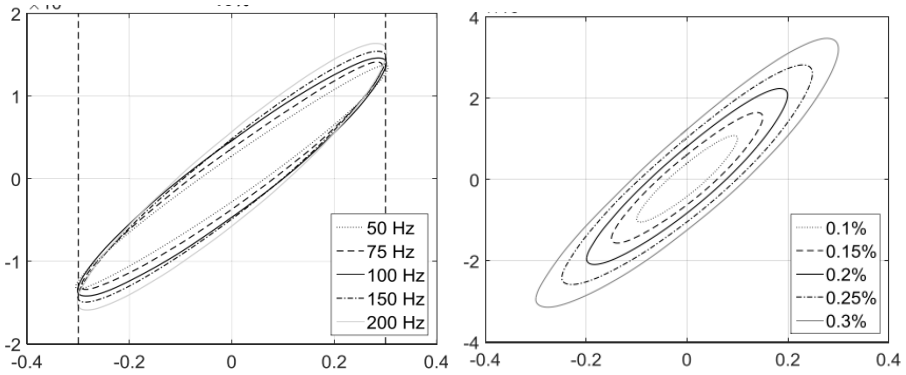

Figure 2-4 Effect of frequency and field on the stiffness of the MRE (Agirre-Olabide and Elejabarrieta 2018)

2.4. Dynamic characterization of MRE

Property characterization of the viscoelastic materials is carried out either by static tests or dynamic tests. Static tests represent the elastomers as "High Elastic" rather than highlighting the viscoelastic nature portrayed in dynamic tests (Brown 2006). The rheological properties under dynamic loading conditions are comprehended using the transient response method or the dynamic method (Sternstein 1983). The transient method involves obtaining the decaying output response of the elastomer for a given instantaneous input. On the other hand, the dynamic method measures the periodic response for a given harmonic input. Depending upon its region of operation, the dynamic method technique is further categorized as resonant method and non-resonant

method (Lakes 2009). Rheological property characterization using a non-resonant method is carried out using Rheometer, Dynamic Mechanical Analyser (DMA), or forced vibration tests. Rheometer (Li et al. 2010) (Borin et al. 2018) (Agirre-Olabide et al. 2018) and DMA (Chen et al. 2008a) (Nayak et al. 2015) are used widely in characterization using either controlled strain or controlled stress input. However, the above techniques are used to understand the material properties of the elastomer, devoid of the geometrical aspects of MRE.

In general, for the characterization of the MRE isolator, which involves the evaluation of the geometry-dependent complex properties, the specimen is subjected to the forced vibration tests based on ISO 10846-1 (Iso 2009). ISO 10486-1 defines the testing procedures for vibroacoustic properties of resilient materials. ISO 10846 (International Organization for Standardization 2002) is subdivided into the direct stiffness method (ISO-10846-2) and indirect stiffness method (ISO 10846-3). The direct stiffness method has the input as either displacement, velocity or acceleration with the response force. In contrast, the indirect stiffness method measures the transmissibility response of the resilient material. The direct method is categorized into the drive point method and blocked transfer method (Nadeau and Champoux 2000). The drive point method measures the force on the input side due to which the influence of the inertial component at higher frequencies is observed. Though the effect can be overcome with a reduced payload, the results are significantly affected by frequencies as low as 30Hz (Ooi and Ripin 2011). Blocked transfer method overcomes the issue by measuring the force at the blocked end, which is devoid of the effect of the inertial component. Further, the property estimation from the blocked transfer method is carried out either by the receptance method (Lin et al. 2005), transmissibility plot (Ramorino et al. 2003) or the Lissajous plots (Brown 2006). The Lissajous plots, otherwise known as Hysteresis curves, offer the real-time indication of the viscoelastic response and a simple technique to obtain the dynamic stiffness and loss factor.

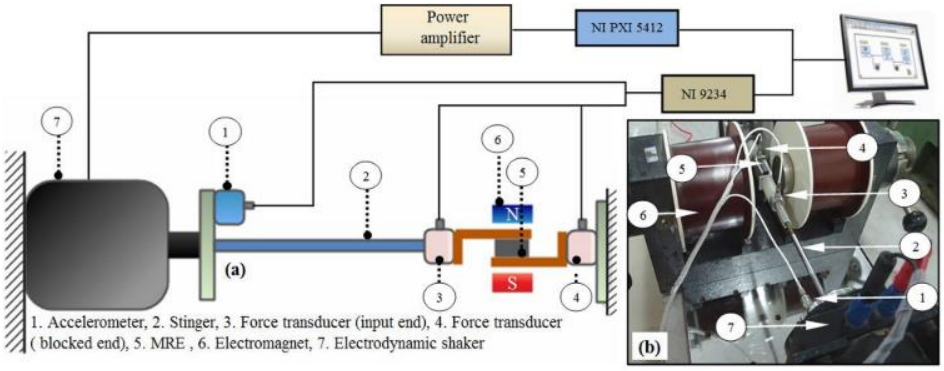

Figure 2-5: Characterization of MRE for translatory load

2.5. Modeling

The modeling of complex behavior of Magnetorheological elastomers forms a quintessential step in implementing the MRE for engineering applications. It plays a vital role in the ability of the MRE isolator or absorber to modify its properties in response to an external control signal. Since the MRE is a viscoelastic material, the modeling technique differs from that of a pure solid or a pure liquid. The factors affecting the rheological properties of the MRE are the applied magnetic field, frequency and input angular displacement. To assess the property variations, the modeling approach for the MRE is divided into two parts: the parametric method and the non-parametric method. The non-parametric modeling technique involves using mathematical functions of polynomial equations that do not encompass the actual behavior of the MRE. Parametric modeling, on the other hand, focusses on the use of actual parameters such as springs and dampers, which represent the actual energy storing and dissipating capacities of the MRE.

The simplest form of the parametric modeling technique is the Kelvin-Voight model, which has the parallel combinations of an energy-storing spring element and an energy-dissipating dashpot element. Similarly, the Maxwell model includes the parameters in series combinations. Building on the Kelvin-Voight model, an extra spring element is added in parallel, taking care of sudden loading on the element. Further, researchers developed these models by adding extra spring and dashpot elements, which increased the model's usefulness for different strain rates, frequencies, and fields (Li et al. 2010). Likewise, in order to describe the creep and stress relaxation of the viscoelastic materials, parametric models such as the Zener model and the

Poynting model have also been developed (Gamota and Filisko 1991). These are also known as the "Standard Linear Solid" or SLS model. To incorporate the nonlinearity in the material during higher displacements, the Ramberg-Osgood model was added in parallel with the Maxwell model (Eem et al. 2012). The Ramberg-Osgood model adequately describes the non-linearity in the material, while the Maxwell model introduces the viscoelasticity of the MRE. Apart from the Ramberg-Osgood model, other models such as Bouc-Wen model (Behrooz et al. 2014a) and the Prager model (Kaleta et al. 2007) were introduced along with the classical viscoelastic models to describe the nonlinear Hysteresis behavior of the MRE.

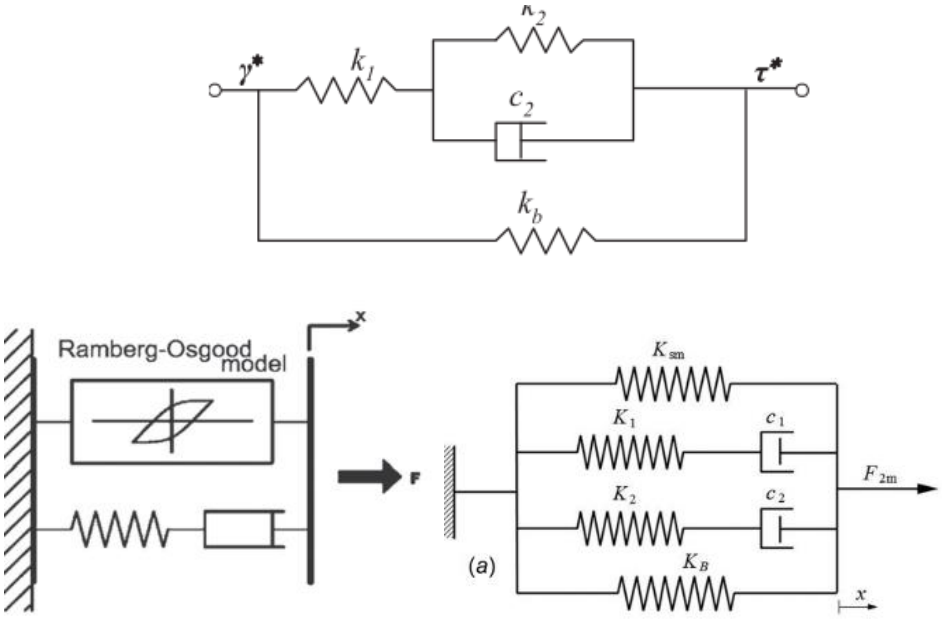

Figure 2-6: Existing Modeling Techniques

Though the models' effectiveness could be improved with more springs and dashpots, the increase in the number of parameters results in the increased parameter identification process. This can be effectively addressed by introducing the fractional-order element. A fractional derivative element (Poojary and Gangadharan 2018) (Agirre-Olabide et al. 2018), also known as spring-pot, envisages the properties of the viscoelastic member by taking into consideration the properties of both; the elastic characteristic of the spring and the viscous characteristic of the damper. The regular phenomenological models could be easily incorporated with the fractional element, reducing the number of parameters. These models easily consider the dependency of viscoelasticity of the MRE on the operating parameters, mainly the frequency.

2.6. Vibration Attenuators and control strategies

MRF based dampers have been used widely for various applications. Notably, they have been used in off terrain vehicles for their variable damping properties. Though various semi-active based control strategies have been developed to reduce the amplitudes of vibrations effectively, MRF cannot be used to achieve the required isolation under variable stiffness regimes prominently seen under multi-frequency applications(Li et al. 2014)(Guo et al. 2012)(Opie and Yim 2011). In the stiffness-controlled or the mass-controlled regions, variable damping has little to no effect on the transmissibility of the vibrations. In fact, improper tuning of the MRF in the mass-controlled region results in an increase in amplitudes rather than the expected reductions.

Due to its advantages over the MRF, MRE-based attenuators have attracted considerable attention in the field of seismic vibrations, structural vibrations, seat structures and powertrain systems(Ni et al. 2010)(Lerner and Cunefare 2008). As seen before, MRE works in the pre-yield state and is controlled by the complex stiffness under varying magnetic fields. These advantages result in the MRE as a potential candidate for the development of semi-active isolators and absorbers.

2.6.1. Vibration Absorber

Absorbers are auxiliary systems that are often placed on the vibrating structure. A typical dynamic vibration absorber (DVA) primarily consists of a moving mass (inertia), a restoring spring and an energy-dissipating, damper component. When the operating frequency matches the natural frequency of the absorber, the DVA absorbs the excess amplitudes from the primary system. However, a significant drawback of the DVA is its passive nature due to its fixed stiffness and damping. It often results in the inability of the DVA to work effectively under varying natural frequencies. The passiveness of the DVA is overcome with the use of active vibration absorbers. Though the technique effectively reduces the excessive amplitudes, it involves the application of enormous force and the energy required is substantially large as the natural frequencies increase. An alternative option is the use of semi-active absorbers where the dynamic properties such as stiffness and damping are tuned to varying natural frequencies of the primary system. MRE, due to its controllable rheological properties,

offers an excellent candidate for the semi-active absorber system and has been effectively used in tuning the absorbers.

The adaptive tunable vibration absorber was developed by (Ginder 2001). MRE-based vibration absorbers typically work in various modes of operation based on the loading conditions (Lerner and Cunefare 2008). If the applied load shears the MRE along its thickness, the MRE absorber is said to be in shear mode. Conversely, if the applied load is perpendicular to the MRE's thickness, the resulting absorber is said to be compressive mode. Another mode is the squeeze mode, where the load is perpendicular as in compressive but tends to squeeze the MRE. Implementation of all the modes has been carried out in past researches. It is seen that for a given dimension, the squeeze mode performs better than the shear mode under similar working conditions (frequency shift for squeeze mode is 65Hz in comparison with 30 Hz shift for shear-based absorbers) (Sun et al. 2015a). However, a reverse trend is also reported, where the percentage shift in the MR effect is reduced for squeeze mode compared to the shear mode (Popp et al. 2010).

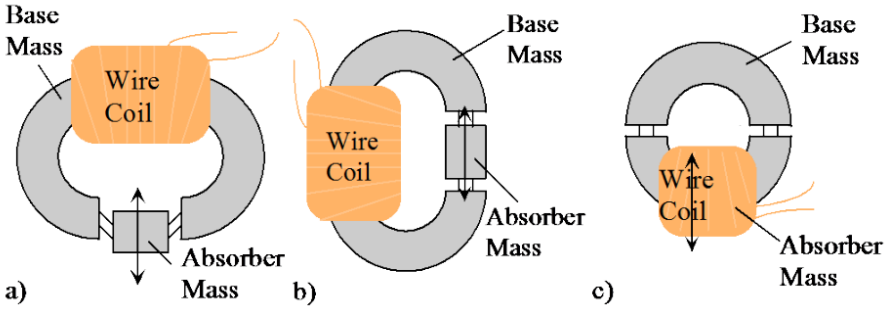

Figure 2-7: Shear and Compressive modes for MR Elastomer based absorber

Though the squeeze mode outperforms, it is it be noted that the success of the squeeze mode depends mostly on the geometrical constraints of the absorber design. Since the squeeze mode invokes a static displacement upon the inertia mass, the absorber needs to have a flexible design constraint (Sun et al. 2015a, Ni et al. 2009) proposed a squeeze- strain– enhanced MRE based MRE absorber. Apart from the design constraints, the application of magnetic field inhibits the performance of the compressive and squeeze mode of MRE (Ginder et al. 2002). Due to the requirement of the field to be applied in the same direction as that of the load, the arrangement of

magnets or the development of electromagnet offers a considerable challenge (Hoang et al. 2011).

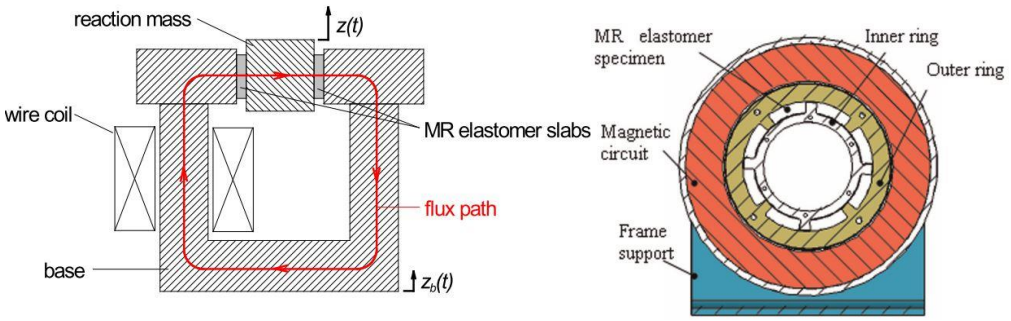

Apart from the arrangement of magnets, the performance of an MRE based absorber depends on the number of individual layers of MRE used in the system. Conventional single-layered MRE has been used effectively in vibration absorbers for varying frequency ranges. However, among the various issues associated, its inability to support the inertial mass in the vertical direction requires for the development of a multi-layered MRE structure (Sun et al. 2015b). These offer added rigidity to the existing compositions of the MRE enhancing the load bearing capacity of the absorber system. Additionally, multi-layered MRE offers a larger displacement of the system, (from 0.24 mm to 13.6 mm) resulting in the absorber working at higher amplitudes of vibrations. Moreover, it is observed that the multi-layered MRE, due to the increased thickness (16mm), has a lower zero-field stiffness value. This effectively works at the lower frequency (3.2 Hz) signals compared to the single-layered MRE (Sun et al. 2015b).

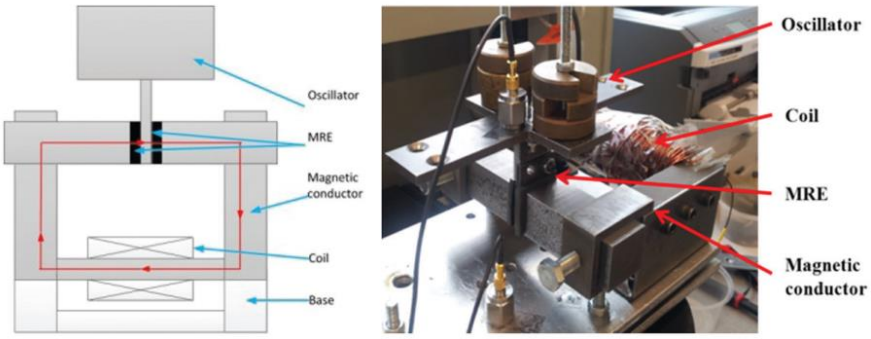

Apart from the vibrations in lateral mode, the attenuation of torsional vibrations is of importance, especially in powertrain systems. Specifically, for an automobile, the dynamic properties of the crankshaft vary depending on the gear sets. At various speed

ratios, the stiffness of the crankshaft changes, resulting in variable natural frequencies. The variable frequencies require the absorber to change its properties. Several methodologies have been applied to reduce the torsional vibration, such as the inclusion of Flywheels (Zu et al. 2015), centrifugal pendulum absorbers (Haddow and Shaw 2003) or the tuned vibration dampers (Deng et al. 2018). Flywheels are highly effective in reducing the torsional amplitudes of the driveline shafts; however, they add up to the inertia of the system. Vibration dampers and the centrifugal absorbers suffer from the problem of operating at a tuned frequency. Convectional dual-mass flywheels have been coupled with the centrifugal pendulum absorbers, which reduce the amplitudes to a large extent. However, though they do not work effectively at lower speeds especially below 1000 rpm due to the higher stiffness of the springs. Furthermore, they are highly inefficient to accommodate the variations in the stiffness of the shafts at different gear ratios. Also, with the addition of the flywheel, the inertia of the crankshaft increases significantly. With regard to the absorber, an MRE based ATVA has been developed for vibration attenuation of torsional vibrations in powertrains (Hoang et al. 2013). An MRE absorber working in the compressive model was developed and its dynamic properties were assessed. Based on the data, the torsional absorber is found to be effective in shifting the frequency for the working frequency of 10.75 Hz to 16.5 Hz. Moreover, to understand the effectiveness of the developed absorber in the powertrains system, simulations were carried. The results highlight the reduction of the torsional vibration amplitudes due to the shift in the primary frequencies.

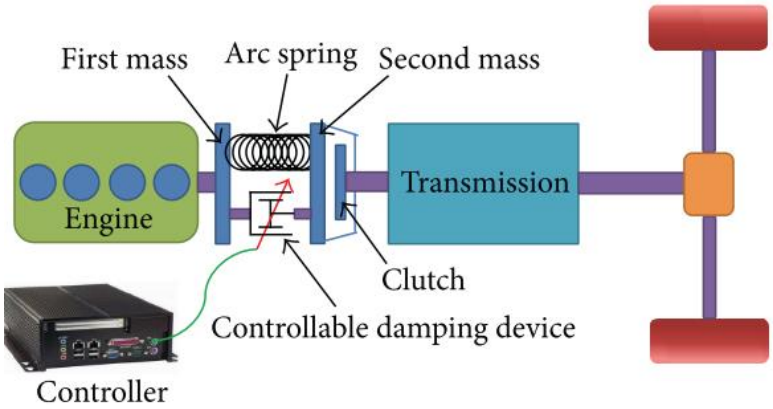

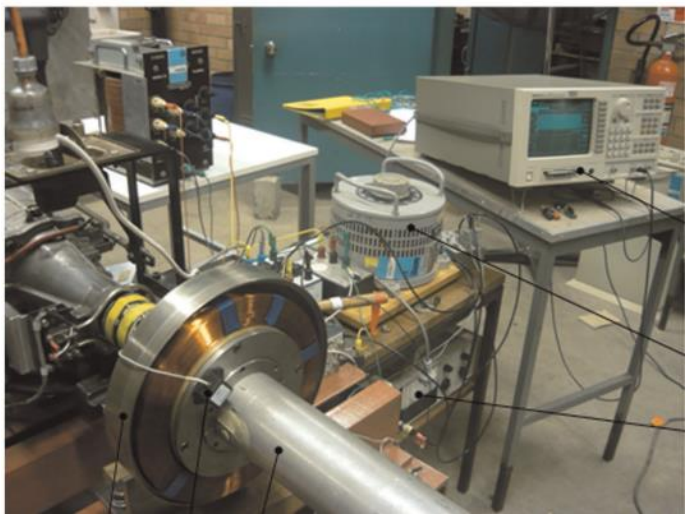

Figure 2-8: MR Elastomer based torsional Vibrations absorber

2.6.2. Vibrations Isolators

As mentioned earlier, the difference between absorbers and the isolators is the positioning of the auxiliary system. While the absorber has the auxiliary system placed on the vibrating system, the isolator is placed in between the vibrating base and the primary system. However, both the techniques focus on the controllability of the rheological properties of the MRE. Vibration isolation is carried in terms of displacement isolation or force isolation based on which the system performance is evaluated in terms of the displacement transmissibility and force transmissibility, respectively. Examples of the MRE based isolators include bushings in automobiles, vibration isolators in seats and seismic isolators and bridge isolation to name a few (Li et al. 2012d)(Yarra et al. 2018)(Jung et al. 2011).

The working frequency for the MRE based vibration isolation depends on the type of application. (Ginder et al. 2000) developed a proof-of-concept potential MRE isolator to reduce the translatory motion of the vehicular suspensions. With an operating frequency of 2Hz, the field-induced variations in stiffness and damping were analyzed. A 25% increase in the stiffness and damping was observed. (Bastola and Li 2018) studied the effect of simultaneous application of field and preloading on the isolator system. The frequency range of the study was 200 Hz – 1000 Hz. Under the influence of the field, an effective increase of approx. 2.65 times (280 Hz to 760 Hz) was observed in the natural frequency. However, the variations in damping were inconsistent with the increase in the field, though the zero-field amplitude reduced by 77%. apart from the

pure shear or compression modes of motion, research has been carried with a mixed mode of the MRE oscillations (Vatandoost et al. 2019). (Yang et al. 2015) developed a mixed-mode MRE isolator based on shear and compression mode. Under the influence of magnetic field, the natural frequency of the system increased from 48 Hz to 95 Hz with an increment of 103%. Further, the results indicate the increase in the damping offered by the MRE under the mixed-mode suggesting an improvement over the conventional mode.

Similar to the vibration absorbers, the concept of multi-layered MRE has been adapted for vibration isolators. The number of layers of MRE varies from 25 to 47(Li et al. 2013), with the thickness of individual MRE varying between 1mm to 2mm. (Behrooz et al. 2014a) developed a composite base isolator made up of conventional passive elastomer (rubber) and the semi-active MR elastomer. With a double shear mode, the transmissibility plots revealed a linear shift in the natural frequency of the system with the applied field with a frequency shift of approx. 1.2 Hz under the applied magnetic field.

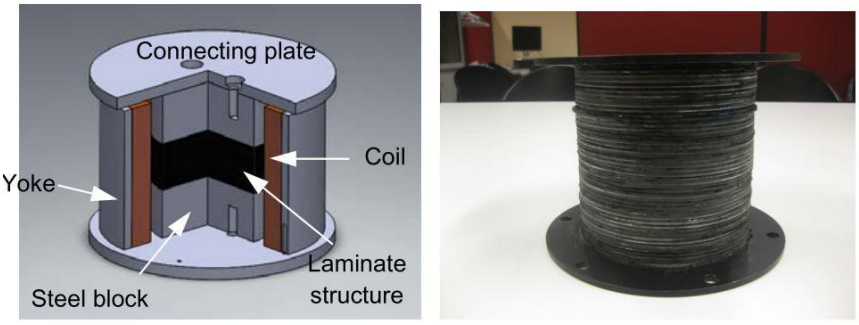

Figure 2-9: Multilayered MRE isolator

Various control strategies have been incorporated in the MRE-based vibration isolators. (Liao et al. 2012) developed an MRE vibration isolator with tunable damping and stiffness. MRE was used to provide the required variability in the dynamic stiffness while a voice coil motor provided the required damping capability to the vibrating system. Using the proposed ON-OFF control strategies, an effective reduction of 61.5% was observed in the transmissibility near the natural frequency of the system. (Opie and Yim 2011) developed an MRE based semi-active isolator using PID control. A hybrid magnetic circuit consisting of a permanent magnet and an electromagnet has been developed. The field intensity of the electromagnet was regulated using the developed

control. Sine sweep between 1 Hz to 25 Hz was given by an electrodynamic shaker and the corresponding acceleration transmissibility plots were obtained. Results show a reduction of 16-30% in the resonance amplitudes and velocities.

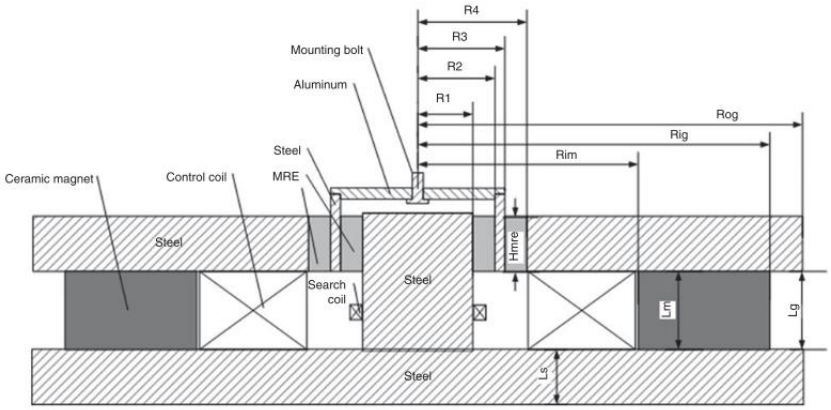

Figure 2-10: Hybrid magnet

(Xu et al. 2018) developed a stiffness controlled MRE based isolator with mixed-mode oscillations of the MRE. The developed MRE isolator worked in shear and squeeze mode and showed a stiffness increase of the order of three under the influence of the field. The results of the developed MRE were scaled up and implemented in a mathematical model of the seat suspension subjected to a vibrating base. Results indicate a reduction in the amplitude of the vibrating system. For a white noise excitation, a reduction of 12.5% was observed in the amplitudes, while a reduction of 22% was observed for a bump excitation input. (Gu et al. 2015) developed a real time back forward control strategy to the MRE isolator for a multistoried benchmark model. The simulation results showed that floors with the controlled MRE isolator was able to quickly and considerably reduce the amplitudes compared to the bare building without the MRE isolator and the building with passive isolator. (Hashi et al. 2016) developed an MRE based torsional isolation system for an operating frequency of 13.5 Hz. Under the influence of the magnetic field, the MRE isolator registered a approx. frequency shift of 4 Hz. However, the variations in the damping are inconsistent.

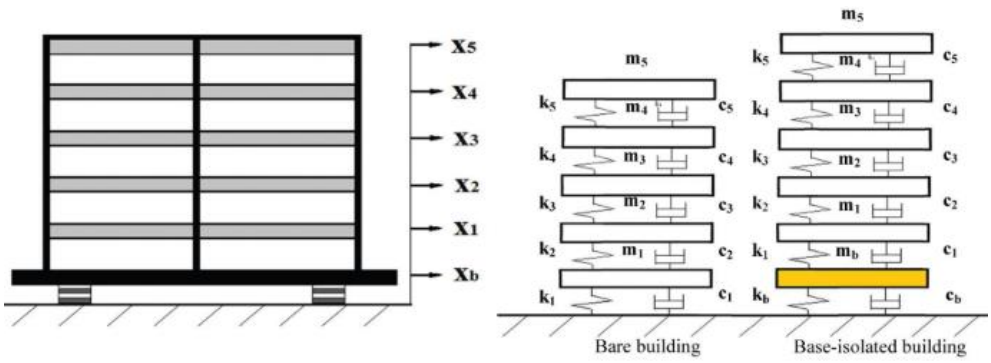

Figure 2-11: Seismic Vibrations isolation using MR Elastomer

2.7. Summary of the Literature reviewed

The constituent materials of the MRE comprise of the fillers, matrix and additives. Though the irregular shaped fillers provide better dipole interactions, the regular, spherical shaped fillers provide a better reinforcing effect. Similarly, the optimal volume fraction of the fillers of the average diameter of 4-10 µm is found to be between 25% to 35%. The choice of the matrix depends on various factors; specifically, on the loading conditions during the actual application of the MRE. Hard matrices are preferred for heavier loading purposes, whereas the softer matrices provide a good relative shift in the properties. Similarly, RTV based matrices are preferred over the HTV due to its ease in preparation. Furthermore, the choice of additives plays an important role in improving the properties of the MRE.

The viscoelastic properties of the MRE are dependent upon various parameters such as applied magnetic field, operating frequency and displacement. Field dependent properties have been thoroughly studied for translatory loading conditions. Also, the application of the magnetic field improves the rheological properties of the MRE in the direction of the applied field. However, the requirement of high fields (greater than 0.6T) limits its use. The rheological properties of the MRE are dependent upon the operating frequency due to its filled elastomeric characteristics. An increase in the frequency results in the faster movement of polymeric chains, which influences the rheological properties. Similarly, the properties of MRE are dependent upon the input displacement.

For the characterization of the elastomer, various approaches are available, of which the blocked transfer method as per the ISO 10846-2 forms the ideal method. This

method is devoid of inertial effect and provides the rheological properties of the MRE isolator considering its geometrical aspects. Various parametric based viscoelastic modeling techniques have been used to derive the constitutive relationship between the parameters. To suit the various properties of the MRE, various forms of the basic parametric models have been derived. Further, to reduce the number of individual springs and damping elements, fractional elements have also been used.

Concerning the applications, it is comprehended that the MRE has been used as excellent vibration attenuators. Literature highlights MRE based vibration absorbers and isolators in various modes of loading conditions. Multilayered MRE, as well as sandwich isolators, have been implemented across various vibrating members. Numerical simulations of the MRE based torsional vibration absorbers have shown that the transmissivity of the vibration could be effectively reduced for driveline shafts

2.8. Research opportunities

The implementation of conventional systems such as centrifugal pendulum absorbers with dual-mass flywheels has been successful in reducing torsional vibrations. However, due to their passive nature, the available attenuators are useful only for a specific frequency/speed range. Smart materials such as MRE based isolation system resolves this by adhering to variations in the resonant frequencies and facilitates the reduction in the amplitudes of vibrations.

Though the MRE has been thoroughly investigated and implemented in semi-active vibration control for translatory vibrating systems, the isolation capabilities of the MRE for attenuating torsional vibrations are very limited. Besides, the dynamic characterization of the MRE isolator for the torsional shear conditions is less reported and needs systematic understanding for various input parameters. Hence a comprehensive understanding of the behavior of Magnetorheological Elastomer under torsional loading conditions should be addressed with a thorough understanding of its characterization process.

2.9. Problem Statement

Torsional vibrations seen in all of the rotating shafts have a detrimental effect considering the constant twists leading to torsional stresses being developed on the shaft. Usually observed in the lower frequency ranges, it becomes necessary for the

removal of these vibrations. In the present study, a semi-active vibration isolation process using MRE is studied for a torsional system. The isotropic MRE is constituted of RTV rubber with CIP of average diameter of 5 μm. To comprehend its behavior, the dynamic characterization of the MRE under torsional loading is carried out for comprehending the variations dependent on operating frequency (10 – 30 Hz), applied field (0 – 0.3 T) and input angular displacement (0.002 – 0.016 rad) using a novel setup based on the ISO10846. Further, a phenomenological model is developed based on the modified Kelvin – Voight model to comprehend the constitutive relationship between the parameters. The constitutive model enhances the semi-active isolation capabilities of the isolator with the implementation of a model-based PID control. The isolation capabilities of the characterized MRE isolator are explored with a novel SDoF torsional vibrating system for different parameters. Hence the problem statement is defined as, "Experimental investigation and modeling of torsional vibration isolation using Magneto-Rheological Elastomer."

2.10. Research Objectives and Scope

Based on the literature reviewed and the research opportunities identified, the research objectives are listed as follows:

- To investigate the effect of magnetic field and frequency on the torsional stiffness of the MRE isolator
- To study the angular displacement dependent dynamic properties of the MRE under torsional loading conditions
- To develop a mathematical model and estimate the dependency of input parameters on the torsional properties of the MRE
- To evaluate the performance of MRE based Single Degree of Freedom (SDoF) torsional isolation system
- To develop a parametric based PID control strategy for the MRE isolator system

2.11. Summary

The current chapter presented the overview of the recent advancements in the field of characterization techniques, modeling and the vibration attenuation techniques of

Magnetorheological elastomers. The pertaining research gaps for the individual sections were identified and the motivation for the present research was presented. The succeeding chapter presents the methodology for the dynamic characterization of the MRE isolator under torsional loading conditions.

3. Methodology

3.1. Introduction

From the previous chapter, it was comprehended that of the various methods to carry out the dynamic characterization of the MRE, the Blocked transfer stiffness method offers results devoid of the inertial component of the system. Though the existing blocked transfer method is well suited in assessing the rheological properties of MRE isolator in lateral shear, it is not effective in portraying the properties under torsional shear. The present chapter focuses on developing a novel experimental approach to characterize the dynamic properties of an RTV based isotropic MRE under torsional shear. Initial discussions deal with the concept of the Blocked transfer method. The latter part of the chapter explains the development of the test setup based on the method.

3.2. Blocked transfer method

The schematic of the blocked transfer method used for the characterization of the viscoelastic elastomer for lateral loading is shown in Figure 3-1 (a). It has one end of the elastomer test specimen rigidly fixed while the other end is subjected to a known input. Hysteresis curves are obtained by plotting the input displacement and the output response force from which the variations in the dynamic properties are assessed. Similar to the lateral shear, the dynamic properties of the MRE under torsion is effectively assessed by adapting the blocked transfer method (Figure 3-1 b). The input angular displacement and the response blocked torque is plotted. Rheological properties such as complex stiffness and loss factor are obtained from the slope and the area under the hysteresis curve Figure 3-2

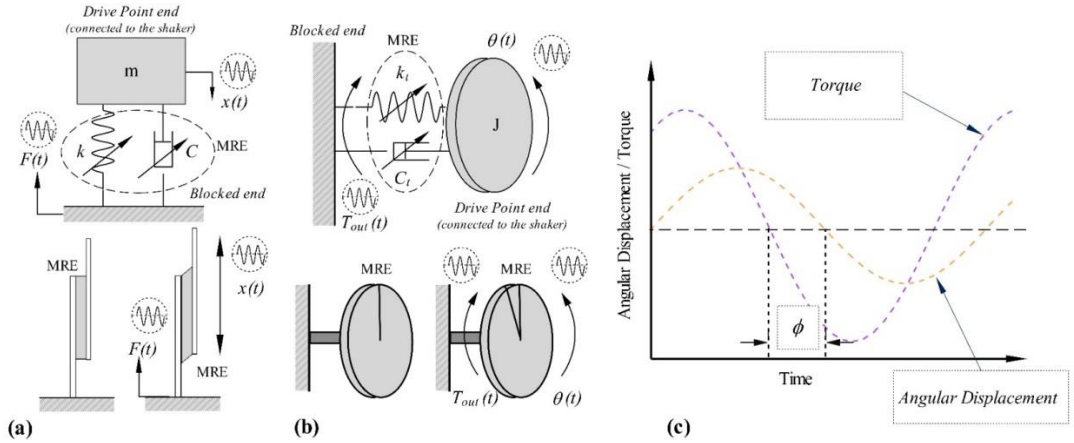

Figure 3-1: (a) blocked transfer method for lateral shear (b) Proposed blocked transfer method for torsional shear (c) Phase lag between the input angular displacement and output response torque

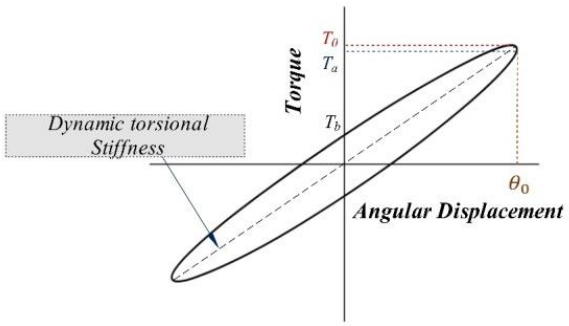

Figure 3-2: A typical hystesis plot of force-displacemet

3.2.1. Dynamic torsional stiffness and loss factor

From the hysteresis curves, the dynamic properties of the MRE are assessed in terms of dynamic torsional stiffness (complex stiffness) and the loss factor. The dynamic torsional stiffness is defined as the ratio of the output response torque (T_0) to the input angular displacement (θ_0)given as,

$$K_t^* = \frac{T_0}{\theta_0} \tag{3.1}$$

The output response torque and the input angular displacement for the measurement of the dynamic torsional stiffness are schematically shown in Figure 3-2 (b). A known input angular displacement, of amplitude θ_0 is given to the MRE sample. For a constant frequency ω, the harmonic equation is represented as

$$\theta(t) = \theta_0 \sin \omega t \tag{3.2}$$

The corresponding response torque generated at the output end is harmonic. For a perfectly elastic element, the response torque is in-phase with the input angular displacement. However, the viscoelastic nature of MRE results in a phase lag between the response torque and the input angular displacement by an angle φ (Figure 3-1 c) and is given by

$$T_{out}(t) = T_0 \sin(\omega t + \varphi) \tag{3.3}$$

The input angular displacement and the obtained output response torque are substituted in equation (1) to obtain the dynamic torsional stiffness of the MRE

Also, the energy dissipation capacity of the MRE is expressed in terms of the loss factor. The loss factor for a viscoelastic member is defined as the ratio of the imaginary part to the real part of the dynamic complex stiffness. It is the measure of energy lost to the energy stored by the material. For a viscoelastic material, the loss factor is given as,

$$\eta = \frac{K^{"}}{K'} \tag{3.4}$$

Also, the loss factor can be calculated from the Hysteresis plots as (Brown 2006),

$$\eta = \frac{T_b}{T_a} \tag{3.5}$$

Where

- T_a refers to the positive torque at the maximum positive angular displacement
- T_b refers to the torque at zero angular displacement

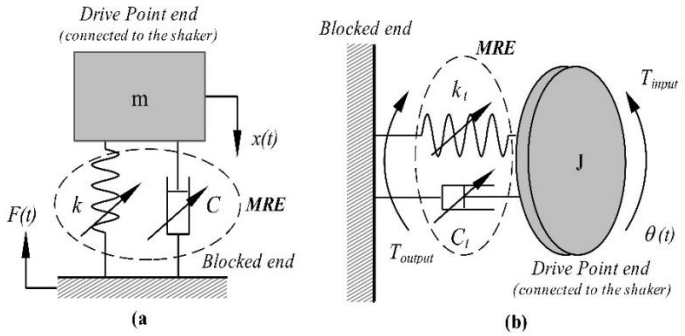

Figure 3-3: (a) Blocked transfer method for lateral shear (b) Blocked transfer method proposed for torsional shear

3.3. Experimental details

3.3.1. Preparation of isotropic MRE

A 2 part- Room Temperature Vulcanizing (RTV) based Silicone rubber (MoldSil 102LL (Part-A), with CAT 9 (Part-B), Performance polymers) and Carbonyl iron particles (BASF, type CN; average diameter 5 μm) form the essential components of the isotropic MRE. A volume fraction of 73:27 is maintained between the Silicone rubber and carbonyl iron particles(Poojary et al. 2018). All the constituent materials are converted into appropriate mass, considering the density of individual materials and the volume of the mould. Further, silicone oil (10% by volume of the silicone rubber) is added to the above mixture. To fabricate the MRE sample, the required mass of the carbonyl iron particles, silicone polymer (Part-A) and the silicone oil is blended and mixed thoroughly for 30 minutes to ensure proper distribution of the iron particles within the polymer matrix. Following this, the catalyzer (Part-B, 5% by volume of the silicone matrix) is added and the mixing is carried out thoroughly for 2 minutes(Bodelot et al. 2018). The mixture is then poured into a mould (50mm dia X 10mm thick), followed by degasification in a desiccator using a vacuum pump until the air bubbles are removed. This maintains the uniform magnetic permeability of the CIP throughout the sample. Further, the mixture is allowed to cure under constant pressure and room temperature for 24 hours (Li et al. 2014). Figure 3-4 illustrates the process.

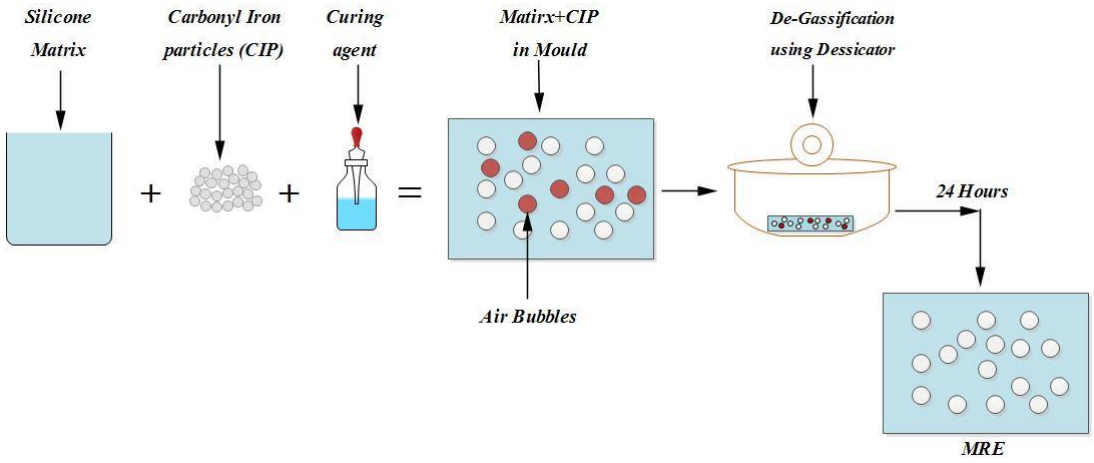

Figure 3-4: Preparation of isotropic MRE

3.3.2. Experimental Setup

Figure 3-5 (a) shows the schematic of the experimental setup developed to characterize the dynamic properties of the MRE as per ISO 10846-2 standard. Of the available ISO 10846 methods, as explained earlier, the direct method (ISO 10846-2) is used for the evaluation of the dynamic stiffness in the present study. It involves a controlled harmonic input angular displacement to one end of the MRE while the other end is rigidly fixed. The complex torsional stiffness is calculated by measuring the ratio between the amplitude of the torque transmitted to the rigid end through the MRE and the angular displacement imposed at the input end. Based on this, the MRE sample is sandwiched between two aluminum shafts of identical cross-sections (200mm Lemgth, 20mm diameter) (Figure 3-5 h). The input shaft is connected to the electrodynamic shaker (YMC MS-100) through a force transducer (KISTLER 9712) and a stinger (Figure 3-5d and g). The output shaft is rigidly blocked at the output end through another force transducer (KISTLER 9712, also known as Blocked force transducer) of identical specifications, as shown in Figure 3-5 b and g. The dimensions of the shafts ensure the negligible effect of its rotational inertia on the readings. Harmonic excitation is induced to the MRE sample via the shaker through an AGILENT 33220A function generator and a YMC LA-200 power amplifier (Figure 3-5 f). Input acceleration signals are observed using a YMC 121A single-axis accelerometer based on the IEPE type. Data acquisition techniques are used to convert the input acceleration signals to corresponding displacement (Behrooz et al. 2014b), which are further converted to angular displacements. The response torque ($T(t)$) is calculated as the product of force

measured by the force transducer (F (t)) and its distance from the axis of the shaft (r), as shown in Figure 3-5 c. The geometrical similarity is maintained by keeping the input and the output force transducers equidistant from the axis of the shafts. MRE sample is subjected to pure torsion by using bearings at appropriate locations to support the shafts, which keep the shafts in-line with the MRE sample. The input angular displacement and the output torque signals (Figure 3-5 e) are acquired and sent through a NI 9234 data acquisition system at a sampling rate of 25.6 kS/s, which is processed using LabVIEW 2014.

A custom in-house made electromagnet is developed to study the rheological properties of the MRE under different magnetic fields. To predict the magnetic field generated across the sample, Finite Element Method Magnetics (FEMM) software is used (Figure 3-6a). An external ferromagnetic strip on the electromagnet core enhances the intensity of the magnetic field on the MRE sample. The 2D, FEMM contour plot suggests the homogeneity in the generated magnetic field across the MRE sample. Figure 3-6b shows the magnetic field generated across the electromagnet measured using a Lakeshore Gaussmeter (410). A Sorenson programmable DC power supply (XG 150) provides the required voltage to the developed electromagnet. From the figure, it is observed that a maximum of 0.3T is achieved for input current of 5.5A.

The MRE is excited within the linear region and the dynamic characteristics of the specimen are studied by varying the input angular displacement at 0.002, 0.004, 0.008, 0.012 and 0.016 rad. The frequency-dependent studies are carried out in the range of 10 Hz to 30 Hz (Hoang et al. 2013). The input magnetic field is varied from 0T to 0.28T. Consistency in the readings is ensured by recording the data for a 10 sec time interval and the steady-state response of the results is observed by taking readings of 10 harmonic cycles. Due to its viscoelastic nature, the properties of the MRE sample are susceptible to its deformation history. Hence a recovery period between each test is maintained. The effect of the temperature variations is excluded by conducting tests at room temperature.

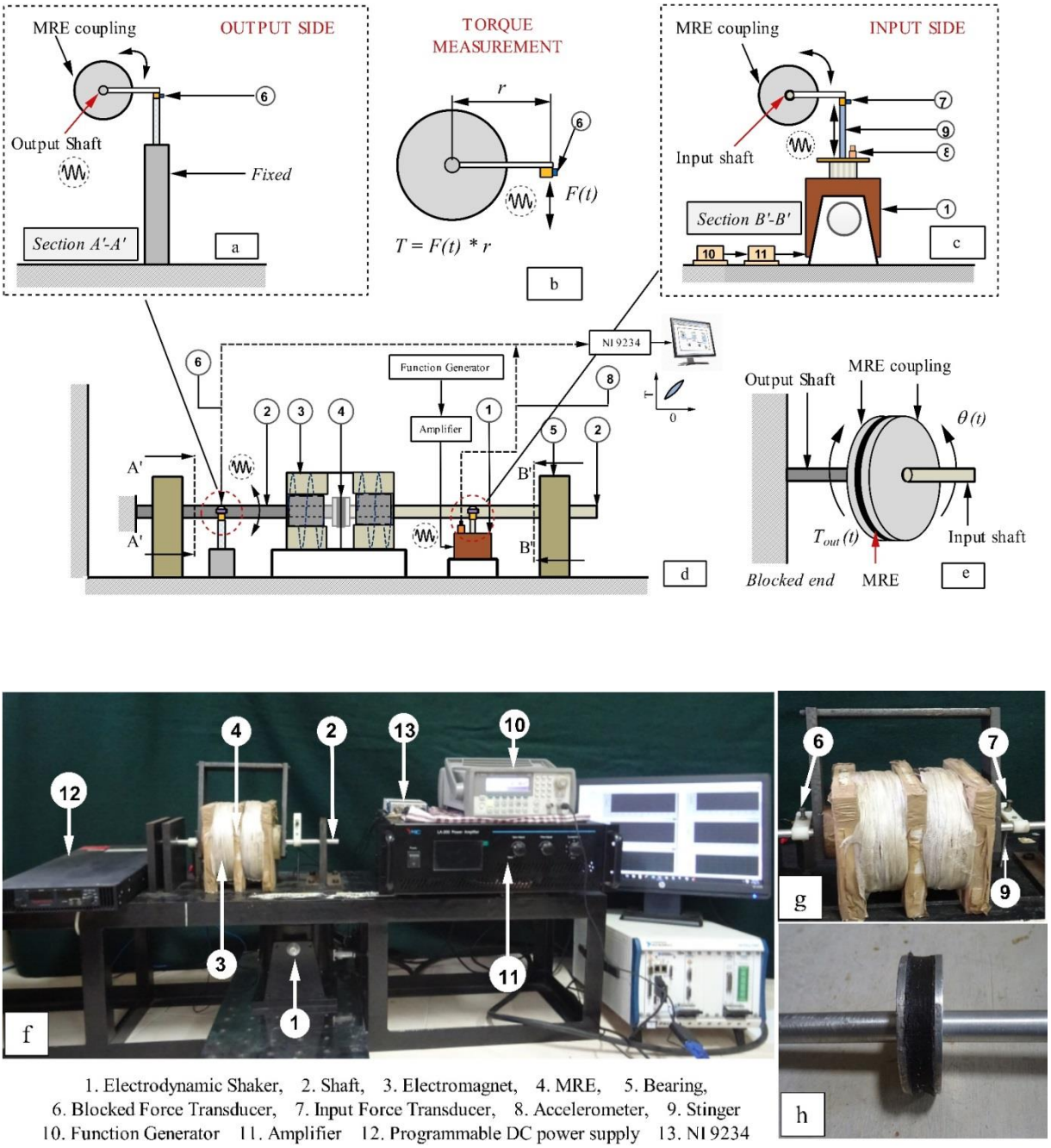

Figure 3-5: (a) Schematic representation of the experimental setup (b) Output Shaft (c) Measurement of torque from force (d) Input Shaft (e) Input and response on the MRE specimen (f) Photograph of the experimental setup (g) Inset showing the positioning of the transducers (h) MRE sandwiched between the shafts

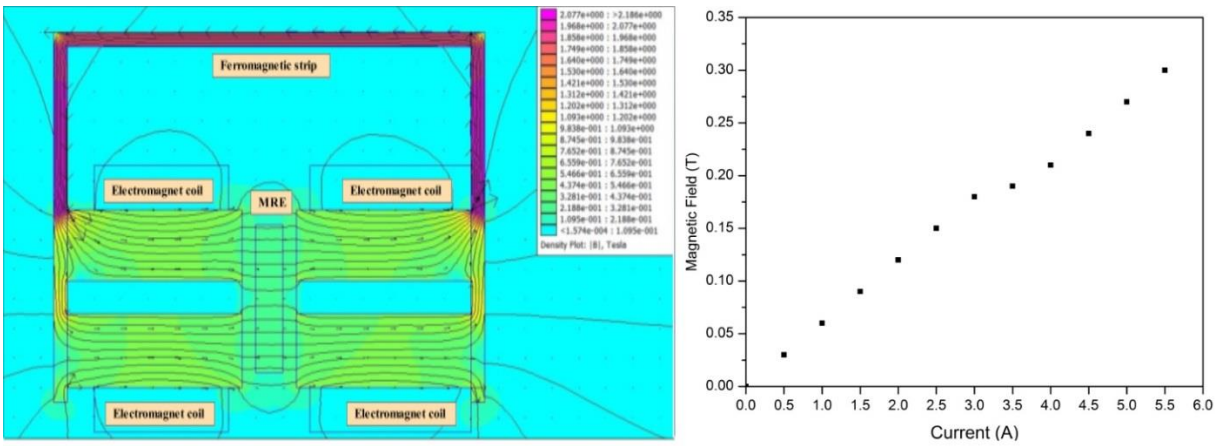

(a) **(b)**

Figure 3-6: (a) Predicted magnetic field variations across electromagnet using FEMM (b) Generated magnetic field in the electromagnet measured using Gaussmeter

3.4. Summary

The present chapter described the necessary methodology to carry out the dynamic characterization of the MRE isolator under torsional loading conditions. Initial discussions dealt with the preparation of the isotropic MRE. Following this, an experimental setup based on the ISO 10846-2 standard was developed. Succeeding discussions focused on the development of a custom-made, in-house built electromagnet to provide the in-line magnetic fields perpendicular to the torsional shear of the MRE.

With the experimental setup developed, the following chapter discusses the effect of the magnetic field, and the operating frequency on the torsional properties of MRE.

4. Effect of magnetic field and frequency on the torsional characteristics of MRE isolator

4.1. Introduction

The isolation capabilities of MRE for torsional vibrations are sensitive to the applied magnetic field and the operating frequency. The present chapter describe in greater detail the field and frequency-dependent variations on the complex torsional stiffness and damping of the developed isotropic MRE isolator. The operating frequencies are varied between 10 Hz to 30 Hz in steps of 5 Hz. The field-dependent variations are studied by varying the applied field between 0T to 0.28 T. To ensure the linear response of the MRE isolator, the input angular displacement is kept constant at 0.008 rad. The experiments are carried out on the test setup built as per the ISO standard, as discussed in Chapter 3. Also, the field-dependent variations are further explored using numerical simulations with Ansys 19.1.

4.2. Relationship between Blocked Torque and Input angular displacement

Figure 4-1 shows the variations in the output torque at 0T, 0.12T and 0.28T at the input frequency of 10Hz. It is observed that the output torque increases with an increase in the input current. For 0T, the maximum amplitude of torque observed is 0.0409 N.m. With an increase in the magnetic field, the amplitude increases and a maximum value of 0.0449 N.m is obtained at 0.28T. A similar trend is observed for the rest of the tested frequencies (Figure 4-2). It is seen that the obtained Lissajous curves are a symmetrical ellipse, which signifies that the MRE is within the Linear Viscoelastic Limit (Agirre-Olabide and Elejabarrieta 2018). With an increase in field, the Lissajous curves show an increase in the slope, as observed in the inset of Figure 4-2. For a viscoelastic material like MRE, the slope of the Lissajous curves represent the complex stiffness. The variations in the complex stiffness highlight the field-induced stiffening of the MRE (Sec. 4.3). Additionally, the complex stiffness is affected by the input frequency (Sec. 4.4).

Further, the area under the Lissajous curves represents the energy dissipation capacity of the MRE. It is observed that the area of the Lissajous plots varies with the input parameters. These variations in the energy dissipation capacity are also expressed in terms of the Loss factor, which is the ratio of the energy dissipating term (K'') to the

stiffness term (K'). The field-dependent and frequency-dependent variations in the loss factor are explained in sec 4. 5.

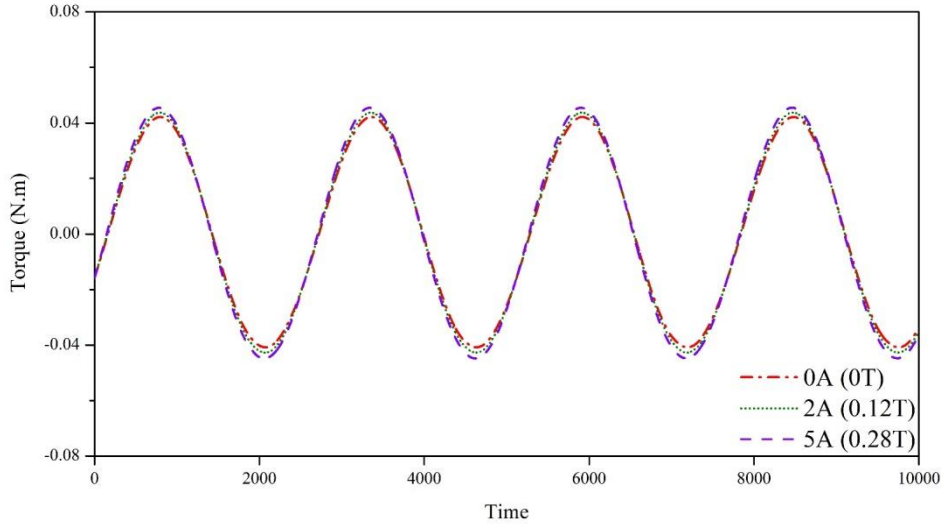

Figure 4-1: Output torque variations with varying input current

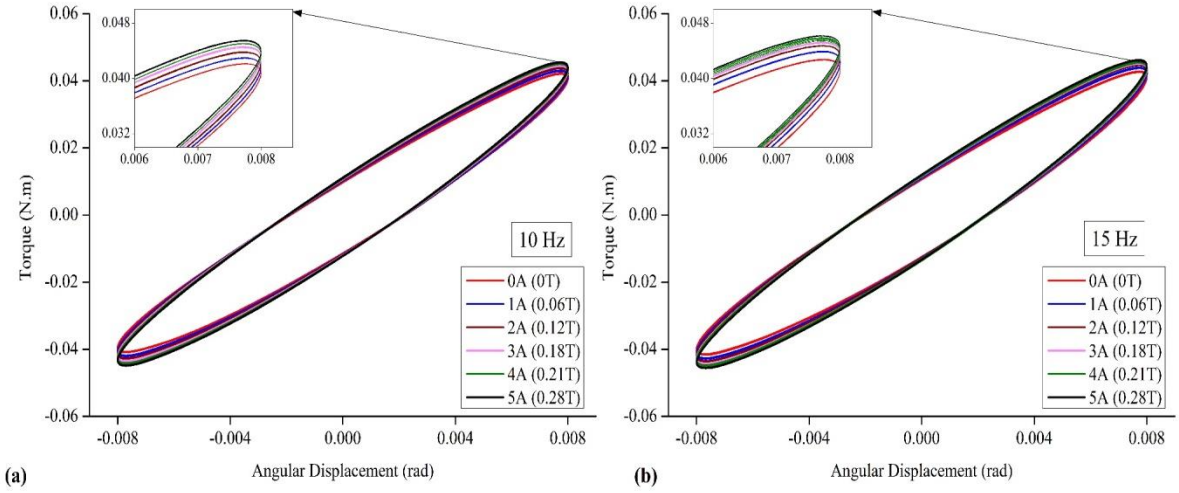

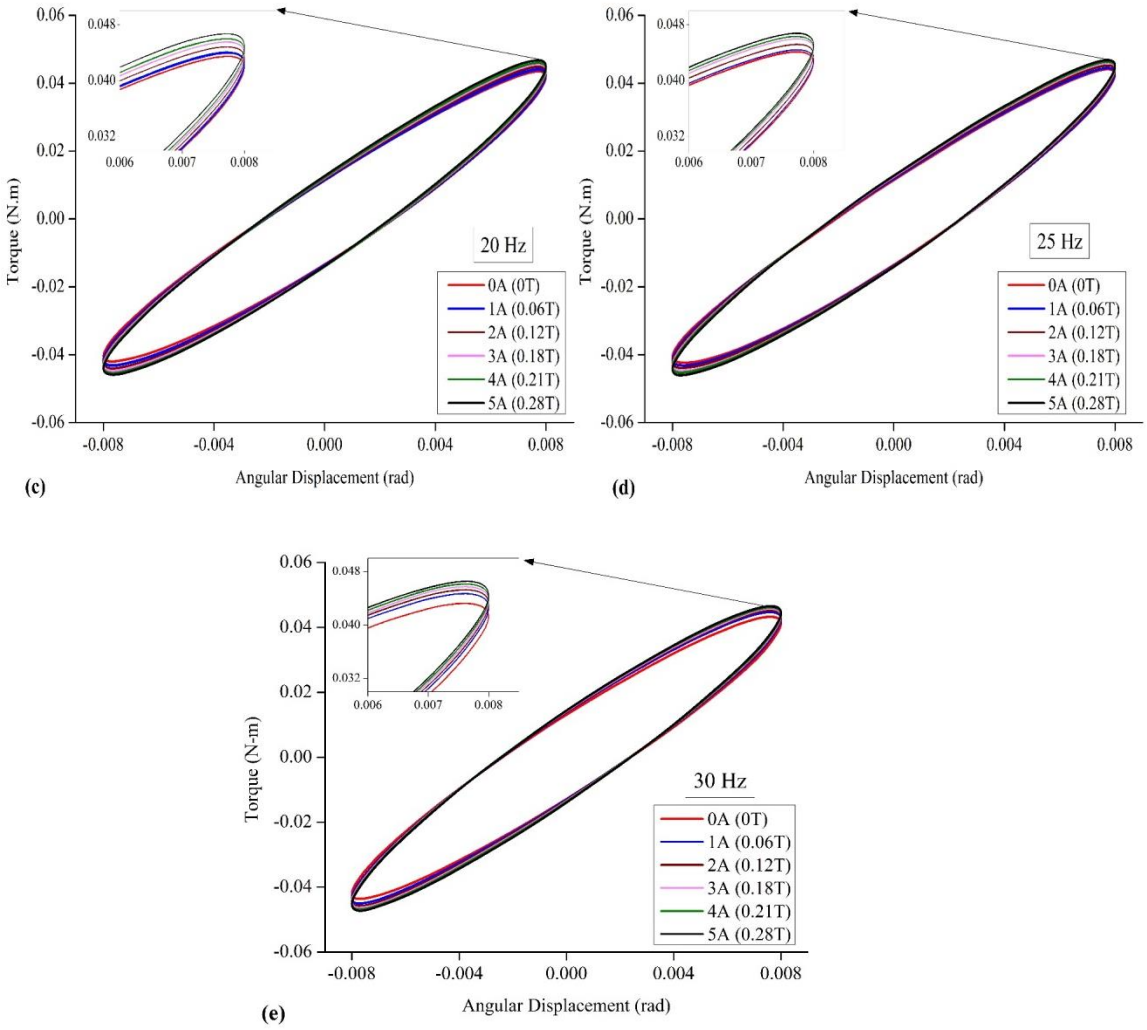

Figure 4-2: Variations in field-dependent Lissajous curves for different input frequencies (a) 10Hz (b) 15Hz (c) 20Hz (d) 25Hz (e) 30Hz at a constant angular displacement of 0.008 rad

4.3. Complex stiffness variations with the magnetic field

The complex stiffness values are calculated from the Lissajous curves (Figure 4-2 a-e) from Equation (3.1 and the corresponding values are listed in Table 4.1 for varying input fields and frequencies. It is observed that the complex stiffness of the MRE sample increases with an increase in the magnetic field. A similar trend is observed in the complex stiffness values of MRE for translatory shear conditions(Poojary et al. 2017). The enhancement in the complex stiffness across varying magnetic fields is expressed using the MR effect. MR effect is defined as the percentage ratio of the

difference in complex stiffness between a given magnetic field and zero-field to the complex stiffness at zero-field. The dynamic torsional stiffness at 10Hz, 0T, is found to be 5.194 N.m/rad. Corresponding value at 0.28T is 5.65 N.m/rad, with an overall enhancement of 8.87%. A similar trend is observed for the rest of the frequencies.

Table 4.1: Complex stiffness for varying current and absolute MR effect variations

Freq (Hz)	K_t^*(N.m rad^{-1})						Absolute MR Effect
	0T	0.06T	0.12T	0.18T	0.21T	0.28T	
10	5.194± 0.092	5.316± 0.089	5.419± 0.096	5.518± 0.090	5.581± 0.097	5.651± 0.096	8.87 %
15	5.277± 0.090	5.424± 0.090	5.524± 0.090	5.61± 0.094	5.698± 0.094	5.741± 0.093	8.79 %
20	5.353± 0.094	5.466± 0.091	5.564± 0.090	5.653± 0.096	5.721	5.791± 0.091	8.26 %
25	5.419± 0.097	5.481± 0.094	5.576± 0.093	5.677± 0.093	5.732± 0.094	5.812± 0.093	7.25 %
30	5.437± 0.091	5.612± 0.094	5.701± 0.093	5.761± 0.090	5.821± 0.097	5.871± 0.093	7.98 %

The Increase in the complex stiffness is attributed to the field enhanced interactions between the ferromagnetic fillers. In the absence of the magnetic field, iron particles are embedded within the matrix, which enhances its zero-field stiffness compared to the unfilled elastomer. Under the influence of the magnetic field, iron particles act as magnetic poles, which improves the filler-filler interactions. This force of attraction between the iron particles causes a localized compression of the matrix.

Figure 4-3 (a) shows the SEM image of the MRE with CIP entrapped between the silicone matrix under zero magnetic fields. Figure 4-3 (b) shows the enlarged view of a typical cross-section of the elastomer in the absence and presence of the magnetic field under an external strain. The iron particles displace with a change in separation distance (r_0 to r). In the presence of an external magnetic field, the interaction energy between two iron particles of radius '*a'*, is given as (Shen et al. 2004),

$$E_{12=}\frac{1}{4\pi\mu_0\mu_1}\left[\frac{m_1m_2}{r^3}-\frac{3}{r^5}(m_1r)(m_2r)\right] \tag{4.1}$$

Where

m_1 and m_2 represent the dipole moment of the two iron particles

r_0 and r represents the separation distance between the two particles without and with the presence of field

μ_0 and μ_1 represent the permeability of the vacuum and relative permeability of the elastomer.

Further, the force between the two particles (F) is given as,

$$F = \frac{dE}{dr}\sin\alpha \tag{4.2}$$

Where α' is the angle between the displaced position with the un-displaced position of the CIP. Assuming constant dipole moments, $m = m_1 = m_2$. Hence,

$$\Longrightarrow F = \frac{3}{2}C\frac{(5{r_0}^2 - r^2)m^2\sqrt{r^2 - {r_0}^2}}{\pi\mu_0\mu_1 r^7} \tag{4.3}$$

Where $C = 1.2$ for a larger number of filler particles

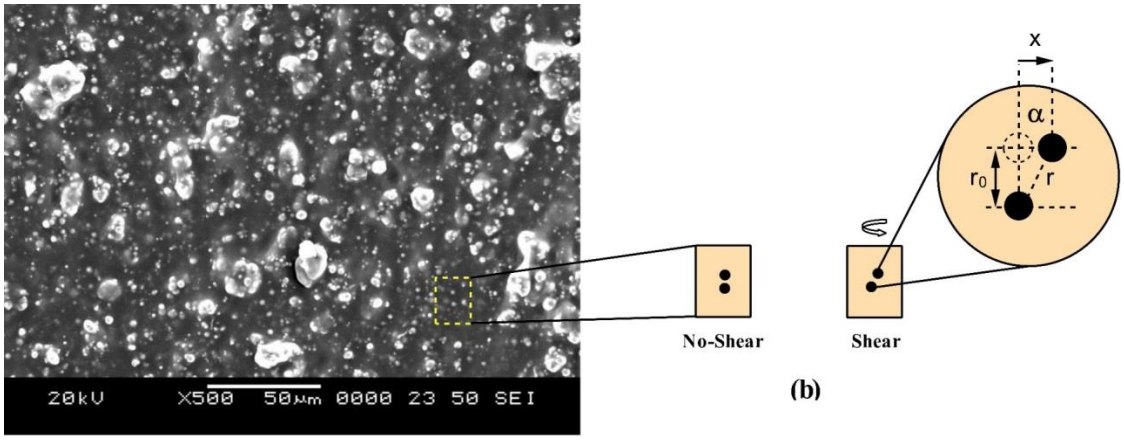

Figure 4-3: (a) SEM image of isotropic MRE (b) Dipole interactions during torsional shear

The effect of the magnetic force on the embedded matrix is substantiated through the magnetostatic and static structural numerical simulation. Figure 4-4 depicts the 2D model developed in ANSYS 19.1, APDL. A unit cell of MRE with iron particles of diameter 4µm and a separation distance of 6µm is considered. The magnetic field is induced between the poles using two permanent magnets (Alnico; Coercivity 109300

A/m). To focus the field lines on the iron particles, a C-shaped path is generated using a permeable material. The magnetic force generated in unstrained and strained cases of the iron particles is obtained from the magneto-static analysis. The magnetic force generated is used to obtain the mechanical strain and displacement on the iron particles by performing static structural analysis.

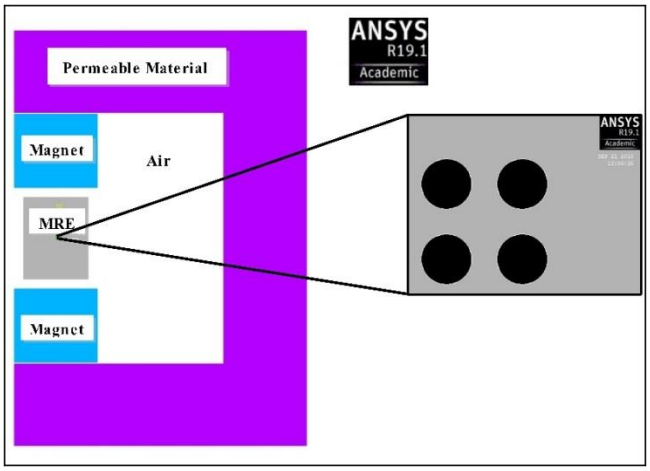

Figure 4-4: 2D model of the setup

The simulation results of a unit cell in the unconstrained and constrained conditions are shown in Figure 4-5. In the unconstrained position of the MRE, the iron particles are aligned in the direction of the magnetic field. The magnetic flux generated exerts a force of attraction between the iron particles (Figure 4-5, a). In the presence of an external torque, the iron particles attain new positions which increase the separation distance between the dipoles. The separation results in the reduction of the magnetic force on the iron particles as observed from the magnetic force contour plots (Figure 4-5 b). The developed magnetic force of the iron particles exerts a compressive force on the embedded matrix, which increases the localized complex stiffness of the MRE. Figure 4-5 c shows the mechanical strain of the iron particles, which indicates the compression caused by the iron particles on the matrix.

It is observed that the absolute variations in the MR effect are limited to a maximum of 8.87%. These variations are ascribed to the influence of the thickness of the MRE sample on magnetic field intensity. The torsional stiffness, K_t, for the elastomer sample of thickness t_h, radius r_s and shear modulus G, is given as (Gent 2012),

$$K_t = \frac{\pi G {r_s}^4}{2t_h} \tag{4.4}$$

Under the zero magnetic field, stiffness of the sample for the unstrained and strained conditions is dependent on the geometrical parameters, as represented in the above equation. Under the influence of the magnetic field, the complex stiffness increases with an increase in the magnetic field. However, the increase is inversely dependent on the thickness of the MRE. To comprehend the influence of the sample thickness on the magnetic force, two samples of variable thickness are considered. In both cases, a separation distance of 2 mm is maintained between the MRE sample and the permanent magnets on either side. The increase in sample thickness is represented by the increase in the number of iron particles, as shown in Figure 4-5 d.

The simulation results illustrated in Figure 4-5 d suggest that, for a fixed distance between the sample and the magnetic poles, the magnetic force generated on the individual iron particles reduces with the increase in the thickness of the sample. The reduced magnetic force signifies the reduction in the displacement of the iron particles in comparison with the thinner samples, as displayed in Figure 4-5 c. Due to the reduced displacement, the interaction energy (Equation (4.1) between the dipole decreases, leading to the reduction of the compressive force exerted on the embedded matrix. This reduction leads to the reduced MR effect of the test sample. Thus, the overall effect of the geometry and intensity of the magnetic field influences the field-induced variations on the MRE. The problem can be addressed by increasing the magnetic field across the MRE. Though it does increase the MR effect, however, the relative shift in the field-dependent absolute stiffness reduces with an increase in the thickness of the MRE (Johnson et al. 2018). Moreover, from Table 4.1, it is observed that the trend remains the same for all the tested frequencies.

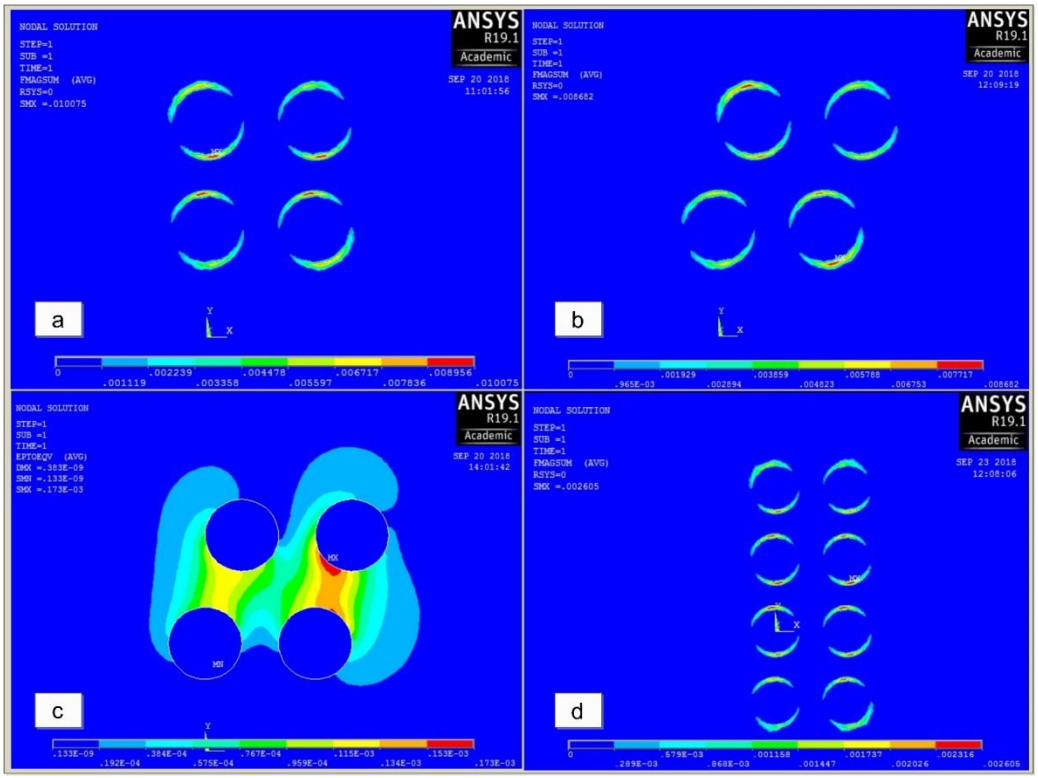

Figure 4-5: Magnetic force generated on iron particles in (a) unstrained condition and (b) strained condition; (c) Mechanical strain on iron particles under strained condition; (d) Influence of increase in thickness on the magnetic force of the particles

4.4. Complex stiffness variations with frequency

Figure 4-6 depicts the Lissajous plots of blocked torque and angular displacement for 10 Hz, 20 Hz and 30 Hz at 0T and 0.28T, respectively. The plots reveal a small shift in the slope with an increase in the frequency from 10 Hz to 30 Hz. The effect is further illustrated by the maximum amplitude of torque, as portrayed in Figure 4-1. At 0T, 10 Hz frequency, the maximum torque experienced by the MRE is 0.0409Nm. The corresponding value at 30 Hz frequency is 0.0436 Nm, with an increase in torque of 6.67%. The shift in the complex stiffness is attributed to the frequency-dependent characteristics of the viscoelastic material under dynamic loading conditions.

MRE, by virtue of its polymer matrix, exhibits frequency-dependent characteristics (Tian et al. 2011a). At lower frequencies, the polymer chain molecules have adequate time to return to their original positions, allowing it to behave like viscous material. At higher frequencies, these polymer chains have less time to relax.

Consequently, the elastic part dominates over the viscous part. The overall effect is visible in terms of enhancement in the stiffness with the input frequency. The addition of filler into the matrix, however, induces a composite behavior into the MRE sample, which increases the resistance to the cyclic loading at lower frequencies. The micro-nano sized particles embedded within the matrix results in the coexistence of filler-matrix interaction alongside the matrix-matrix interaction. This enhances the stiffness of the elastomer at lower frequencies due to which the increase in the frequency-dependent increment in the complex stiffness is not as dominant as seen in unfilled elastomers.

The frequency-dependent stiffness variation is evaluated in the form of the absolute enhancement in the torsional stiffness from 10 Hz to 30 Hz and is given as,

$$\text{Absolute enhancement in the frequency}-\text{dependent stiffness} = \left(\frac{K^*_{t(30\text{Hz})} - K^*_{t(10\text{Hz})}}{K^*_{t(30\text{Hz})}}\right) \times 100 \qquad (4.5)$$

As evident from Table 4.1, it is observed that, under the absence of a magnetic field, the absolute enhancement in the frequency-dependent stiffness from 10 Hz to 30 Hz is restricted to 4.68%. It is also seen that, with an increase in the magnetic field to 0.28T, the enhancement observed is 3.82%. Likewise, it is observed that the frequency induced enhancement of the complex stiffness is relatively less when compared with the field-induced variations seen in the stiffness. While the maximum shift in the field-dependent complex stiffness observed is 8.87%, the frequency-dependent enhancement is limited to 5.59%. The values demonstrate the weak frequency-dependent enhancement in the complex stiffness of the MRE in the absence as well as in the presence of a magnetic field.

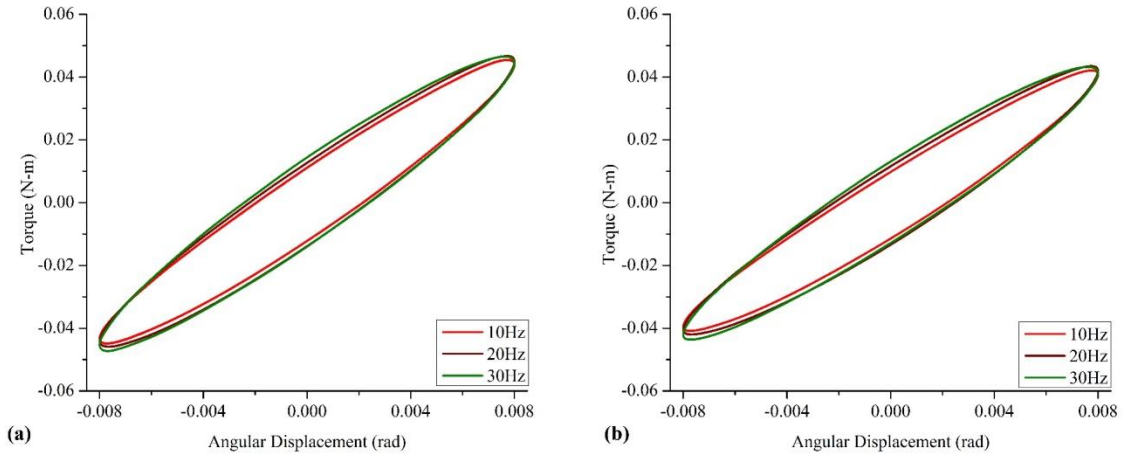

Figure 4-6: Frequency-dependent complex torsional stiffness variations at (a) 0T (b) 0.28T

4.5. Loss factor variations with field and frequency

The loss factor represents the energy dissipation capacity of the material. The variations in the loss factor of the MRE under torsional loading at different input current and excitation frequencies are as shown in Figure 4-7. As evident from the graph, the loss factor increases with an increase in the frequency (Agirre-Olabide and Elejabarrieta 2018). However, the field-induced variations are not significant in the variations of the loss factor. At 10 Hz, the loss factor varies from 0.238 to 0.258, with an increase in the field from 0T to 0.28T. Correspondingly, for 30 Hz, the loss factor varies from 0.299 to 0.316. This typical characteristic of the MRE is attributed to the field-dependent variations observed in the storage stiffness and loss stiffness of the complex stiffness.

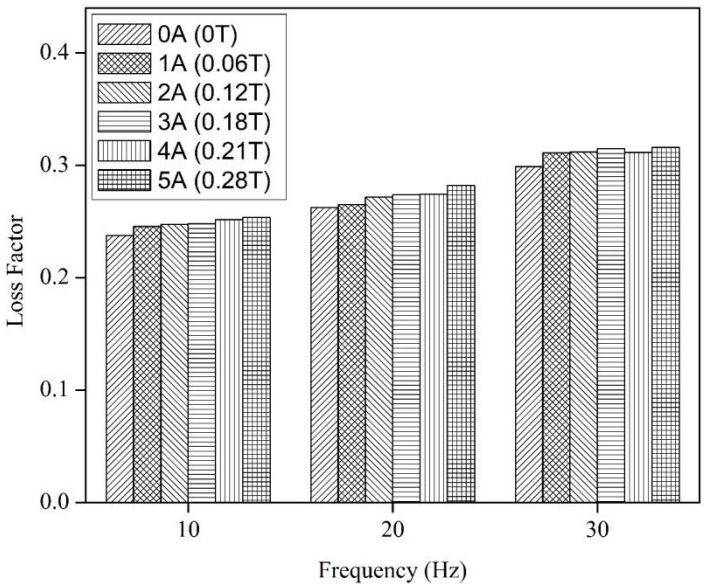

Figure 4-7. Loss factor under different magnetic field and frequency

As depicted in Figure 4-8, the storage stiffness (K') and the loss stiffness (K'') enhance with the increase in the magnetic field. However, the relative enhancements vary with the intensity of the input current. It is observed that for the 10 Hz input frequency, the absolute enhancement of the K' is 7.84%, with an increase in the magnetic field from 0T to 0.28T. Similarly, it is observed that the loss stiffness, K'' has an absolute increment of 15.06%. Consequently, these variations influence the field-dependent variations in the loss factor.

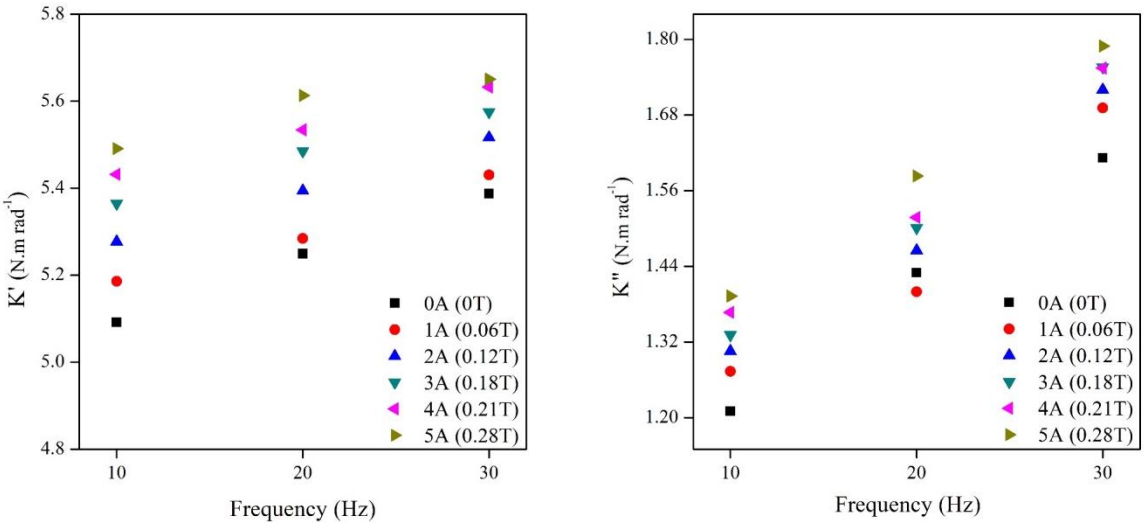

Figure 4-8: Field dependent variations in (a) K' (b) K''

4.6. Summary

The assessment of the field dependency and the influence of the operating frequency forms the crucial step in the characterization of the MRE isolator. In the present chapter, the influence of the aforementioned parameters has been discussed. The properties of the MRE isolator has been characterized as per the ISO 10846-2 discussed in Chapter 2. The characterization is carried out within the Linear Viscoelastic Limit, with the angular displacement restricted to 0.008 rad. For the range of parameters comsidered, the results indicate that the magnetic field dependence is stronger compared to the frequency-dependent characteristics. The field-induced variations are explained with the Magneto-static and structural based numerical simulations. The isolator, due to its filled characteristics, exhibits frequency dependency. Although the effect of the frequency is reduced in comparison with the applied field, the MRE isolator does exhibit the effect for the range of 10Hz to 30Hz. Furthermore, the loss factor also suggests similar dominance of the field-induced variations, over that of the operating frequency.

With the field and frequency dependency discussed in the present chapter, the next chapter discusses the angular displacement dependent variations on the properties of the MRE.

5. Dynamic characterization of angular displacement dependent variations on the characteristics of MRE isolator

5.1. Introduction

Apart from the field and frequency-dependent behavior, the dynamic properties of the magnetorheological elastomers are primarily affected by variations in the input displacement. To substantially evaluate its isolation capabilities, it is quintessential to comprehend the displacement dependent variations on the complex stiffness and the loss factor of the MRE. The present chapter focuses on studying the influence of angular displacement on the field-dependent dynamic properties of the Magnetorheological Elastomer isolator under torsional loading conditions.

The angular displacement dependent variations are carried out as per the procedures discussed in Chapter 0. The input angular displacements are varied between 0.002 rad to 0.016 rad for the frequency between 10Hz to 30Hz. Displacement is maintained within the linear viscoelastic limit, which is determined from the shape of the torque-angular displacement hysteresis plot. The magnetic field is varied, between 0T to 0.28T.

5.2. Influence of angular displacement om the rheological properties

The angular displacement influenced characteristics of the MRE are assessed from the torque-angular displacement hysteresis plots. Figure 5-1 (a-e) shows the hysteresis plots of varying angular displacements for input frequencies of 10, 15, 20, 25 and 30 Hz, respectively. As well as the effect of the magnetic field at 0T, 0.18T and 0.28T on the hysteresis plots are observed. It is evident from Figure 5-1 (a-e) that the obtained hysteresis curves are symmetrical about the axis, signifying that the results are within the Linear Viscoelastic (LVE) Limit (Agirre-Olabide and Elejabarrieta 2018). What is interesting in these figures is the noticeable reduction in the slope of the hysteresis curves with the increase in the angular displacement. The observation is true in the absence and the presence of the magnetic field, signifying the displacement-dependent reduction in the dynamic torsional stiffness of the MRE.

Figure 5-2 depicts the dynamic torsional stiffness values obtained from the slope of the hysteresis curves. It is seen that the stiffness values reduce with an increase

in the angular displacement. In the absence of a magnetic field, the torsional stiffness corresponding to 10 Hz reduces from 5.487 N.m rad^{-1} to 4.94 N.m rad^{-1} with an increase in the angular displacement from 0.002 rad to 0.016 rad. A similar trend is observed with an increase in the frequency to 30 Hz. in the presence of the magnetic field, the stiffness reduces from 5.848 N.m rad^{-1} to 5.379 N.m rad^{-1} for 10 Hz and from 6.074 N.m rad^{-1} to 5.691 N.m rad^{-1} for 30 Hz. The decreasing trend suggests that the dynamic torsional stiffness behaves on similar lines as that of the dynamic stiffness obtained under lateral shear(Poojary and Gangadharan 2016).

The reduction in the values is attributed to the displacement-dependent characteristics observed in viscoelastic materials (Payne and Whittaker 1970)(Zhang et al. 2007). For a filled viscoelastic material, the dependency of the input displacement on the torsional stiffness is explained either by the interactions between the adjacent filler particles (filler-filler interactions) or the interactions between the filler particle and the surrounding matrix (filler-matrix interactions). Filler-filler interactions are a characteristic feature observed in the nano-sized particles which are accredited to the agglomeration of the particles(Payne 1962). Alternatively, the filler-matrix interaction, also termed as bound rubber, is attributed to the adhesion of matrix layer on the surface of the filler particles and is observed in micro-sized as well as the nano-sized filler particles(Zhang et al. 2007). Reduction in the dynamic stiffness in filler-filler interactions occurs due to the constant aggregation and disaggregation of the filler particles under the harmonic loading conditions. On the other hand, bound rubber theory follows the bonding and debonding of the rubber strands, which results in the reduction of intact rubber strands on the filler boundary, reducing the overall stiffness offered by the MRE. The bound rubber model can be effectively used to describe the displacement-dependent reduction seen in the MRE under the torsional loading condition.

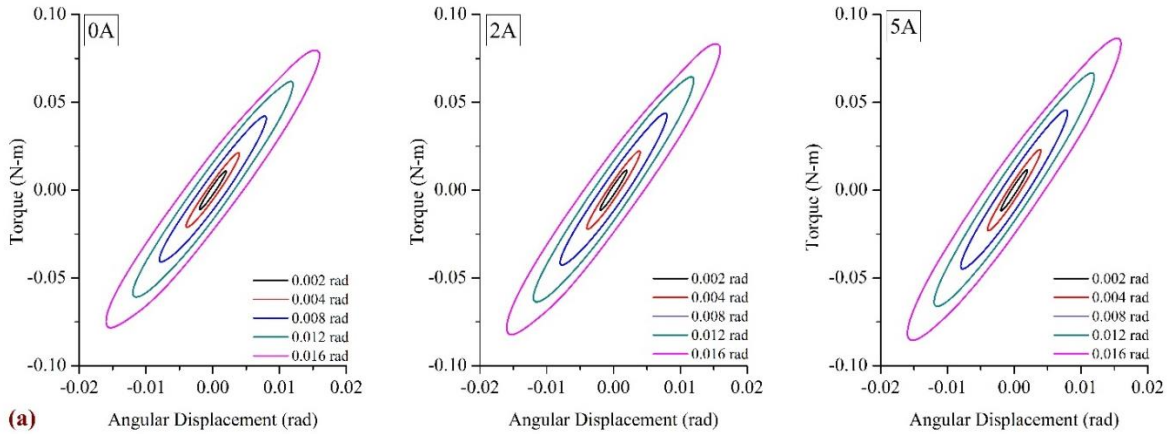
0A
2A
5A
Torque (N-m)
Angular Displacement (rad)
0.002 rad
0.004 rad
0.008 rad
0.012 rad
0.016 rad
(a)

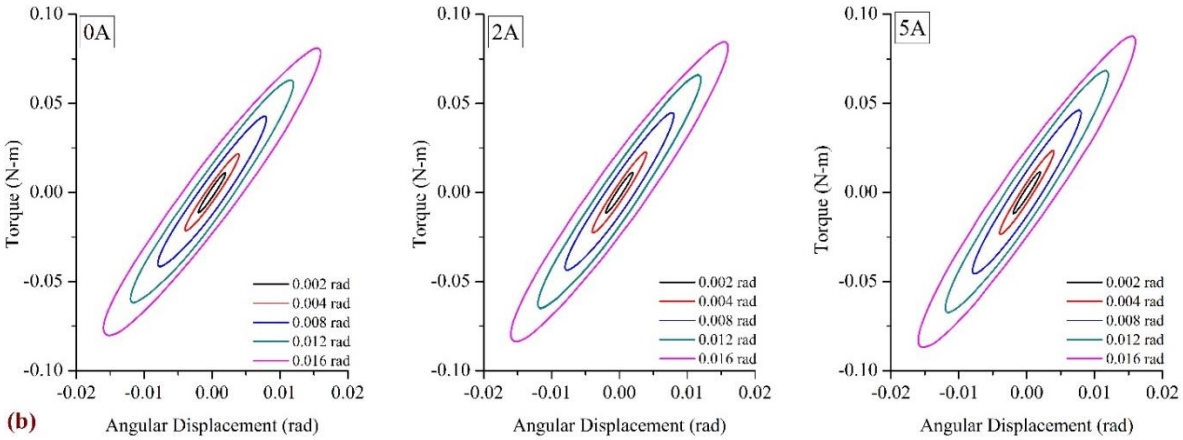
0A
2A
5A
Torque (N-m)
Angular Displacement (rad)
0.002 rad
0.004 rad
0.008 rad
0.012 rad
0.016 rad
(b)

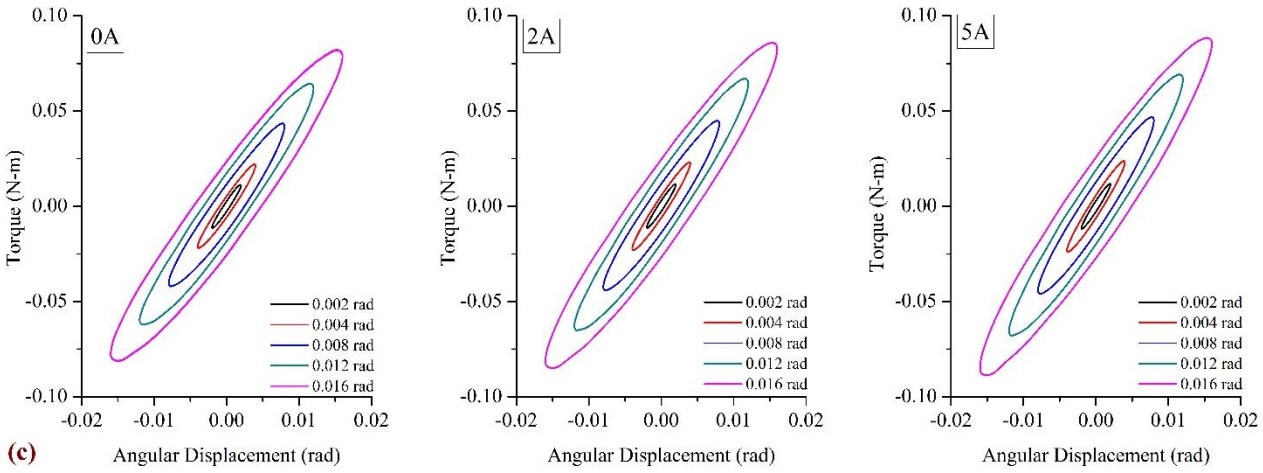
0A
2A
5A
Torque (N-m)
Angular Displacement (rad)
0.002 rad
0.004 rad
0.008 rad
0.012 rad
0.016 rad
(c)

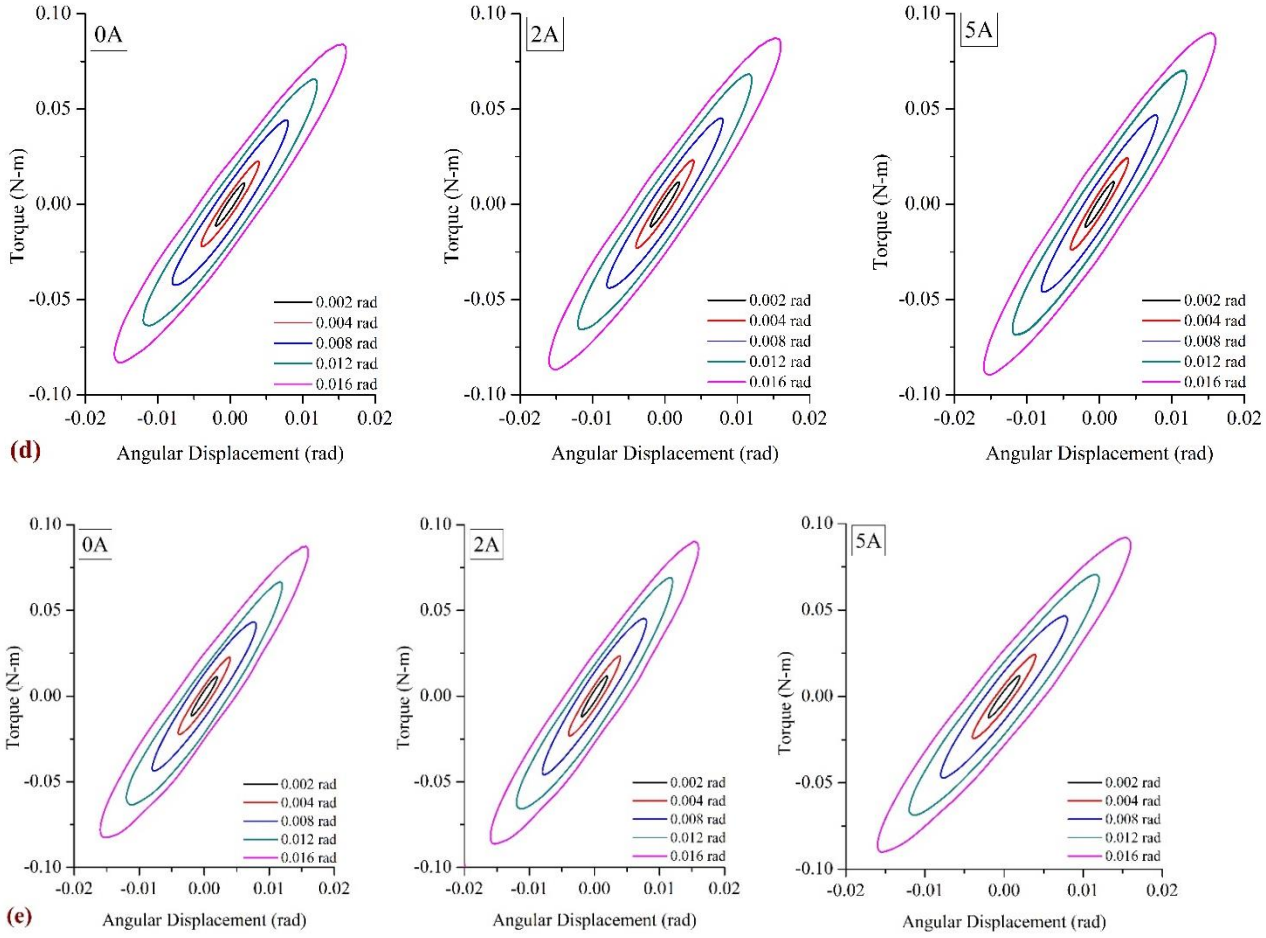

Figure 5-1: Hysteresis curves of Torque-Angular displacement for varying angular displacements and magnetic fields at (a)10 Hz (b)15Hz (c)20Hz (d)25Hz (e)30Hz

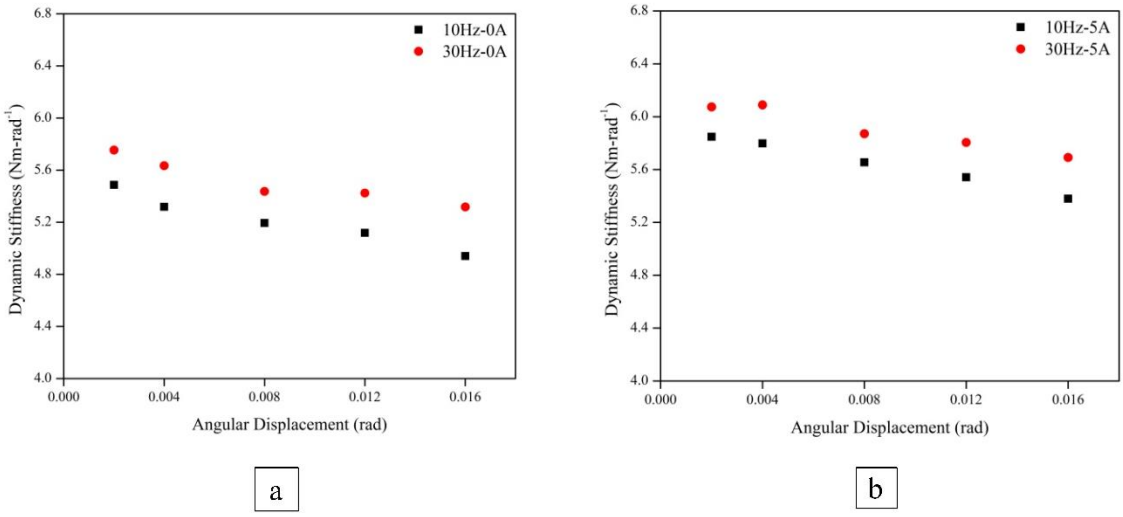

Figure 5-2: Variations in the dynamic torsional stiffness for varying angular displacements for (a) 0T and (b) 0.28T

5.3. Angular Displacement-induced variations in dynamic torsional stiffness

The reduction in the dynamic torsional stiffness of the MRE with the increase in the input angular displacement is explained using the bound rubber theory (Zhang et al. 2007). For filled elastomers, the filler and the viscoelastic matrix form a bond during the process of curing, resulting in the formation of a network. Termed as "Bound rubber", this refers to the rubber available in the transition layer between the CIP and the interlaying bulk rubber. The bound rubber is inherently much stiffer in comparison with the rest of the interlaying rubber matrix. Effectively, the shear modulus of bound rubber is given as (Zhang et al. 2007),

$$G' = G_0 \left[1 + 2.5 \left(\frac{R + wt}{R} \right)^3 \emptyset + 14.1 \left(\frac{R + wt}{R} \right)^6 \emptyset^2 \right] \tag{5.1}$$

Where *R* represents the radius of the CIP, *t* represents the thickness of the bound rubber, G_0 represents the zero-field shear modulus, *ø* represents the volume fraction of the particles and *w* is the power coefficient. It is observed that increasing the thickness of the bound rubber results in the increase of the shear modulus or otherwise the dynamic torsional stiffness offered by the MRE. It also describes the increase in the stiffness of filled elastomers compared to their unfilled matrices.

Figure 5-3(a) shows the SEM image of the isotropic MRE. As depicted in Figure 5-3 (c), the bound rubber consists of two layers, namely the tightly bound rubber and the loosely bound rubber(Leblanc 2002)(Fan et al. 2010). The tightly bound rubber refers to the layer of the bound rubber tightly adhered to the surface of the iron particles. The loosely bound rubber interacts with the interlaying bulk rubber and forms a chain-like structure between the iron particles and the surrounding interlaying rubber through the tightly bound layer. In the absence of the external torsional shear, the bound rubber surrounding the CIP lay intact. However, in the presence of external shear, the MRE deforms which increases the relative motion between the bulk rubber and the CIP. In the absence of additives, the thickness of the loosely bound layer is reduced which results in the reduction of the interfacial adhesion between the CIP and the surrounding matrix. In the presence of the external shear, the matrix deforms in the direction of the applied shear, during which the bound matrix is unable to follow the shear deformation due to its weak interaction with the bulk rubber. The weak adhesion results in the

breakage of the chain-like formation between the CIP and the bulk rubber resulting in the formation of a gap between the bound rubber and the bulk rubber (Figure 5-3 d). It results in the reduction of the dynamic stiffness offered by the MRE as well as in the reduction of the magnetic force between the interlaying carbonyl iron particles. Further, due to the presence of the gaps, the permeability reduces, thus resulting in the reduction of the magnetic force experienced by the individual CIP. This reduction is amplified when the bulk of the MRE is considered(Wang et al. 2006)(Li et al. 2012c). The thickness of the loosely bound layer can be increased with the addition of additives, which significantly influences the interaction between the CIP and the interlaying bulk rubber(Fan et al. 2010). the agglomeration of the iron particles entraps the rubber chains resulting in the formation of trapped rubber (Khimi and Pickering 2015) (Wang 1998), as portrayed in Figure 5-3 (b). This leads to an increase in stiffness offered by the MRE.

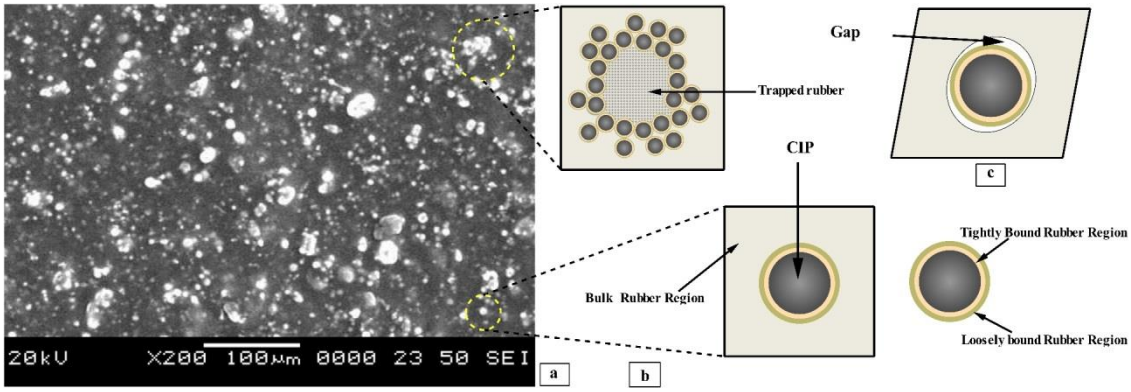

Figure 5-3: (a) SEM image of isotropic MRE (b) Schematic representation of the trapped rubber (c) Representation of Bound rubber (d) Presence of gap during torsional shear

Apart from the thickness of the loosely bound rubber, the interaction between the loosely bound rubber and the CIP plays a dominant role in the reduction of the dynamic torsional stiffness of the MRE. The existence of bound rubber is attributed to the force of attraction due to various factors such as the dispersion force, the inductive force or due to the force which exists due to the dipole interactions (Stacer et al. 1990). In the absence of the external shear (Figure 5-4a), the loosely bound rubber strands adhere to the surface of the CIP through the tightly bound region (Stacer et al. 1990)(Ladouce-Stelandre et al. 2003). Under harmonic angular displacement (Figure 5-4 b), the iron particles get displaced in the direction of the applied torsional shear.

The displacement (*D'*) causes the bonding-debonding of the loosely bound rubber strands attached to the CIP, as observed in lateral shear (Poojary and Gangadharan 2016). For smaller displacements, the bonding-debonding is insignificant and the breakage of the strands from the surface of the CIP is at a reduced rate (Figure 5-4 b). However, with an increase in the angular displacement, the debonding of the loosely bound strands overwhelms the bonding process, which results in the reduction of the number of intact bonds present in the bound rubber region (Figure 5-4 c). This decreases the resistance offered by the bound rubber region to the external torsional shear, resulting in the reduction of the overall stiffness offered by the MRE. In the presence of the magnetic field, the CIP act as dipoles(Jolly et al. 1996a) which results in the development of a force of attraction between the neighboring iron particles (Figure 5-4 d). The attractive force, in turn, induces a compressive force on the interlaying matrix, which in turn results in better adhesion of the bound rubber strands on the CIP surface (Figure 5-4 e and f). With the increased adhesion, the number of intact bonds increases, which leads to a decrease in the displacement induced reduction of the dynamic torsional stiffness of the MRE. The effect can be explicated by the displacement induced reduction in stiffness without and with the application of a magnetic field. Figure 5-5 shows the percentage reduction in the values of the absolute stiffness in the absence and presence of the magnetic field across varying input frequencies. The percentage reduction in displacement induced dynamic torsional stiffness is given as,

$$Reduction\ in\ dynamic\ torsional\ stiffness\ (\%) = \left(\frac{(dynamic\ torsional\ stiffness)_{0.002\,rad} - (dynamic\ torsional\ stiffness)_{0.016\,rad}}{(dynamic\ torsional\ stiffness)_{0.002\,rad}}\right) X\ 100 \quad (5.2)$$

It is observed that in the absence of the magnetic field, the percentage reduction in dynamic torsional stiffness is 9.96% for 10 Hz when the angular displacement is increased from 0.002 rad to 0.016 rad. This reduces to 8.02%, with an increase in the magnetic field to 0.28T. A similar effect is seen for the rest of the tested frequencies, which suggests that the displacement induced reduction in the dynamic torsional stiffness is more pronounced for the non-magnetized states of MRE and application of the magnetic field improves the bonding of the CIP and the bound rubber

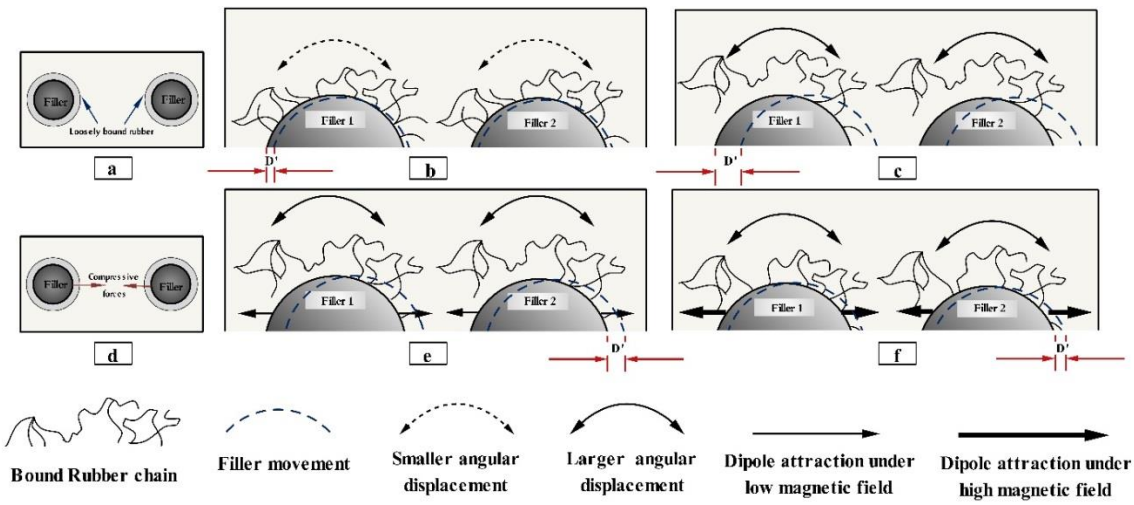

Figure 5-4: (a) Schematic of loosely bound rubber adhered to the surface of the CIP. Bonding-Debonding under the absence of the magnetic field at (b) lower angular displacement (c) Higher angular displacement (d) Compressive forces in the presence of a field. Bonding-Debonding under the presence of (e) Lower magnetic field (f) higher magnetic field

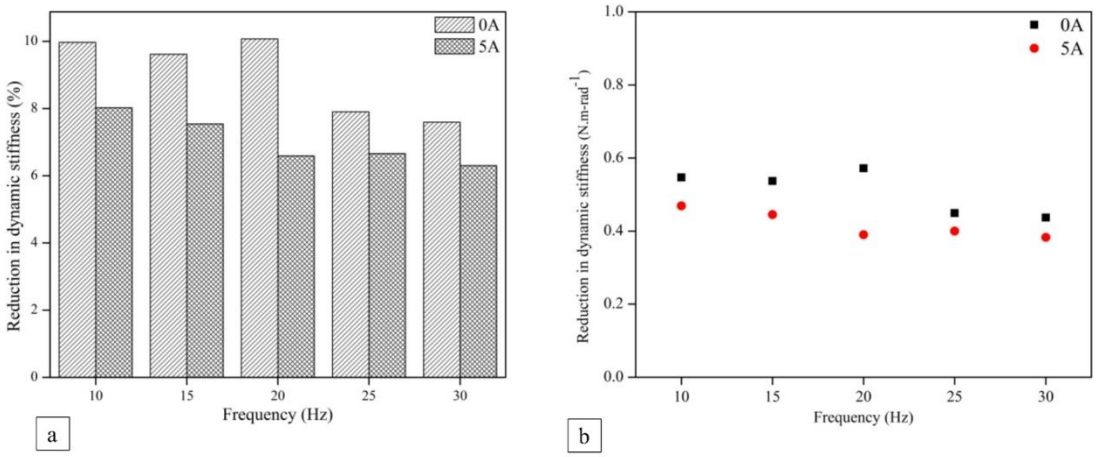

Figure 5-5: (a) Variations in displacement induced percentage reduction in the dynamic torsional stiffness for 0T and 0.28T (b) Effect of frequency on the displacement induced reduction in dynamic stiffness

Additionally, it is observed from Figure 5-2 that the dynamic torsional stiffness of the MRE increases with an increase in the magnetic field, signifying the field-induced stiffening of the MRE. The field-induced enhancement in the dynamic stiffness is referred to as the MR effect(Poojary et al. 2018)(Lee and Kim 2018). As explained earlier, the Absolute MR effect is defined as the percentage ratio of the difference in

the torsional stiffness values between a given magnetic field and zero-field to the torsional stiffness value at zero-field. As shown in Table 5.1, for a constant angular displacement of 0.002 rad, the zero-field dynamic stiffness for 10 Hz input frequency is 5.487 Nm rad^{-1}. In the presence of a magnetic field, the value increases to a maximum of 5.848 Nm rad^{-1} at 0.28T, with an overall increase in the absolute MR effect to be 6.57%. A similar trend is observed for the rest of the tested angular displacements. The enhancement in the dynamic torsional stiffness is attributed to the formation of dipoles between the iron particles, which induces a compressive force on the embedded matrix(Poojary et al. 2016). This results in increased resistance to the deformation of the MRE under the external torsional loading resulting in increasing the dynamic torsional stiffness of the MRE.

Table 5.1: Absolute MR Effect across varying angular displacement at 10Hz input frequency

Angular Displacement (rad)	K_t^* (N.m rad^{-1})		$K^*_{t5} - K^*_{t0}$ (N.m rad^{-1})	Absolute MR Effect (%) $\left(\frac{K^*_{t5} - K^*_{t0}}{K^*_{t0}}\right) \times 100$
	(0T)	(0.28T)		
0.002	5.487	5.848	0.361	6.57
0.004	5.318	5.798	0.48	9.02
0.008	5.194	5.655	0.461	8.87
0.012	5.118	5.542	0.424	8.28
0.014	4.94	5.378	0.438	8.86

Besides, Figure 5-2 reveals the frequency-dependent variations on the dynamic torsional stiffness values of the MRE. In the absence of magnetic field, it is observed that the torsional stiffness increases from 5.487 N.m rad^{-1} to 5.754 Nm rad^{-1} with an increase in the frequency from 10 Hz to 30 Hz. A similar trend is observed in the presence of the magnetic field. The shift in the torsional stiffness is accredited to the frequency-dependent properties of the filled viscoelastic composites under harmonic loading conditions(Tian et al. 2011b). An increase in the frequency offers less time for

the polymer chains to relax, which increases the resistance offered by the MRE to deform. The reduced resistance leads to the increase of the dynamic torsional stiffness. Although the effect is less for filled elastomers, the relative increase in the dynamic stiffness is observed from the values shown in Figure 5-2. Further, Figure 5-5 b shows the dominance of the frequency-dependent increase over the angular displacement-dependent reduction in the dynamic stiffness of the MRE. The frequency-dependent variations predominate the rate at which the reduction in the stiffness occurs due to the bonding-debonding of the iron particles with the bound rubber

5.4. Angular Displacement-induced variations in Loss factor

Figure 5-1 shows that the area under the hysteresis curves varies with the angular displacement, signifying the variable damping properties of the MRE under torsional loading conditions. The energy dissipation in MRE is understood from the variations observed in the loss factor. Figure 5-6 shows the displacement-dependent variations in the loss factor of the MRE for 10Hz, 20Hz, and 30Hz across varying input current. Similar to the lateral shear(Garcia Tarrago 2006) (Gong et al. 2012), it is observed that the loss factor increases with an increase in the input angular displacement for the tested frequencies. This variation in the loss factor is attributed to the influence of external shear and is explained by the damping capacity of the MRE.

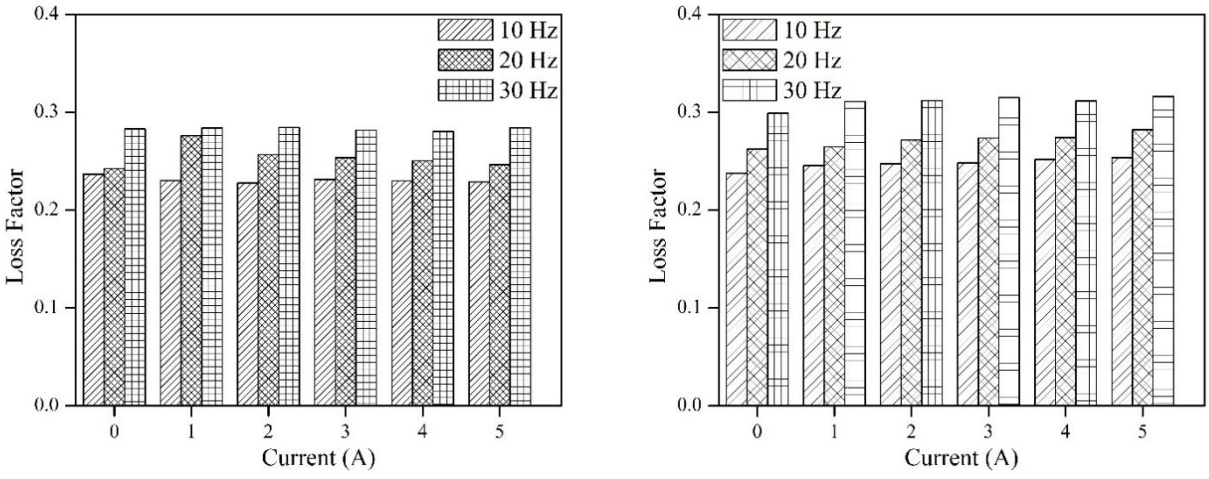

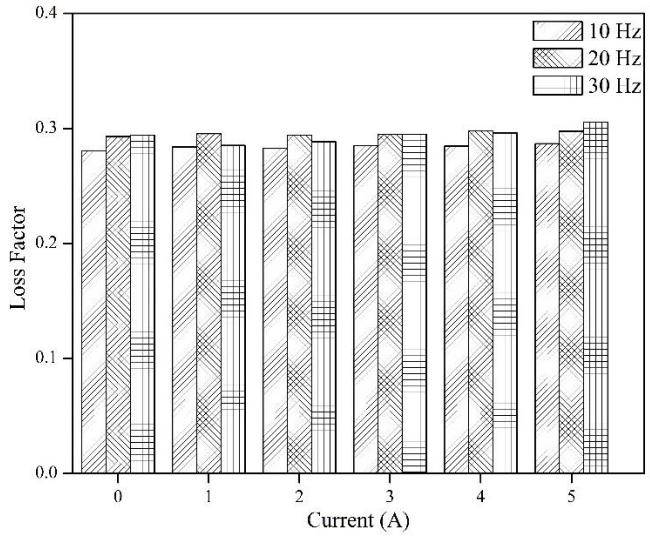

Figure 5-6: Displacement dependent variations in the loss factor for (a) 0.002 rad (b) 0.008 rad (c) 0.016 rad for varying magnetic fields

Magnetorheological elastomers belong to the category of the particle reinforced composites due to which the damping primarily depends on either the intrinsic damping, interface damping or the magneto-mechanical hysteresis damping (Ge et al. 2013)(Chandra et al. 1999). The intrinsic damping refers to the damping capacity predominantly observed between the rubber strands of the viscoelastic matrix of the MRE. It is caused by the friction existing between the polymer chains in the presence of the harmonic loading conditions (Yang et al. 2012). Though for an unfilled elastomer, the intrinsic damping behaves purely on the interactions between the rubber strands, for a filled elastomer, it depends on the volume fraction of the fillers. For a filled elastomer, the intrinsic damping capacity is given as,

$$D_C = (1 - \phi) D_m \tag{5.3}$$

Where D_m represents the damping ratio of the matrix and ϕ represents the volume fraction of the carbonyl iron particles

Interfacial damping in MRE is observed due to the relative interaction between the filler particles and the polymer chains. It is based on the relative friction existing between the polymer matrix chains and filler particles in the presence of an external shear. The interfacial damping is further categorized as ideal bonding, strongly bonding and weakly bonding. The ideal bonded condition does not dissipate energy, while the

strongly bonded elastomers dissipate energy based on the stress concentration on the surface of the CIP. Weakly bonded interfaces provide the majority of the damping based on the relative friction between the CIP and the bound rubber during harmonic loading. In the case of weak bonding at the interface, there exists an interfacial slip between the CIP and the bound rubber. This occurs when the magnitude of the applied shear is sufficient to overcome the frictional load. The interfacial damping capacity is given as,

$$D_s = \frac{4.5(1-\nu)}{\pi^2(2-\nu)}\phi + \left(\frac{3\pi}{2}Kf\xi - \frac{4.5(1-\nu)}{\pi^2(2-\nu)}\right) \times \sqrt[3]{1-\phi} \times \sqrt[3]{1-\epsilon_0} \times \phi \tag{5.4}$$

where ϕ represents the volume fraction of the CIP, *K* represents the coefficient which defines the number of interfaces which reach the critical strain value during the movement, f defines the friction movement between the CIP and the matrix, ξ represents the stress coefficient (i.e., the ratio of the applied stress to the developed normal stress), ν represents the Poisson's ratio of the matrix material and ϵ_0 represents the applied strain

Intrinsic and interfacial damping occurs in MRE due to its inherent characteristic features based on the viscoelastic behavior of the filled matrix. Apart from this, it is observed that damping exists in the MRE due to the magnetic field (also known as magneto-mechanical damping) induced from various sources. It is given as (Yang et al. 2012),

$$D_{mf} = \frac{4\alpha\epsilon}{3\pi E(B)} \tag{5.5}$$

Where ϵ represents the external strain, *E(B)* represents field-dependent elastic modulus and α represents the change of elastic modulus with the external strain

From the above, the total damping capacity is given as,

$$D = D_C + D_s + D_{mf} \tag{5.6}$$

It is observed that principal factors affecting the displacement induced variations in the damping are the interfacial (Ju et al. 2012b) and the field-induced

damping. Further, the effect of intrinsic damping is predominantly observed at lower volume fractions of the CIP(Yang et al. 2012), where the effect of the rubber strands is observed. With the increase in the volume fraction of the CIP, the damping offered by the matrix reduces. This is further substantiated from equation 7. Since the present study is carried out at a 27% volume fraction of the CIP, the intrinsic damping of the matrix is neglected. Hence the modified equation for the total damping capacity of the MRE is given as,

$$D = D_s + D_{mf} \tag{5.7}$$

As seen from Figure 5-6, the damping capabilities of the MRE increase with the increase in the input angular displacement. For a constant frequency of 10 Hz, the loss factor in the absence of the magnetic field at 0.002 rad is 0.236. With an increase in the input angular displacement to 0.016 rad, the loss factor increases to 0.28. With an increment of 18.64%, the increase in the displacement-dependent loss factor is explained by the interfacial damping existing between the CIP and the matrix.

It is seen that the filled elastomers dissipate more energy in comparison with their unfilled matrix counterparts due to the larger relative friction between CIP and the silicone matrix. During curing, the CIP blend with the silicone matrix and is bound by the tightly and the loosely bound layers (Figure 5-3 a). As seen earlier, due to the reduced loose bound rubber available on the surface of the CIP, there exists a relative shift between the CIP and the matrix during the harmonic loading of the MRE. Due to this, sliding friction exists between the two interfaces, which increases further with an increase in the input angular displacement. This is explained by the weak interfacial damping energy existing between the CIP and the matrix. For a unit volume of the MRE, the interfacial damping energy (E_s) due to the weakly bonded interfaces is given as (Chen et al. 2008b),

$$E_s = nfs \tag{5.8}$$

Where *n* denotes the number of carbonyl iron particles in a given unit volume of the MRE, *f* represents the sliding frictional force existing between the polymer chains and the iron particles, and *s* represents the relative displacement occurring between the surfaces of CIP and polymer chains.

From equation (12), it is observed that for a fixed number of iron particles, the interfacial damping energy is directly proportional to the sliding friction between the CIP and the matrix. With the increase in the angular displacement, the relative displacement (*s*) increases, which results in the increase in the interfacial damping on the bulk of the MRE.

Likewise, it is observed that the field-dependent variations in the loss factor are reduced in comparison with the angular displacement dependent variations. For a constant frequency of 10 Hz, the loss factor varies from 0.236 at 0T to 0.228 at 0.28T for an input angular displacement of 0.002 rad. These results indicate that the field-induced damping does not cause substantial variations in the overall damping of the MRE. It is also seen that the field-dependent variations in the loss factor are less predictable in comparison with the angular displacement dependent variations. Similar observations have been reported in the case of field-induced loss factor variations for lateral shear(Yang et al. 2012).

5.5. Summry

Apart from the applied field and the operating frequency, the dynamic properties of the MRE are effectively influenced by the input displacement. The present chapter investigates the effect of the angular displacement on the variations in the viscoelastic properties of the MRE. The experiments are carried out as per the ISO 10846-2 standard, as explained in Chapter 2. Further, the effect of the angular displacement is restricted to the Linear Viscoelastic Limit (LVE) by maintaining the operating range within 0.002 rad to 0.016 rad.

The Lissajous plots showcase the efficacy of the method in capturing the angular displacement-dependent variations in the dynamic torsional stiffness. The plots demonstrate a reduction in the stiffness values for increasing angular displacements. The variations are adequately explained by adapting the bound rubber theory. Also, the displacement dependent reduction in the stiffness is less in the presence of the magnetic field, which is explained by the existence of field-induced dipoles.

The variations in the angular displacement dependent damping capacity of the MRE are assessed in terms of the loss factor. It is concluded that the interfacial damping played a dominant role and the loss factor increased with the increase in the angular

displacement. The results further also suggest the reduced influence of the magnetic field on the variations in the loss factor.

While Chapter 4 discussed the variations in the field and frequency-dependent properties of the MRE isolator, the present chapter focused on the angular displacement dependent property variations in the properties MRE. This completes the characterization process of the MRE isolator. The proceeding chapter develops a parametric based viscoelastic model to comprehend the constitutive relations between the parameters.

6. Parametric Modelling of field, frequency and input angular displacement dependent viscoelastic behavior of MRE isolator

6.1. Introduction

The rheological properties of the MRE isolator are modeled using various approaches, of which the phenomenological technique replicates the actual behavior of the isolator in terms of the spring and the damper elements. It involves using standard linear spring, damper and fractional dashpot elements to explain the field-dependent, frequency-dependent and the displacement-dependent behavior of the MRE isolator.

What follows in the present chapter is the development of a fractional derivative-based Poynting Thomson model to represent the rheological properties of the MRE isolator. A total of six parameters are used in assessing its complex nature. The parameters are obtained by minimizing the effective error between the modeled values and the experimentally obtained data. The performance of the model is assessed based on its ability to predict the field-dependent and angular displacement dependent behavior over a frequency range from 10 Hz to 30 Hz. For the comparative assessment of the MRE, the field is varied from 0T to 0.28T, whereas the input displacement is changed from 0.002 rad to 0.016 rad.

6.2. Constituent Models

6.2.1. Kelvin Voight model

As described in chapter 2, the Kelvin-Voight model (Norouzi et al. 2015) represents the pre-yield behavior of the MRE using a spring and a damping element parallel to each other (Figure 6-1).

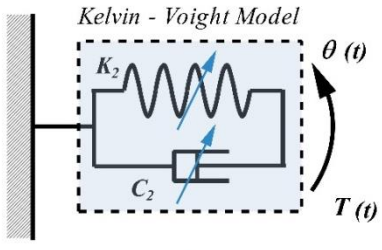

Figure 6-1: Kelvin-Voight Model

The parallel arrangement results in equal distribution of the input angular displacement to the individual elements. The total torque experienced by the elements is given as,

$$T_{KV}(t) = K_2\theta(t) + C_2\frac{d\theta}{dt} \quad (6.1)$$

Where, K_2 represents the torsional stiffness and C_2 represents the damping constant with θ being the input angular displacement. In terms of the complex stiffness, the equation is given as,

$$K_t^* = \frac{T_{KV}(t)}{\theta(t)} = K_2 + iC_2\omega \quad (6.2)$$

6.2.2. Poynting Thomson model

The Kelvin-Voight model effectively describes the complex stiffness variations of the viscoelastic materials. However, these variations in the rheological properties for varying displacement and frequencies over a broader range can be further adequately addressed by the addition of extra springs or dashpots in series to the constituent Kelvin-Voight model. This is termed as the Poynting Thomson model (Figure 6-2) (Poojary and Gangadharan 2018).

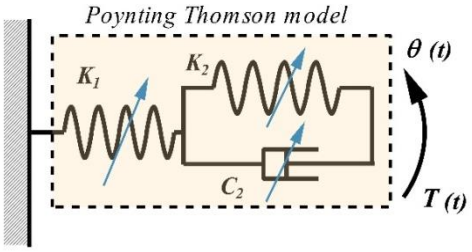

Figure 6-2: Poynting Thomson model

Due to their serial arrangements, the torque acting on the spring and the Kelvin-Voight element is the same. Hence, the total deformation of the Poynting Thomson element is the summation of the deformation of the spring element and the Kelvin-Voight element. The torque-angular displacement relation is given as,

$$(K_1 + K_2)T(t) + C_2\frac{dT(t)}{dt} = K_1K_2\theta(t) + K_1C_2\frac{d\theta(t)}{dt} \quad (6.3)$$

6.2.3. Fractional derivative

With the addition of multiple parameters, the complex nature of the MRE can be comprehended over a wide range of frequency and displacement. However, the inclusion of several parameters makes the model more complex due to its increased computational effort. Alternatively, the number of parameters is effectively reduced with the inclusion of fractional elements. The fractional element (Agirre-Olabide et al. 2018) consists of a spring-pot element (modified dashpot), which makes the constitutive relations to be time derivatives in the fractional form. This results in the smoother transitions of the damping characteristics of the MRE isolator. The torque component of the spring-pot element is given as,

$$T_{fd} = c\frac{d^{\alpha}\theta}{dt} \tag{6.4}$$

Where, T_{fd} represents the torque acting on the spring-pot & c and α are the fractional parameters. The term $\frac{d^{\alpha}\theta}{dt}$ denotes the time order derivative of the angular displacement of the order of α. The order determines the effective characteristic feature of the viscoelastic nature of the MRE, which lies in between a purely viscous material ($\alpha = 1$) and a purely elastic material ($\alpha = 0$).

6.3. Proposed Model for MRE

The rheological properties of the MRE subjected to torsional oscillations are studied using the constitutive models discussed in the previous section. To capture the effects of the angular displacement, magnetic field and frequency, a fractional derivative-based Poynting Thomson model is developed. It consists of a spring and a fractional element in parallel with the Poynting Thomson model. The three spring elements define the stiffness for the model and the two dashpots define the damping. The fractional element describes the effectiveness of the spring and the damping. The proposed model is shown in Figure 6-3.

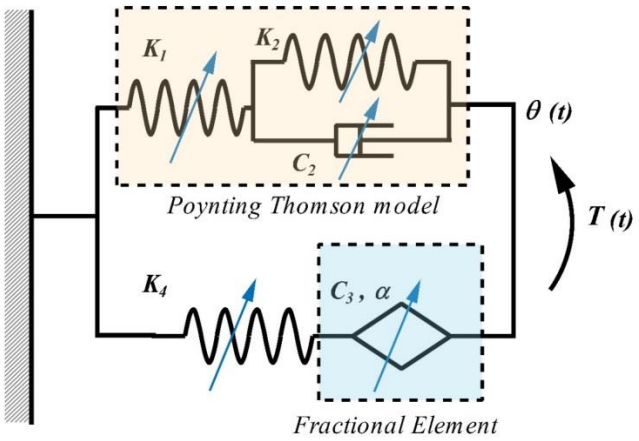

Figure 6-3: fractional Derivative based Poynting Thomson model

6.3.1. Fractional derivative-based Poynting Thomson model

The effectiveness of the fractional model is evaluated by comparing the experimentally obtained complex stiffness values with the modeled results. As given in section 6.2.1, the complex stiffness for the Kelvin-Voight model is given as,

$$K_{KV}{}^{*} = K_2 + iC_2\omega$$

Next, the Kelvin-Voight is in series with the spring K_1. Hence the equivalent complex stiffness ($K_{pt}{}^{*}$) is as follows,

$$\frac{1}{K_{pt}{}^{*}} = \frac{1}{K_1} + \frac{1}{K_{KV}{}^{*}}$$

$$\left(K_{pt}{}^{*}\right)^{-1} = \frac{K_1 + K_2 + iC_2\omega}{K_1(K_2 + iC_2\omega)}$$

$$K_{pt}{}^{*} = \frac{K_1(K_2 + iC_2\omega)}{K_1 + K_2 + iC_2\omega} \tag{6.5}$$

Taking the complex conjugate,

$$K_{pt}{}^{*} = \frac{K_1{}^2K_2 + K_1K_2{}^2 + K_1(C_2\omega)^2}{(K_1 + K_2)^2 + (C_2\omega)^2} + i\frac{K_1{}^2C_2\omega}{(K_1 + K_2)^2 + (C_2\omega)^2} \tag{6.6}$$

For a fractional model with a spring element in series, the torque acting on the system is given as (Poojary and Gangadharan 2018),

$$T_{fd}(t) + \frac{C_3}{K_4}\frac{d^\alpha}{dt^\alpha}\left(T_{fd}(t)\right) = C_3\frac{d^\alpha}{dt^\alpha}(\theta(t)) \tag{6.7}$$

Considering harmonic angular displacement $\theta = \theta_0 e^{i\omega t}$, the time domain equation is converted to the frequency domain signal using the relation,

$$T\left[\frac{d^\alpha}{dt^\alpha}(x(t))\right] = (i\omega)^\alpha x(t) \tag{6.8}$$

From the above, the relation between the angular displacement and the input torque in the frequency domain is obtained as,

$$T_{fd}(t) = \frac{K_4 C_3 (i\omega)^\alpha \theta(t)}{K_4 + C_3 (i\omega)^\alpha} \tag{6.9}$$

With $i^\alpha = \cos {\alpha\pi}/{2} + i \sin {\alpha\pi}/{2}$ and taking the conjugates, the equivalent complex stiffness is,

$$K_{fd}{}^* = \frac{K_4 C_3 \omega^\alpha \left(C_3 \omega^\alpha + K_4 \cos\frac{\alpha\pi}{2}\right)}{K_4{}^2 + (c_3\omega^\alpha)^2 + 2c_3\omega^\alpha K_4 \cos\frac{\alpha\pi}{2}} + i\frac{K_4{}^2 c_3 \omega^\alpha \sin\frac{\alpha\pi}{2}}{K_4{}^2 + (c_3\omega^\alpha)^2 + 2c_3\omega^\alpha K_4 \cos\frac{\alpha\pi}{2}} \tag{6.10}$$

Finally, with the Poynting-Thomson element and the Fractional derivative in parallel, the total complex stiffness of the system is given as,

$$K_t{}^* = \frac{K_1{}^2 K_2 + K_1 K_2{}^2 + K_1 (C_2\omega)^2}{(K_1 + K_2)^2 + (C_2\omega)^2} + \frac{K_4 C_3 \omega^\alpha \left(C_3 \omega^\alpha + K_4 \cos\frac{\alpha\pi}{2}\right)}{K_4{}^2 + (c_3\omega^\alpha)^2 + 2c_3\omega^\alpha K_4 \cos\frac{\alpha\pi}{2}} + i\left(\frac{K_1{}^2 C_2 \omega}{(K_1 + K_2)^2 + (C_2\omega)^2} + \frac{K_4{}^2 c_3 \omega^\alpha \sin\frac{\alpha\pi}{2}}{K_4{}^2 + (c_3\omega^\alpha)^2 + 2c_3\omega^\alpha K_4 \cos\frac{\alpha\pi}{2}}\right) \tag{6.11}$$

Where,

$$K_t{}' = \frac{K_1{}^2 K_2 + K_1 K_2{}^2 + K_1 (C_2\omega)^2}{(K_1 + K_2)^2 + (C_2\omega)^2} + \frac{K_4 C_3 \omega^\alpha \left(C_3 \omega^\alpha + K_4 \cos\frac{\alpha\pi}{2}\right)}{K_4{}^2 + (c_3\omega^\alpha)^2 + 2c_3\omega^\alpha K_4 \cos\frac{\alpha\pi}{2}}$$

And

$$K_t{}'' = \frac{K_1{}^2 C_2 \omega}{(K_1 + K_2)^2 + (C_2\omega)^2} + \frac{K_4{}^2 c_3 \omega^\alpha \sin\frac{\alpha\pi}{2}}{K_4{}^2 + (c_3\omega^\alpha)^2 + 2c_3\omega^\alpha K_4 \cos\frac{\alpha\pi}{2}}$$

6.4. Parameter Identification

The proposed model adheres to developing a mathematical relationship to predict the effect of the magnetic field, angular displacement and frequency on the rheological properties of the MRE. As stated earlier, the present study is carried out for five levels of input frequency, five levels of angular displacement & six levels of magnetic field corresponding to 150 sets of experimental data. For the estimation of the 6 parameters, i.e. $K_1, K_2, C_2, K_4, C_3, \alpha$, the model takes the angular displacement as the input, calculates the K' and K'' and gives the output torque $T(t)$. The parameters are measured as per the least square method, which minimizes the error between the experimentally obtained torque values and the model-predicted torque values. The error is defined by the objective function (A) given by the formula:

$$A = \sum_{i=1}^{j} [T_{mdi}(t) - T_{exi}(t)]^2 \tag{6.12}$$

Where:

- $T_{mdi}(t)$ is the model-predicted torque values
- $T_{exi}(t)$ is the experimentally obtained torque values
- j represents the experimental data for torsional loading in a single loop

The optimization of the parameters is carried out using the MATLAB optimization toolbox.

6.4.1. Parameters of Fractional Poynting Thomson Model:

The parameters of the fractional derivative model obtained by minimizing the objective function, as defined by equation (6.1), are tabulated in Table 6.1-Table 6.5. From the variations observed, the results reflect the sensitivity of the obtained parameters to the applied field, frequency, and angular displacement.

Table 6.1: Optimized parameters for 0.002 rad

0.002 rad		0	0.06	0.12	0.18	0.21	0.28
K_1	10	19.800	19.862	19.949	20.059	20.127	20.179
	15	19.842	19.917	19.982	20.069	20.172	20.270
	20	19.942	20.022	20.124	20.242	20.368	20.481
	25	20.022	20.088	20.149	20.261	20.369	20.499
	30	20.045	20.102	20.166	20.281	20.401	20.499
K_2	10	6.847	7.012	7.242	7.382	7.481	7.560
	15	6.902	7.062	7.262	7.402	7.521	7.629
	20	6.942	7.049	7.166	7.286	7.409	7.499
	25	6.964	7.072	7.240	7.406	7.564	7.606
	30	6.969	7.061	7.261	7.414	7.549	7.604
K_3	10	2.562	2.608	2.641	2.682	2.722	2.769
	15	2.592	2.639	2.688	2.702	2.741	2.782
	20	2.601	2.642	2.689	2.720	2.768	2.799
	25	2.621	2.660	2.700	2.721	2.771	2.801
	30	2.641	2.681	2.721	2.742	2.782	2.811
C_2	10	0.0280	0.0284	0.0289	0.0292	0.0296	0.0302
	15	0.0182	0.0184	0.0187	0.0191	0.0192	0.0196
	20	0.0124	0.0130	0.0135	0.0144	0.0152	0.0159
	25	0.0106	0.0108	0.0112	0.0114	0.0119	0.0124
	30	0.0092	0.0094	0.0096	0.0097	0.0098	0.0102
C_3	10	0.0123	0.0117	0.0112	0.0109	0.0104	0.0099
	15	0.0112	0.0110	0.0105	0.0100	0.0092	0.0092
	20	0.0108	0.0102	0.0099	0.0092	0.0086	0.0082
	25	0.0101	0.0100	0.0097	0.0088	0.0081	0.0077
	30	0.0092	0.0089	0.0086	0.0082	0.0074	0.0068
α	10	0.7869	0.7989	0.8087	0.8197	0.8267	0.8389
	15	0.7999	0.8100	0.8190	0.8272	0.8370	0.8262
	20	0.8099	0.8169	0.8280	0.8369	0.8460	0.8569
	25	0.8169	0.8269	0.8341	0.8421	0.8509	0.8599
	30	0.8283	0.8382	0.8471	0.8561	0.8642	0.8741

Table 6.2: Optimized parameters for 0.004 rad

0.004 rad		0	0.06	0.12	0.18	0.21	0.28
K_1	10	19.568	19.689	19.803	19.903	20.003	20.103
	15	19.602	19.722	19.842	19.962	20.082	20.122
	20	19.682	19.784	19.900	20.020	20.140	20.184
	25	19.762	19.822	19.962	20.062	20.182	20.292
	30	19.802	19.867	19.987	20.097	20.217	20.327
K_2	10	6.667	6.847	7.047	7.202	7.302	7.392
	15	6.747	6.947	7.148	7.308	7.420	7.520
	20	6.809	7.029	7.192	7.388	7.492	7.612
	25	6.874	7.049	7.222	7.402	7.522	7.692
	30	6.924	7.069	7.242	7.421	7.541	7.711
K_3	10	2.583	2.623	2.663	2.703	2.743	2.787
	15	2.603	2.643	2.683	2.723	2.763	2.803
	20	2.627	2.669	2.707	2.744	2.784	2.801
	25	2.647	2.683	2.723	2.763	2.808	2.848
	30	2.669	2.706	2.742	2.782	2.824	2.861
C_2	10	0.028	0.029	0.029	0.030	0.031	0.032
	15	0.019	0.020	0.021	0.021	0.022	0.022
	20	0.012	0.013	0.014	0.014	0.015	0.015
	25	0.010	0.011	0.011	0.012	0.012	0.012
	30	0.010	0.010	0.010	0.010	0.010	0.010
C_3	10	0.012	0.012	0.012	0.011	0.011	0.011
	15	0.011	0.011	0.010	0.010	0.009	0.008
	20	0.011	0.010	0.010	0.009	0.008	0.008
	25	0.010	0.010	0.009	0.008	0.008	0.007
	30	0.010	0.009	0.009	0.008	0.008	0.007
α	10	0.785	0.796	0.803	0.813	0.822	0.832
	15	0.796	0.806	0.816	0.824	0.836	0.848
	20	0.806	0.814	0.826	0.834	0.842	0.852
	25	0.812	0.818	0.828	0.836	0.846	0.854
	30	0.827	0.836	0.842	0.851	0.859	0.868

Table 6.3: Optimized parameters for 0.008 rad

0.008 rad		0	0.06	0.12	0.18	0.21	0.28
	10	19.425	19.545	19.665	19.785	19.945	20.069
	15	19.470	19.526	19.696	19.802	19.962	20.082
K_1	20	19.525	19.583	19.722	19.828	19.986	20.126
	25	19.582	19.684	19.819	19.942	20.025	20.143
	30	19.642	19.764	19.883	20.022	20.102	20.162
	10	6.544	6.704	6.864	6.984	7.098	7.201
	15	6.609	6.726	6.926	7.085	7.144	7.225
K_2	20	6.622	6.745	6.964	7.102	7.168	7.247
	25	6.669	6.747	6.969	7.118	7.169	7.262
	30	6.724	6.806	6.981	7.122	7.174	7.282
	10	2.604	2.644	2.682	2.728	2.770	2.803
	15	2.626	2.662	2.689	2.726	2.789	2.801
K_3	20	2.649	2.689	2.729	2.761	2.782	2.824
	25	2.668	2.702	2.742	2.784	2.824	2.866
	30	2.702	2.762	2.807	2.842	2.880	2.912
	10	0.0284	0.0290	0.0292	0.0302	0.0314	0.0320
	15	0.0189	0.0196	0.0206	0.0214	0.0220	0.0230
C_2	20	0.0137	0.0140	0.0146	0.0152	0.0159	0.0168
	25	0.0102	0.0113	0.0117	0.0124	0.0130	0.0138
	30	0.0094	0.0101	0.0110	0.0114	0.0120	0.0124
	10	0.0126	0.0122	0.0119	0.0116	0.0114	0.0112
	15	0.0114	0.0109	0.0104	0.0099	0.0091	0.0086
C_3	20	0.0109	0.0108	0.0090	0.0086	0.0081	0.0079
	25	0.0102	0.0094	0.00892	0.0082	0.0078	0.0076
	30	0.0096	0.0092	0.0089	0.0078	0.0072	0.0068
	10	0.784	0.796	0.802	0.816	0.827	0.836
	15	0.791	0.801	0.817	0.829	0.836	0.844
α	20	0.804	0.819	0.826	0.834	0.841	0.849
	25	0.816	0.827	0.839	0.846	0.852	0.858
	30	0.824	0.829	0.840	0.842	0.856	0.862

Table 6.4: Optimized parameters for 0.012 rad

0.012 rad		0	0.06	0.12	0.18	0.21	0.28
K_1	10	19.309	19.419	19.524	19.644	19.749	19.842
	15	19.364	19.464	19.584	19.702	19.824	19.964
	20	19.409	19.521	19.661	19.809	19.949	20.069
	25	19.482	19.642	19.802	19.902	20.002	20.082
	30	19.568	19.750	19.861	19.980	20.081	20.129
K_2	10	6.416	6.570	6.707	6.822	6.942	6.992
	15	6.424	6.597	6.763	6.925	7.013	7.122
	20	6.431	6.591	6.769	6.882	7.022	7.142
	25	6.481	6.649	6.838	6.982	7.082	7.189
	30	6.561	6.720	6.860	6.982	7.162	7.269
K_3	10	2.622	2.669	2.708	2.742	2.761	2.791
	15	2.672	2.712	2.762	2.830	2.862	2.904
	20	2.721	2.761	2.811	2.861	2.911	2.961
	25	2.782	2.849	2.897	2.940	2.964	2.994
	30	2.844	2.886	2.941	2.980	3.024	3.041
C_2	10	0.0290	0.0295	0.0310	0.0317	0.0325	0.0327
	15	0.0173	0.0192	0.0202	0.0214	0.0224	0.0232
	20	0.0132	0.0142	0.0153	0.0164	0.0169	0.0174
	25	0.0160	0.0116	0.0119	0.0124	0.0130	0.0137
	30	0.0090	0.0091	0.0092	0.0094	0.0096	0.0098
C_3	10	0.0128	0.0124	0.0120	0.0117	0.0114	0.0112
	15	0.0116	0.0113	0.0107	0.0102	0.0092	0.0087
	20	0.0114	0.0109	0.0104	0.0098	0.0087	0.0081
	25	0.0108	0.0096	0.0090	0.0086	0.0082	0.0074
	30	0.0091	0.0084	0.0087	0.0079	0.0074	0.0070
α	10	0.784	0.794	0.800	0.809	0.818	0.827
	15	0.791	0.799	0.809	0.816	0.824	0.832
	20	0.799	0.809	0.818	0.827	0/837	0.847
	25	0.802	0.812	0.826	0.838	0.844	0.852
	30	0.814	0.824	0.834	0.842	0.850	0.860

Table 6.5. Optimized parameters for 0.016 rad

0.016 rad		0	0.06	0.12	0.18	0.21	0.28
	10	19.160	19.279	19.389	19.499	19.609	19.704
	15	19.269	19.427	19.589	19.729	19.862	19.982
K_1	20	19.324	19.449	19.599	19.742	19.882	19.996
	25	19.397	19.519	19.639	19.752	19.892	20.024
	30	19.488	19.622	19.782	19.947	20.127	20.194
	10	6.082	6.202	6.325	6.425	6.542	6.662
	15	6.092	6.271	6.462	6.582	6.689	6.784
K_2	20	6.099	6.302	6.494	6.643	6.769	6.862
	25	6.142	6.341	6.527	6.682	6.780	6.900
	30	6.239	6.460	6.679	6.840	7.006	7.146
	10	2.644	2.682	2.724	2.764	2.804	2.842
	15	2.689	2.724	2.780	2.824	2.869	2.901
K_3	20	2.784	2.822	2.840	2.869	2.902	2.942
	25	2.821	2.864	2.902	2.947	2.981	3.024
	30	2.861	2.919	2.969	3.022	3.062	3.070
	10	0.0284	0.0296	0.0322	0.0344	0.0360	0.0368
	15	0.0189	0.0198	0.0206	0.0209	0.0212	0.0217
C_2	20	0.0136	0.0144	0.0150	0.0156	0.0160	0.0167
	25	0.0110	0.0117	0.0124	0.0126	0.0129	0.0134
	30	0.0094	0.0100	0.0109	0.0111	0.0117	0.0119
	10	0.0138	0.0132	0.0126	0.0118	0.0112	0.0110
	15	0.0124	0.0112	0.0106	0.0102	0.0098	0.0093
C_3	20	0.0114	0.0108	0.0107	0.0099	0.0092	0.0086
	25	0.0104	0.0092	0.0089	0.0084	0.0079	0.0070
	30	0.0090	0.0089	0.0082	0.0071	0.0062	0.0053
	10	0.779	0.785	0.792	0.802	0.810	0.817
	15	0.783	0.792	0.801	0.809	0.816	0.825
α	20	0.790	0.796	0.806	0.818	0.821	0.829
	25	0.797	0.808	0.817	0.827	0.834	0.846
	30	0.807	0.817	0.827	0.834	0.842	0.850

6.5. Comparison between the experimental and Modelled data

6.5.1. Magnetic field and frequency

Figure 6-4 - Figure 6-8 shows the comparison between the modeled and the experimental field-dependent torque v/s angular displacement hysteresis curves for the measured frequencies at different input angular displacements. From the graphs, it is evident that the prediction using the developed model is in accordance with the experimentally obtained data. The field stiffening effect of the MRE is visible from the increasing slope of the modeled graphs. At the same time, the variations in the area of the torque-angular displacement curves vary, highlighting the influence of the damping of the MRE.

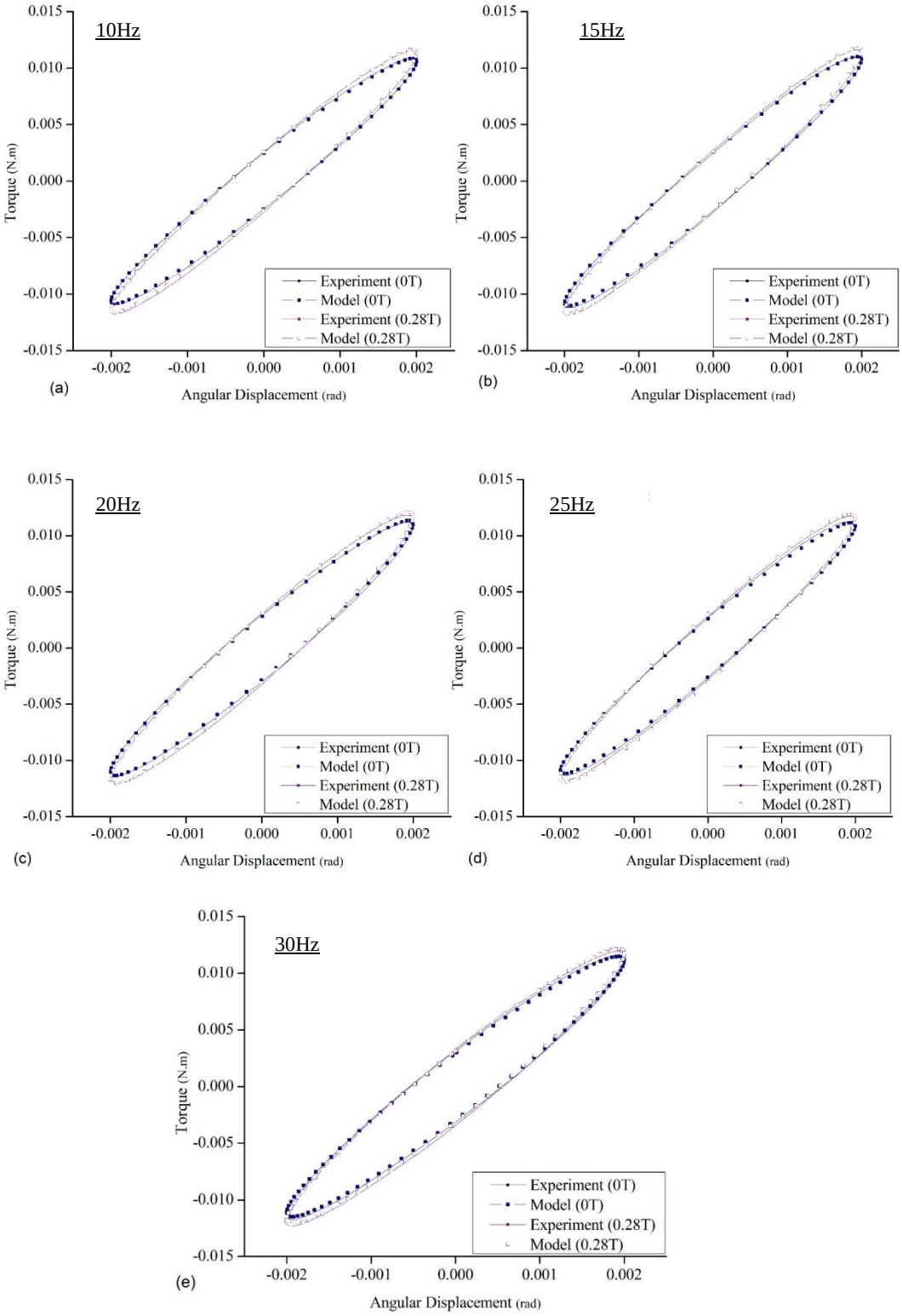

Figure 6-4: Modelled vs Experimental torque vs Angular displacement Hysteresis curves for 0.004 rad (a) 10 Hz (b) 15 Hz (c) 20 Hz (d) 25 Hz (e) 30 Hz

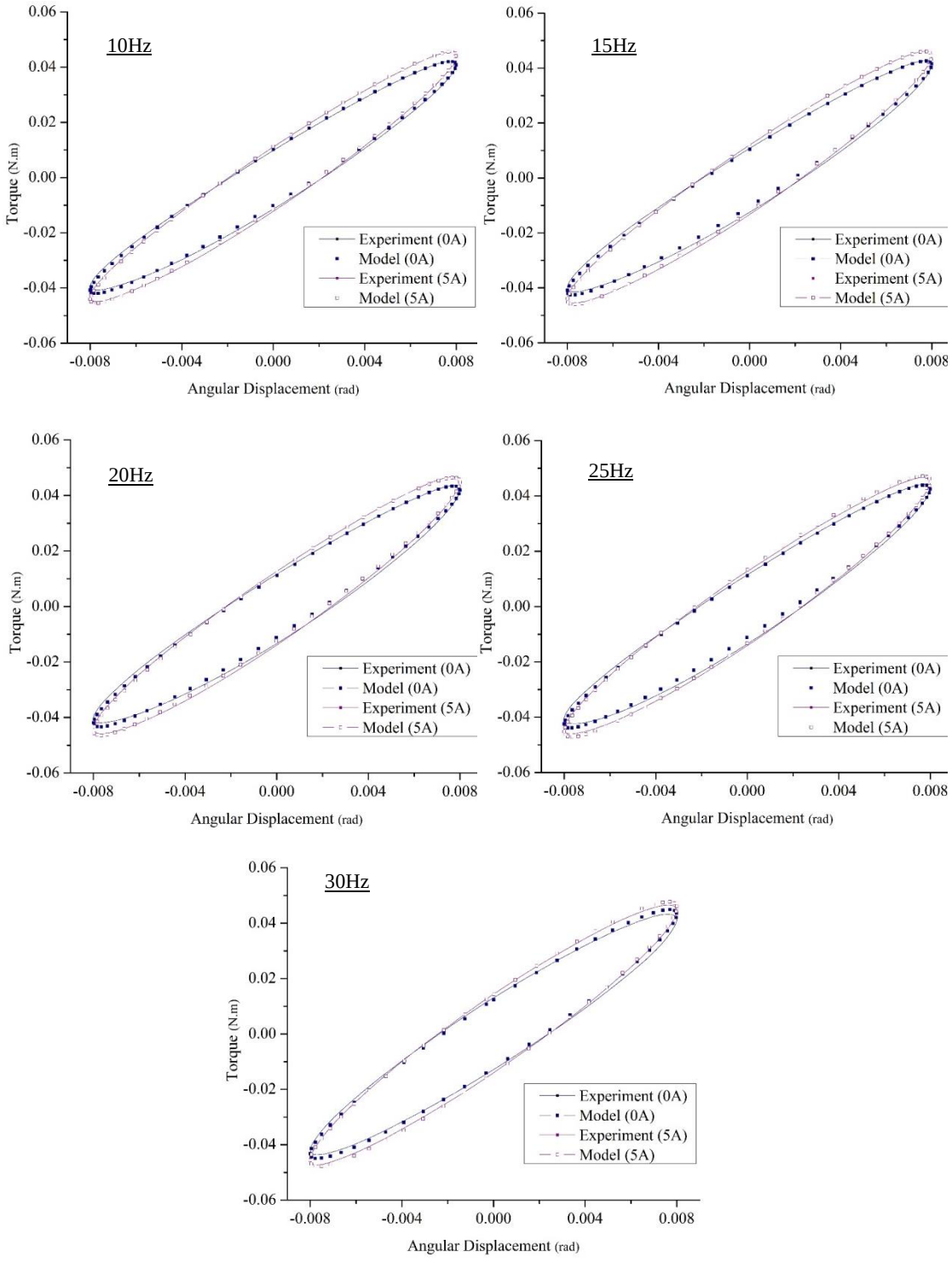

Figure 6-5: Modelled vs Experimental torque vs Angular displacement Hysteresis curves for 0.004 rad (a) 10 Hz (b) 15 Hz (c) 20 Hz (d) 25 Hz (e) 30 Hz

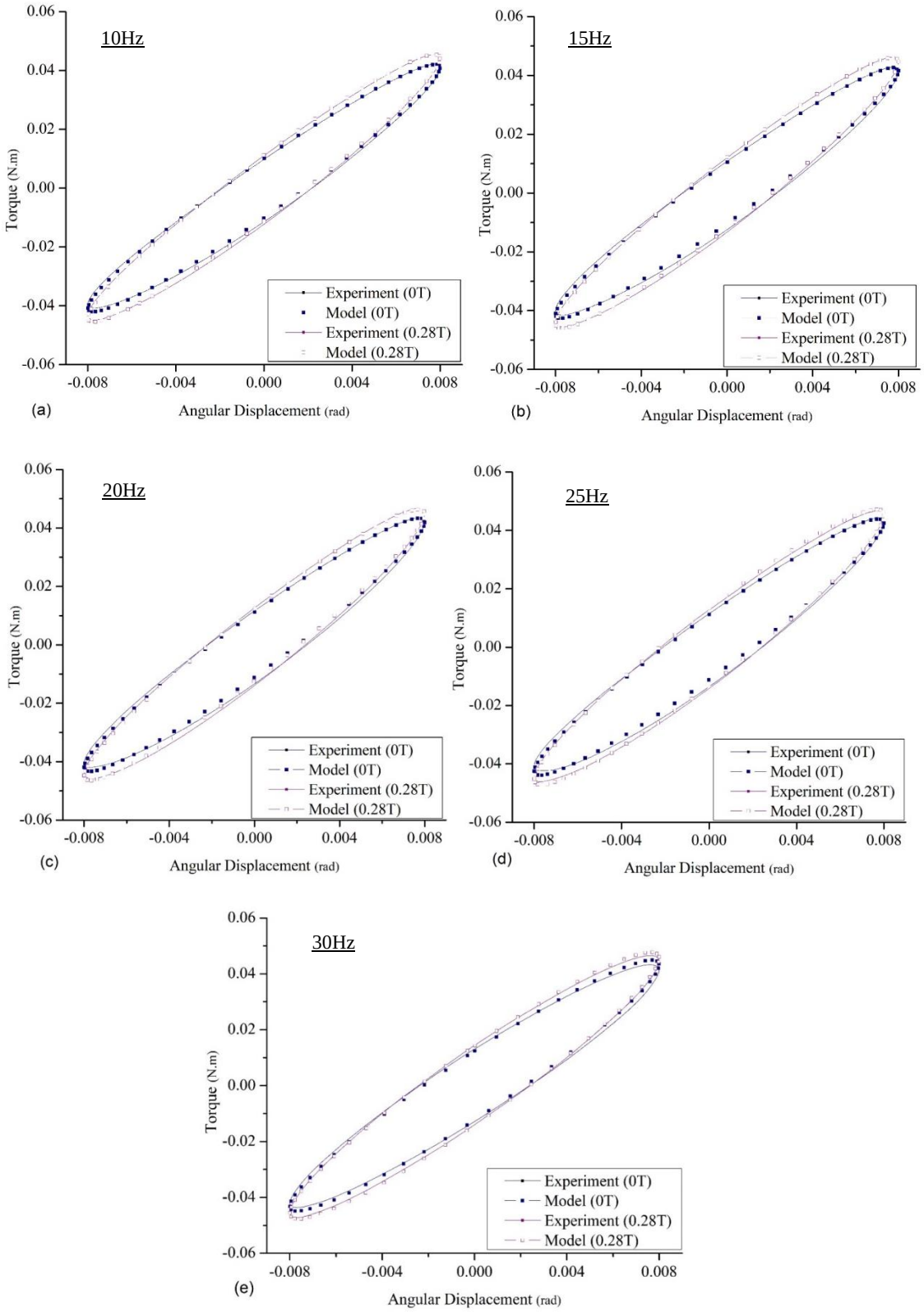

Figure 6-6: Modelled vs. Experimental torque vs. Angular displacement Hysteresis curves for 0.008 rad (a) 10 Hz (b) 15 Hz (c) 20 Hz (d) 25 Hz (e) 30 Hz

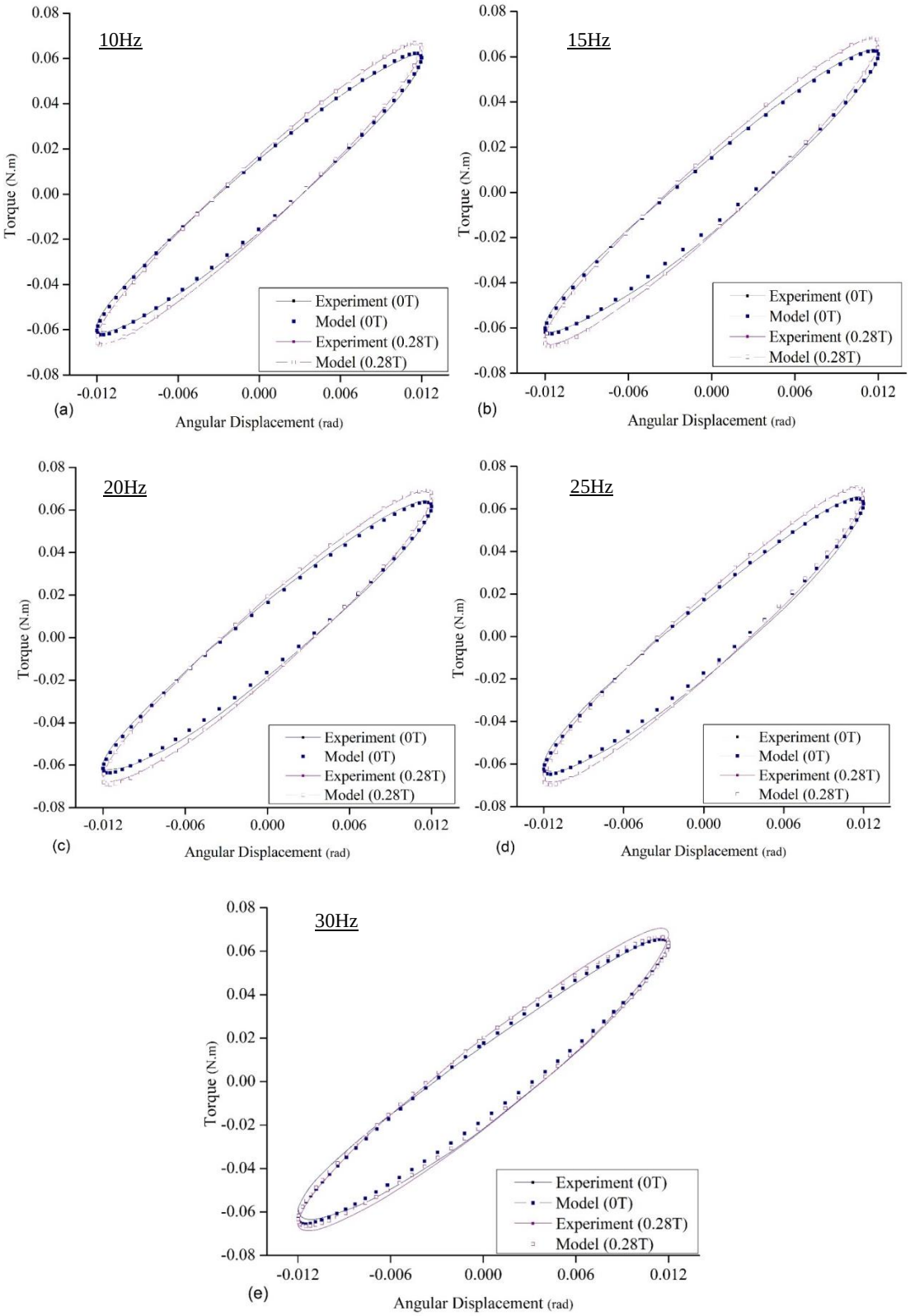

Figure 6-7: Modelled vs Experimental torque vs Angular displacement Hysteresis curves for 0.012 rad (a) 10 Hz (b) 15 Hz (c) 20 Hz (d) 25 Hz (e) 30 Hz

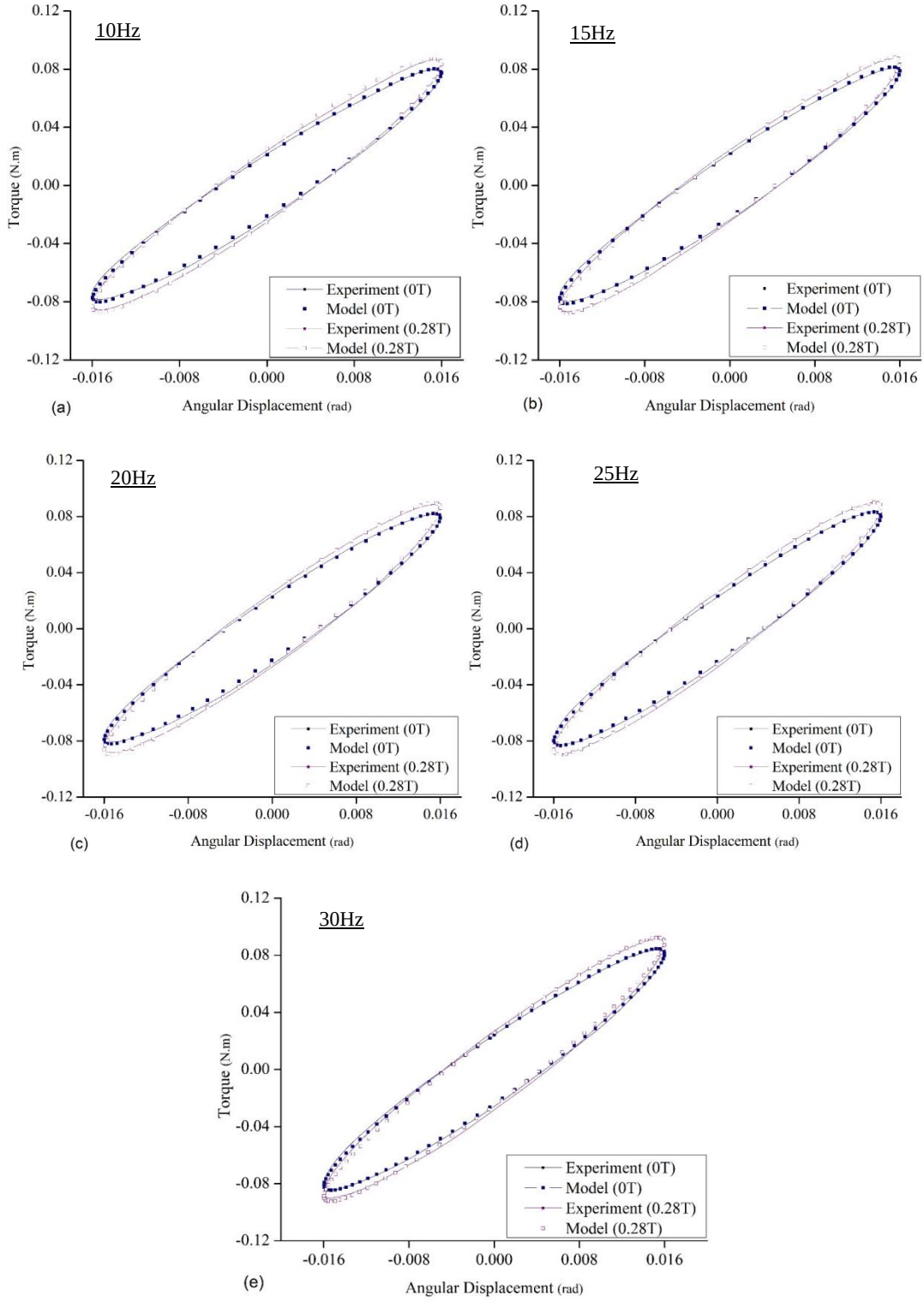

Figure 6-8: Modelled vs Experimental torque vs Angular displacement Hysteresis curves for 0.016 rad (a) 10 Hz (b) 15 Hz (c) 20 Hz (d) 25 Hz (e) 30 Hz

6.5.1. Angular displacement

From the obtained parameters, the dependency of the angular displacement on the MRE isolator is predicted, and the corresponding field-dependent torque-displacement curves are plotted for varying frequencies. Figure 6-9 - Figure 6-13 highlights the comparisons between the predicted and the experimental hysteresis curves. The nature of the slope ascertains the displacement dependent reduction of the complex stiffness of the MRE isolator. The result demonstrates that the established model effectively predicts the behavior of the bound rubber on the MRE isolator in the absence and the presence of the magnetic field. Additionally, the displacement dependent variations in the dissipated energy are also clearly observed from the increase in the area of the hysteresis curves.

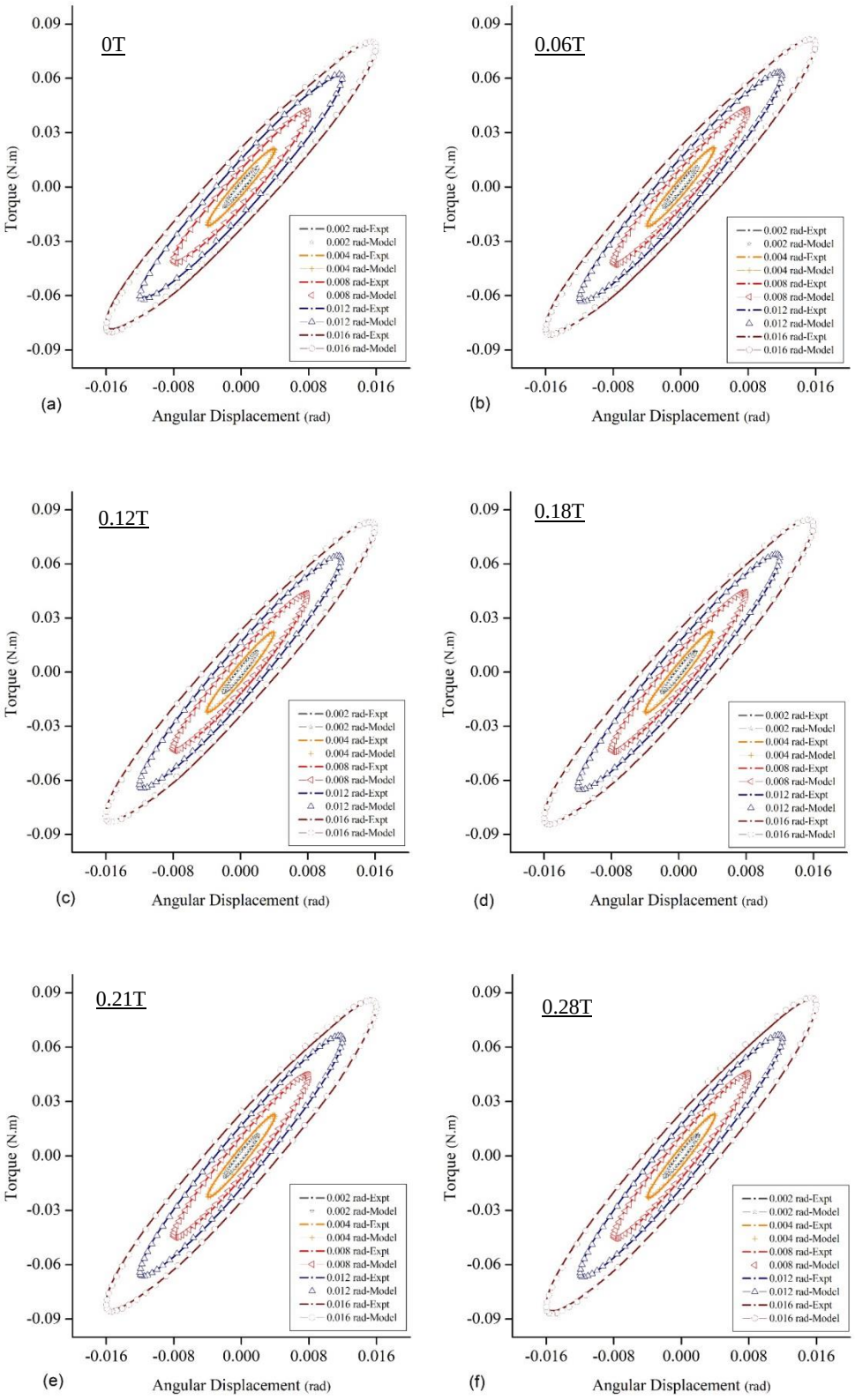

Figure 6-9: Hysteresis curves for 10 Hz (a) 0T (b) 0.06T (c) 0.12T (d) 0.18T (e) 0.21T (f) 0.28T

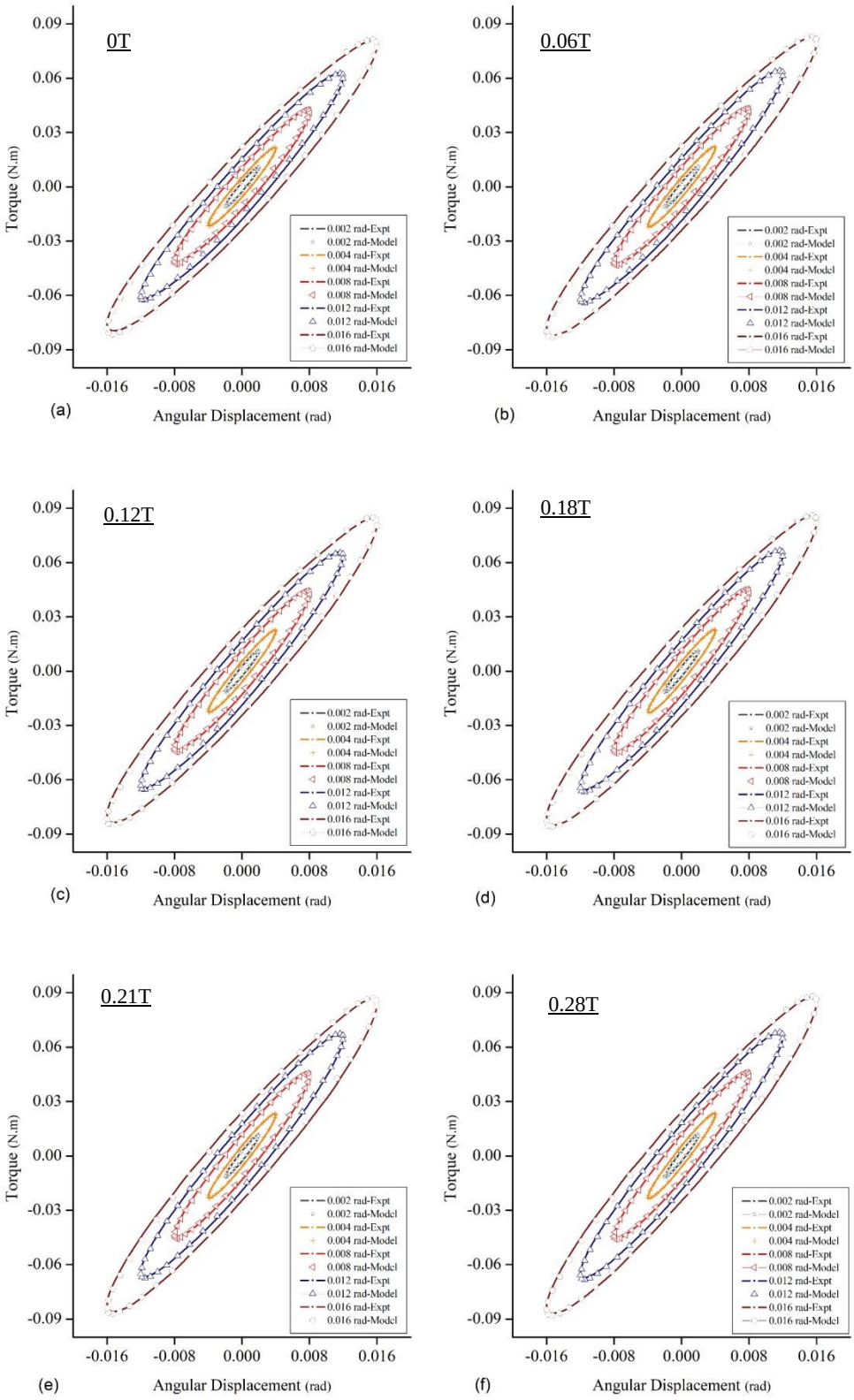

Figure 6-10: Hysteresis curves for 15 Hz (a) 0T (b) 0.06T (c) 0.12T (d) 0.18T (e) 0.21T (f) 0.28T

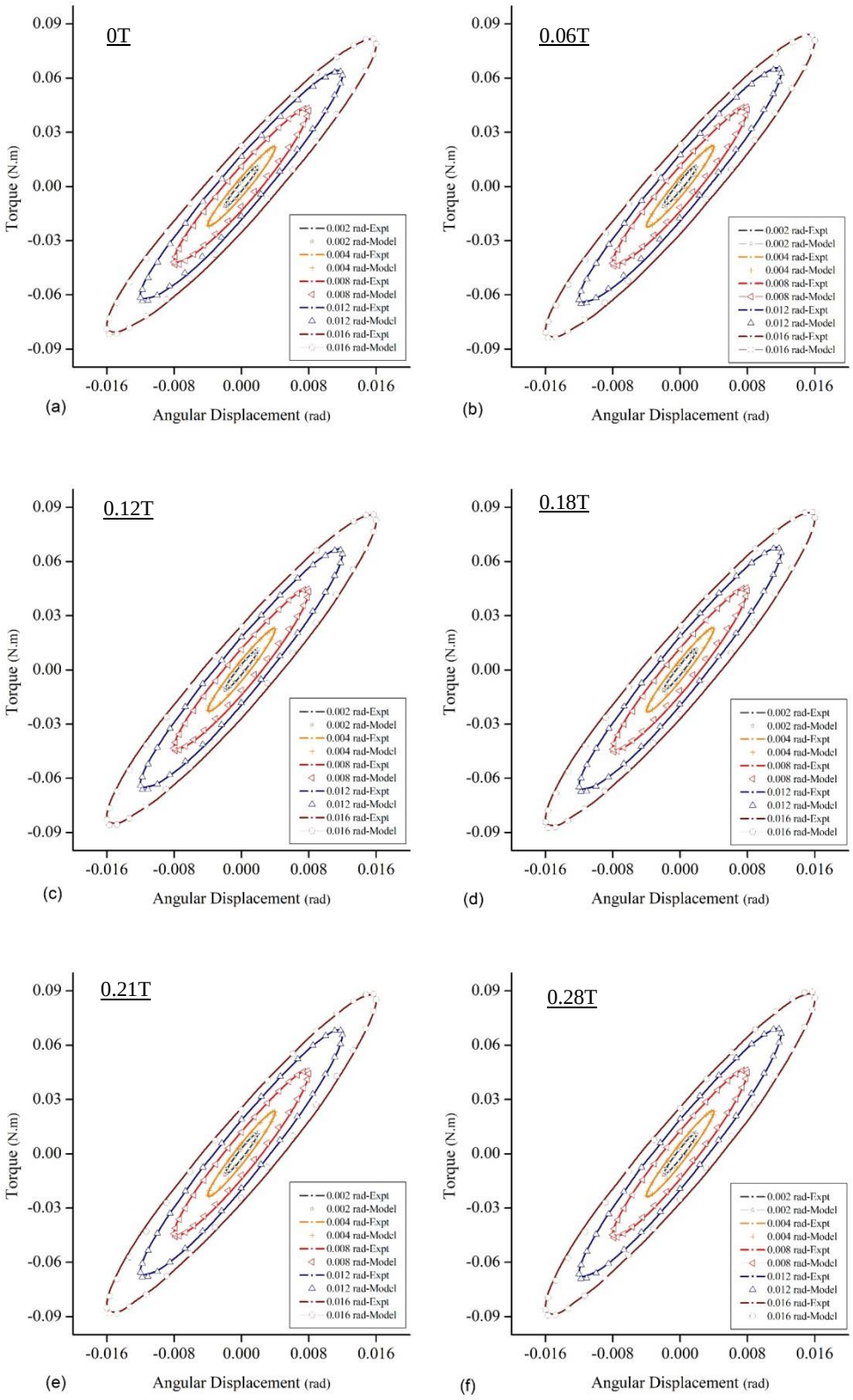

Figure 6-11: Hysteresis curves for 20 Hz (a) 0T (b) 0.06T (c) 0.12T (d) 0.18T (e) 0.21T (f) 0.28T

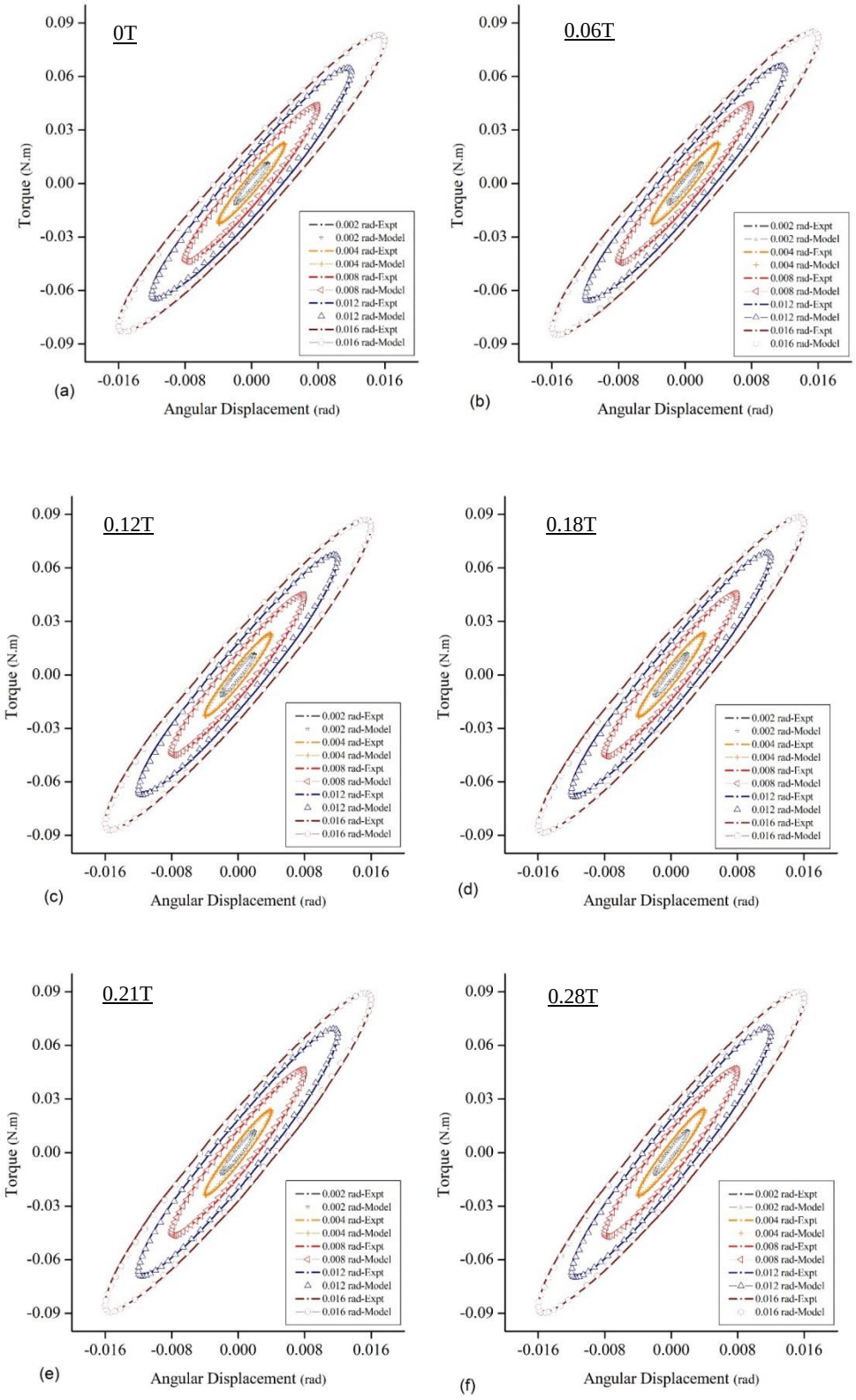

Figure 6-12: Hysteresis curves for 25 Hz (a) 0T (b) 0.06T (c) 0.12T (d) 0.18T (e) 0.21T (f) 0.28T

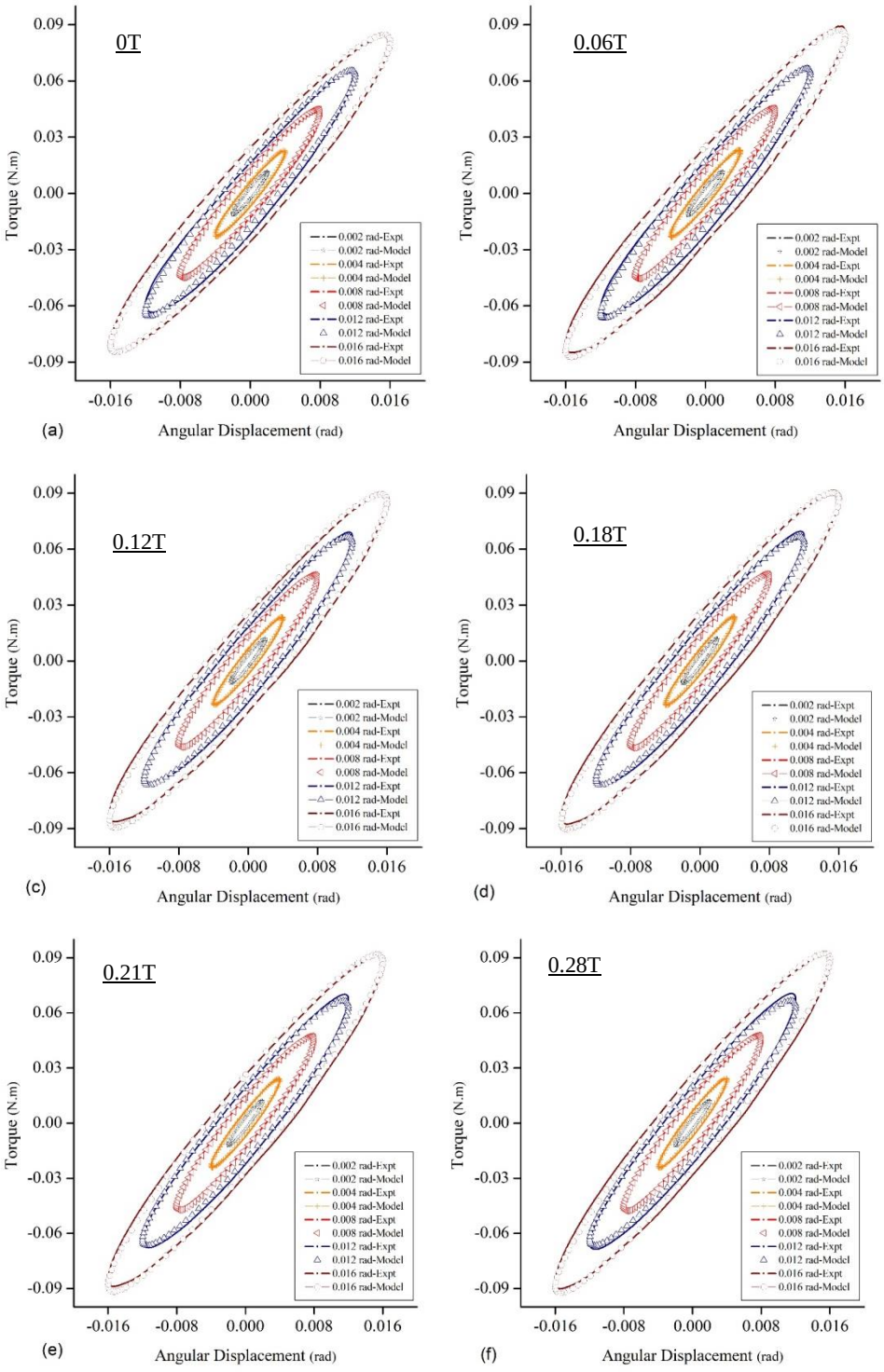

Figure 6-13: Hysteresis curves for 30 Hz (a) 0T (b) 0.06T (c) 0.12T (d) 0.18T (e) 0.21T (f) 0.28T

6.6. Comparison between modeled and experimental rheological properties

From equations (6.11), the complex stiffness, along with its real part and the imaginary part is obtained. Figure 6-14 to Figure 6-18 shows the comparison between the experimental and modeled values of the K', K'', K^* for different input angular displacements. For comparisons, three frequency components (10Hz, 20Hz, 30Hz) are considered. It is understood that the measured stiffness values (K' *and* K^*) increase with an increase in the magnetic field. For example, for an angular displacement of 0.012 rad, the stiffness, K'_t increases from 5.026 N.m rad^{-1} at 0T to 5.381 N.m rad^{-1} at 0.28T for the operating frequency of 10 Hz. Similarly, the field-dependent complex stiffness, K^*, increases from 5.192 N.m rad^{-1} to 5.566 N.m rad^{-1}. The results indicate that the stiffness values obtained from the model are in good agreement with the experimentally obtained values. The modeled data shows an accuracy of more than 96% and 95 % for the predicted values of K' *and* K^* respectively. The same is true for all the tested frequencies at all input angular displacements. However, it is observed that the predicted K'' values are not as accurate as the stiffness values and deviate with accuracy as low as 90.7%. Besides, it is observed that the deviations of the K'' from the experimental results are more at higher operating frequencies. These deviations are ascribed to the K''variations obtained experimentally. As evident from the experimental values, the K''values for the MRE under torsional loads does not follow a prescribed trend in its field-dependent variations. This results in the increased error between the predicted and the experimental K''values

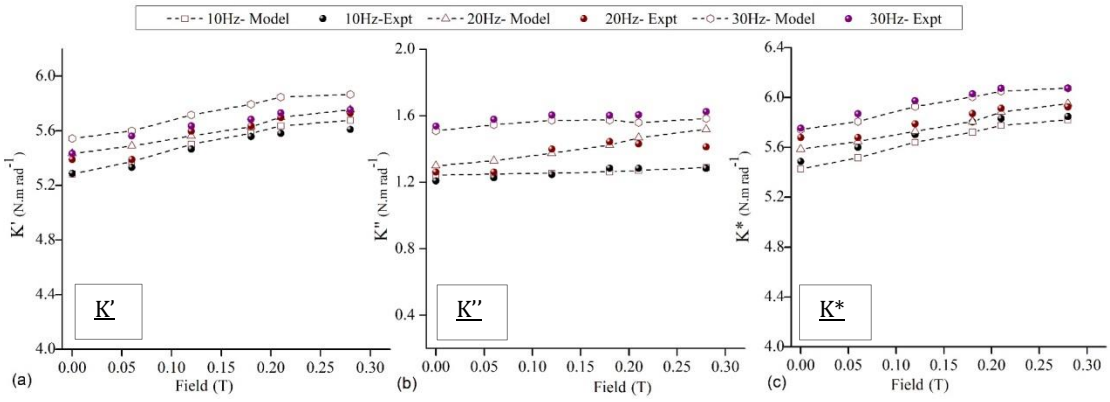

Figure 6-14: Experimental v/s Predicted values for 0.002 rad (a) K' (b) K'' (c) K^*

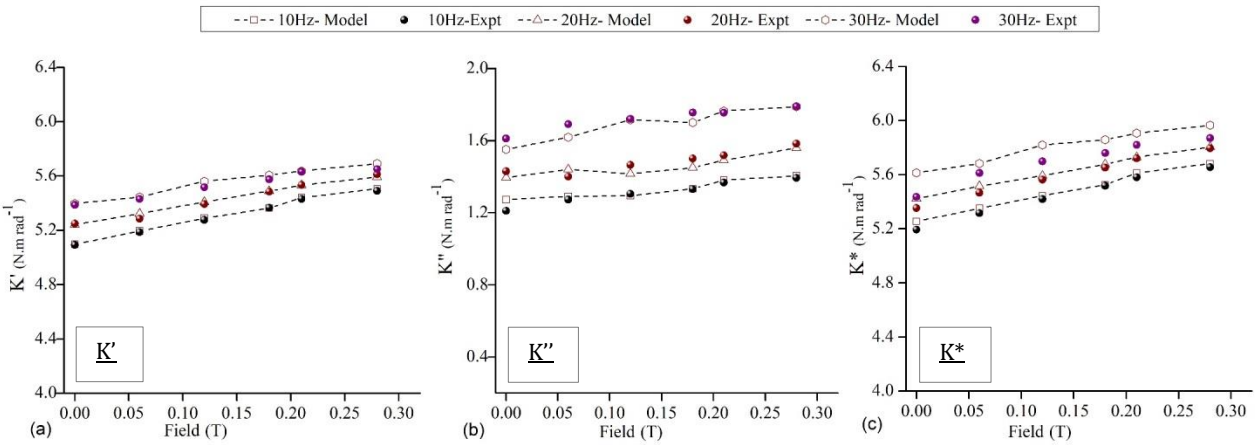

Figure 6-15: Experimental v/s Predicted values for 0.004 rad (a) *K′* (b) *K″* (c) *K**

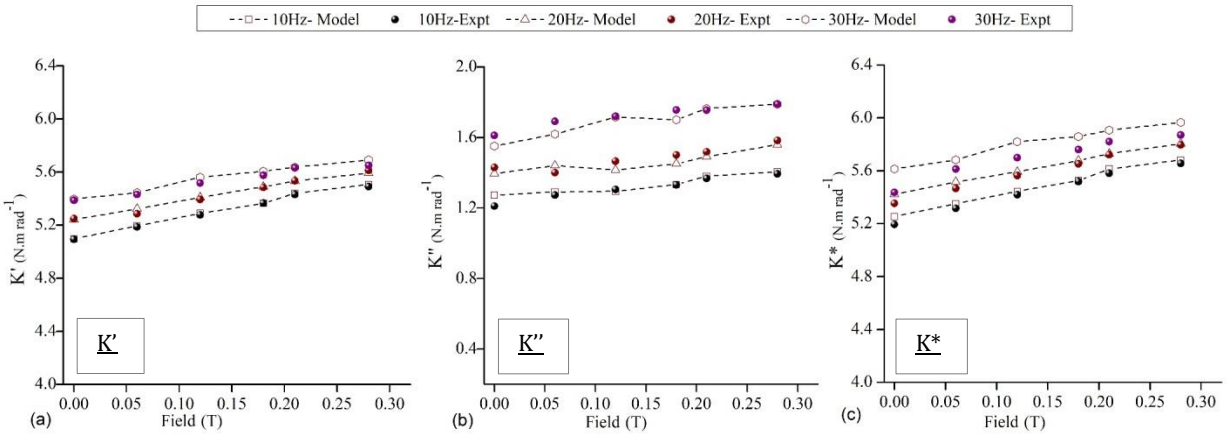

Figure 6-16: Experimental v/s Predicted values for 0.008 rad (a) *K′* (b) *K″* (c) *K**

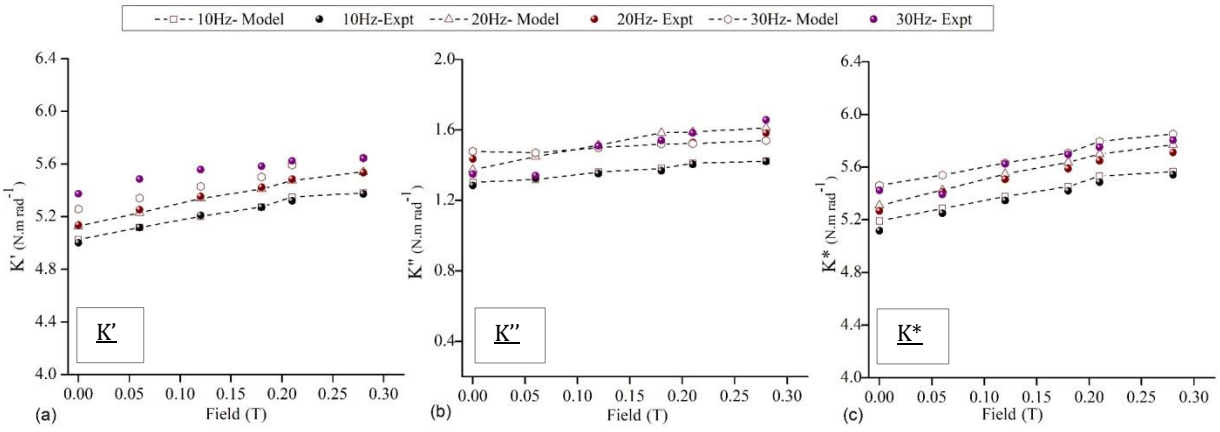

Figure 6-17: Experimental v/s Predicted values for 0.012 rad (a) *K′* (b) *K″* (c) *K**

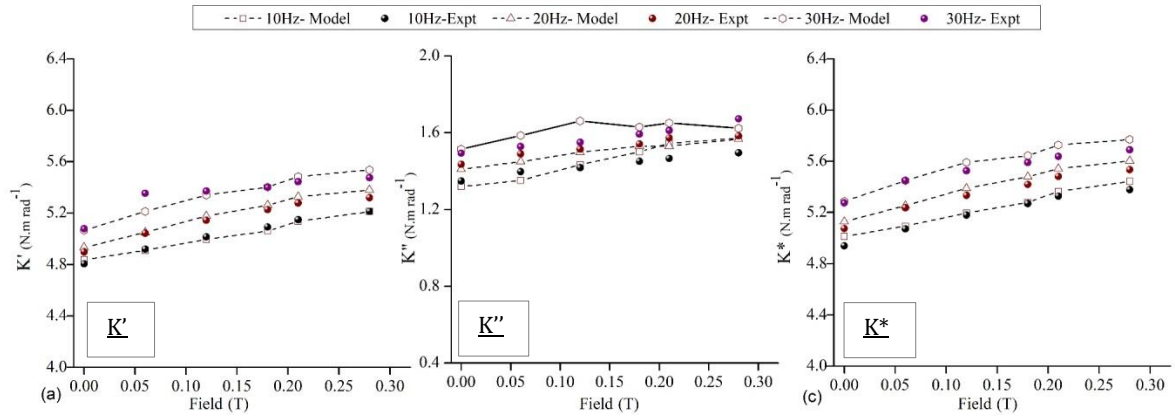

Figure 6-18: Experimental v/s Predicted values for 0.016 rad (a) *K'* (b) *K''* (c) *K**

6.6.1. Error Calculations

The percentage error in estimating the stiffness values (*K', K'', K**) is calculated and is presented in Figure 6-19- Figure 6-23. The data elucidates that the fractional model accurately predicts the experimental results with minimal error. For example, for a displacement of 0.002 rad, the maximum percentage error is within 2.2% for *K'* and *K**. However, for the *K''* term, the accuracy reduces with an increase in the error to 7.2%. A similar trend is observed for the rest of the data. From the error analysis, it is understood that the damping characteristics of the MRE isolator vary with the input parameters.

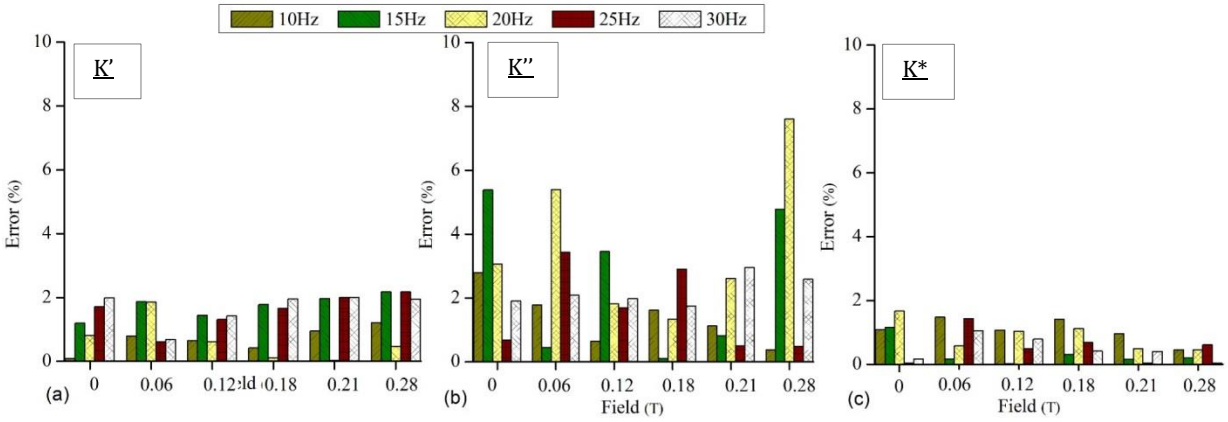

Figure 6-19: Percentage error between experimental and Predicted values for 0.002 rad (a) *K'* (b) *K''* (c) *K**

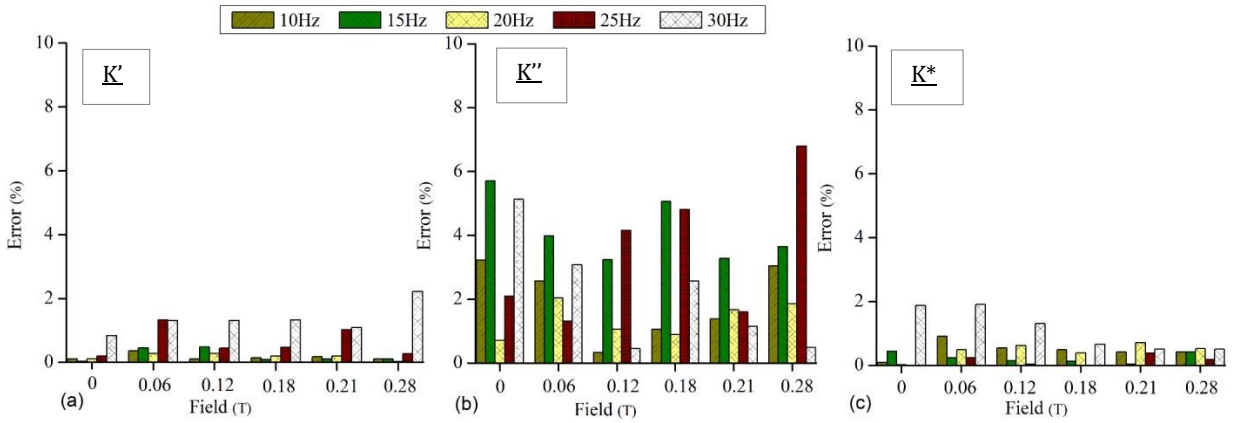

Figure 6-20: Percentage error between experimental and Predicted values for 0.004 rad (a) *K′* (b) *K″* (c) *K**

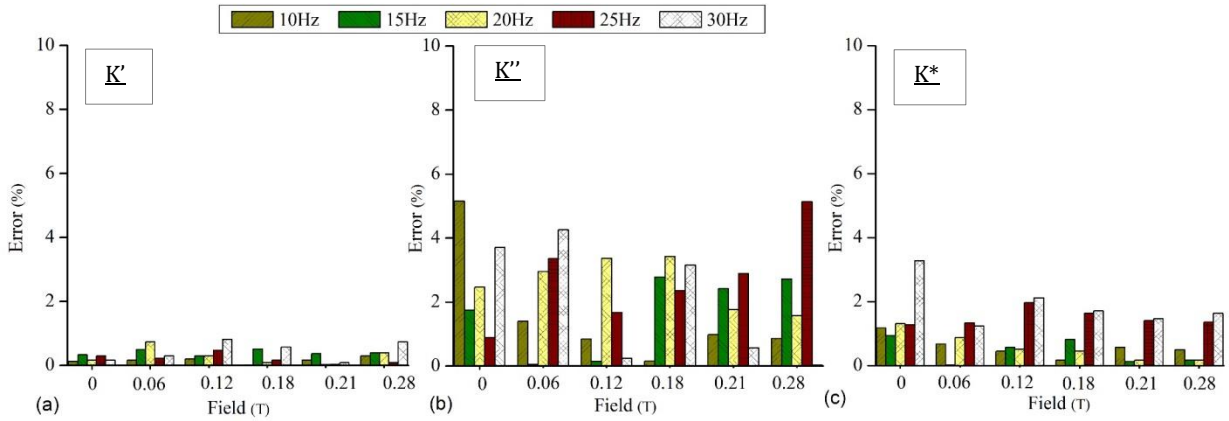

Figure 6-21: Percentage error between experimental and Predicted values for 0.008 rad (a) *K′* (b) *K″* (c) *K**

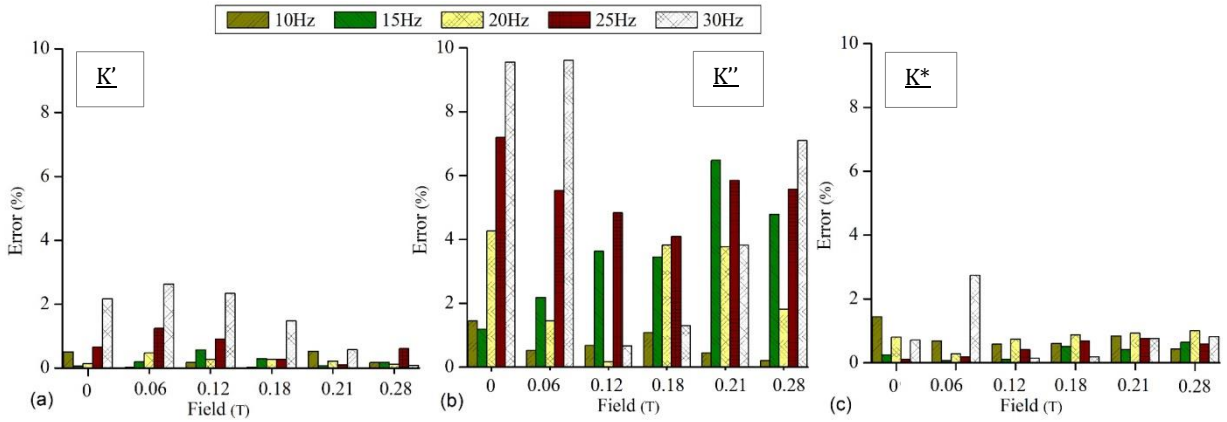

Figure 6-22: Percentage error between experimental and Predicted values for 0.012 rad (a) *K′* (b) *K″* (c) *K**

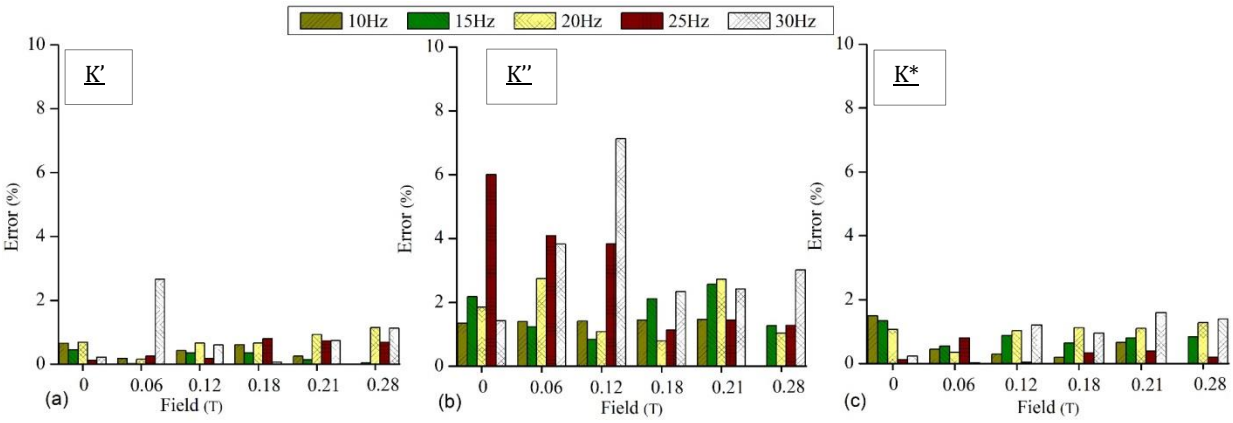

Figure 6-23: Percentage error between experimental and Predicted values for 0.016 rad (a) *K'* (b) *K''* (c) *K**

6.7. Fitness value of the fractional derivative-based Poynting-Thomson model

Figure 6-20- Figure 6-23 provided the graphical analogy of the ability of the proposed model to quantify the experimental data efficiently. Alternatively, a quantitative method, called "Fitness value" can also be adopted to understand the effectiveness of the proposed model. It represents the association between the torque value predicted by the fractional derivative-based Poynting-Thomson model and the measured torque from the experiments. The Fitness value is defined by the normalized RMS value of the experimental and the predicted data. It is given as,

$$Fitness\ Value\ (\%) = \left[1 - \frac{norm(T_{exp} - T_{md})}{norm(T_{exp} - mean(T_{exp}))}\right] \times 100 \qquad (6.13)$$

Where, T_{exp} represents the experimental torque data and T_{md} represents the modeled torque data. From the tabulated data (Table 6.6), it is observed that the fitness values are above 94.29%. This indicates that the proposed fractional based model can be effectively used to predict the angular displacement dependent, frequency-dependent and field-dependent properties of the MRE for the given range of torsional loading conditions.

Table 6.6: Fitness values for the proposed model

Amplitude (rad)	Field (T)	Frequency (Hz)				
		10	15	20	25	30
0.002	0	96.82	97.52	97.01	97.48	96.06
	0.06	95.39	97.30	96.02	98.02	96.06
	0.12	94.94	97.74	97.30	98.20	94.87
	0.18	96.06	97.65	97.96	97.64	94.98
	0.21	96.35	97.71	98.26	97.49	95.81
	0.28	96.24	97.68	97.84	97.35	95.32
0.004	0	96.86	98.17	97.16	95.74	96.06
	0.06	95.71	98.11	97.00	94.44	96.06
	0.12	95.44	98.18	97.06	95.94	94.85
	0.18	95.82	98.31	96.96	95.68	94.98
	0.21	96.70	98.46	97.01	95.75	95.81
	0.28	97.24	98.48	97.33	96.81	95.32
0.008	0	96.86	94.81	94.49	94.40	94.76
	0.06		95.76	94.39	94.96	96.77
	0.12	95.44	96.18	93.87	95.28	96.74
	0.18	95.82	96.32	94.01	95.66	96.68
	0.21	96.70	96.81	95.04	96.60	97.32
	0.28	97.24	97.32	96.60	97.61	97.36
0.012	0	96.59	95.26	95.92	95.01	93.39
	0.06	96.12	96.06	96.16	95.51	93.29
	0.12	97.03	97.00	97.41	95.72	95.11
	0.18	97.06	97.53	97.51	95.72	94.95
	0.21	97.90	97.93	97.63	96.74	94.29
	0.28	98.02	98.28	97.72	96.70	93.97
0.016	0	95.95	96.56	96.16	96.78	96.54
	0.06	95.52	97.38	95.74	97.24	95.28
	0.12	96.62	96.92	96.29	96.94	95.49
	0.18	97.32	97.18	96.12	96.61	95.83
	0.21	96.31	96.49	95.77	96.82	95.65
	0.28	95.87	96.48	96.01	96.99	94.99

6.8. Summary

The present chapter focused on constituting a relationship between the operating parameters. To comprehensively predict the viscoelastic behavior of the isolator, various parametric modeling approaches are available. Though the modified viscoelastic models, such as the Poynting Thomson model, predicts the behavior satisfactorily, the need for the addition of extra constitutive elements increases the computational efforts. The inclusion of fractional elements resolves the issue and the present study derives a fractional derivative-based Poynting Thomson model. It consists of six parameters obtained by minimizing the error between the experimental results and the modeled results.

With five levels of input frequency and angular displacement & six levels of the field, a total of 150 sets of experimental data are considered. The hysteresis plots suggest that the derived model accurately predicts the viscoelastic behavior of the MRE isolator for the given range of the parameters.

7. Experimental investigation of MRE based SDoF torsional isolation system

7.1. Introduction

In the previous chapters, an isotropic MRE isolator was prepared and characterized using the vlocked transfer stiffness method to evaluate its rheological properties under torsional loading conditions. The field-induced variations in the complex stiffness and the loss factor were evaluated for varying frequencies under variable angular displacements. Besides, a fractional derivative-based model was developed to comprehend the constitutive relations of the isolator parameters.

In the present chapter, a more detailed account on the application of the developed MRE isolator to effectively address and isolate the torsional vibrations is presented. The vibration attenuation is carried out on a custom made torsional SDoF system for rotors of various inertia, field and angular displacement. Following this, an evaluation of the variations in the system parameters of the torsional system is carried out.

7.2. Experimental Setup

The schematic for the Single Degree of Freedom (SDoF) torsional system is as shown in Figure 7-1. The SDoF system consists of two Aluminum shafts of negligible mass. The input shaft is connected to the electrodynamic shaker through a stinger. The shaft serves as the vibrating base from which harmonic disturbance of known amplitude is given to the torsional system. The harmonic input to the shaker is provided through an AGILENT 33220A function generator, which is amplified through an amplifier. Two accelerometers (YMC) are connected in the serial configuration on a massless disk, to measure the input accelerations. The acceleration values are numerically added to acquire the torsion vibration amplitudes of the system. The characterized MRE isolator is sandwiched between the two aluminum shafts, which provide the semi-active isolation to the torsional system. On the other end of the second shaft, disks of known inertia are added. Similar to the input, two accelerometers are attached to the inertial component (serial configuration), to measure the output acceleration amplitudes. The system is subjected to pure torsional vibrations by using bearings at appropriate locations to support the shafts and keep them in-line. With this, possible misalignment

of the shafts are removed. The signals are acquired and sent through a NI 9234 data acquisition system at a sampling rate of 25.6 kS/s, which is processed using LabVIEW 2014.

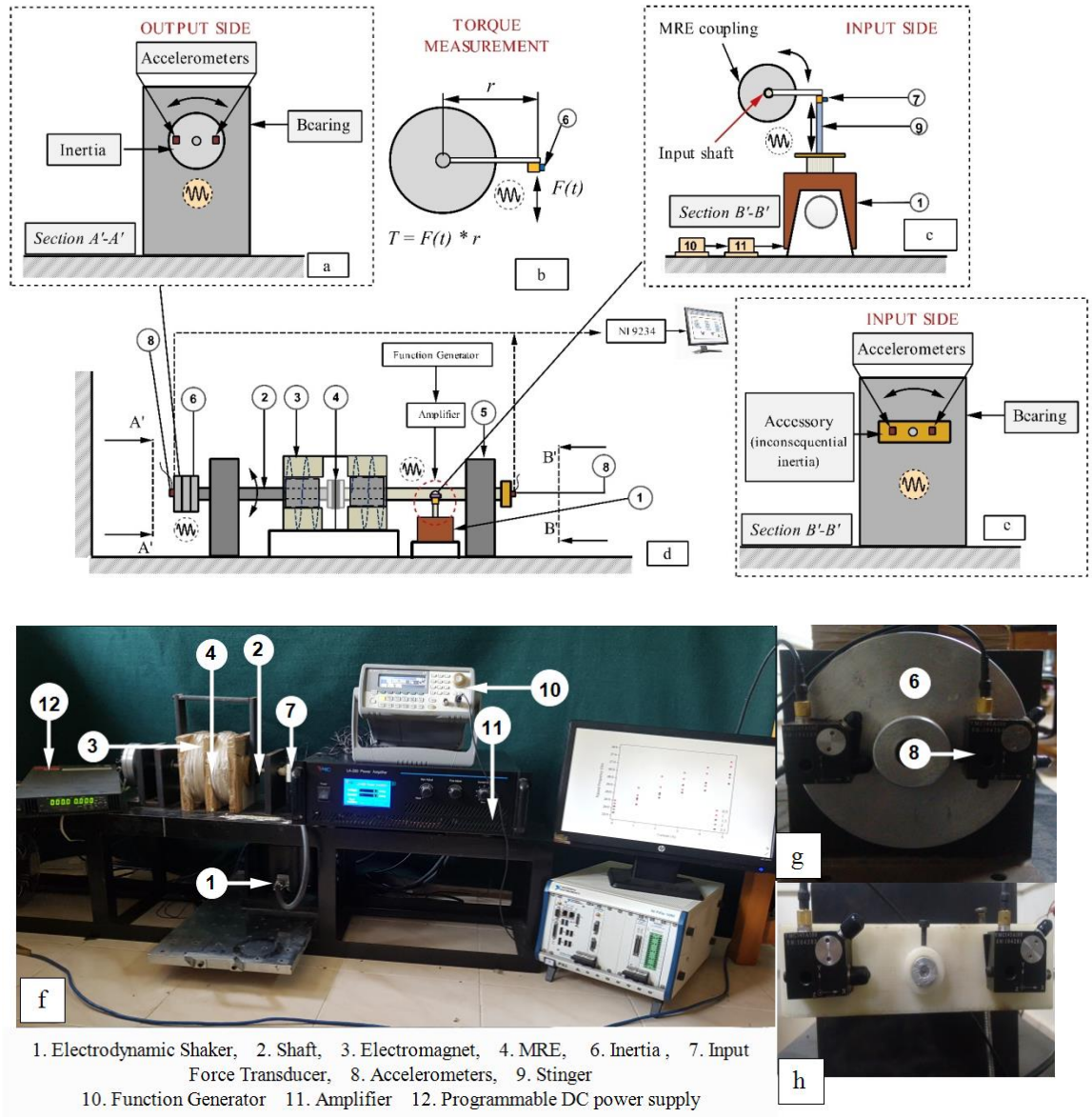

Figure 7-1: (a) Output Side (b) Torque Measurement (c) Torque applied (d) Schematic of the MRE based SDoF torsional isolation system (e) Input Side (f) Setup (g) SAA of the accelerometers at the output side (h) SAA of the accelerometers at the Input Side

7.3. Methodology

7.3.1. Determining the torsional vibrations

To differentiate the torsional mode from bending and lateral frequencies, the serial arrangement of accelerometers (SAA) (Kuang 1994) is adopted in the study. It

includes two identical accelerometers (equal sensitivity) arranged in serial combination, as shown in Figure 7-2 (b). SAA enhances the torsional natural frequency and the undesirable bending and lateral frequencies are restrained. Similarly, the parallel arrangement of accelerometers (Figure 7-2 a) enhances the bending frequency. For the lateral frequency mode, a single axis accelerometer is used in the direction of the impact force as shown in Figure 7-2 (c)

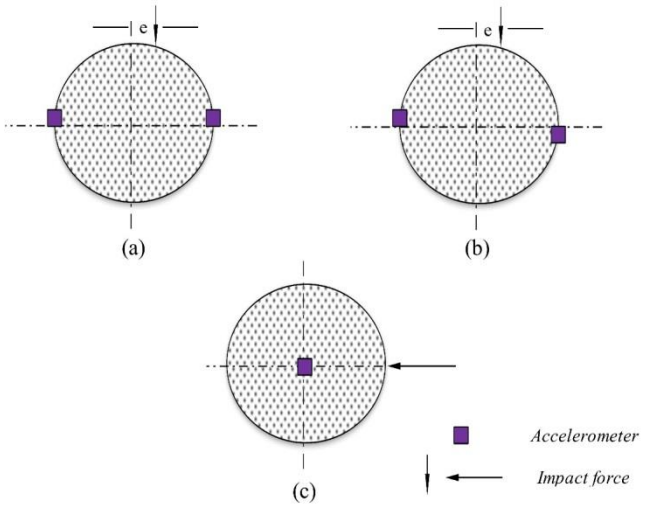

Figure 7-2: Accelerometer arrangements (a) Parallel combination (b) Serial combination (c) Lateral mode

The harmonic response for SAA is given as,

$$S_{ij}(\omega) = 2R\left\{\sum_{r=1}^{m}\frac{\theta_{ri}\theta_{rj}}{{\Omega_r}^2\left[1-\left(\frac{\omega}{\Omega_r}\right)^2\right]}\right\}T_j(\omega) \qquad ((7.1)$$

Wherein:

S_{ij} is the harmonic response in SAA measurement

$\theta_{ri}\theta_{rj}$ are the angular displacement terms of the ith amd jth term

Ω_r is the torsional natural frequency

T_j is the harmonic torque applied on the disks

The harmonic signal in torsional mode is given as,

$$S(\omega) = 2R\left\{\sum_{r=1}^{m}\frac{\theta^2}{{\Omega_r}^2\left[1-\left(\frac{\omega}{\Omega_r}\right)^2\right]}\right\}T_j(\omega) \quad ((7.2)$$

From the above, the Frequency Response Function (FRF) is given as,

$$FRF = \frac{S(\omega)}{T_j(\omega)} = 2R\left\{\sum_{r=1}^{m}\frac{\theta^2}{{\Omega_r}^2\left[1-\left(\frac{\omega}{\Omega_r}\right)^2\right]}\right\} \quad ((7.3)$$

7.3.2. Transmissibility

The isolation properties of the MRE under torsional vibrations are evaluated by measuring the transmissibility ratio of the vibrating base and rotors of inertial component. It is given as follows:

Let the harmonic input angular displacement to the shaft be given as

$$\theta(t) = \theta_0 \sin \omega t$$

Where θ_0 is the amplitude of the angular displacement and ω is the frequency.

The output angular displacement is given as γ. The corresponding equation of motion is,

$$J\ddot{\theta}_0(t) + c\left(\dot{\gamma}(t) - \dot{\theta}(t)\right) + k(\gamma(t) - \theta(t)) = 0 \quad ((7.4)$$

From the above, substituting for $\theta(t)$, and rearranging the terms, we get,

$$\frac{\gamma(t)}{\theta(t)} = \sqrt{\frac{1 + (2\zeta\eta')^2}{(1-\eta'^2)^2 + (2\zeta\eta')^2}} \quad ((7.5)$$

Where η is the frequency ratio and ζ represents the damping ratio

Table 7.1: Parameters for isolation assessment

Inertia (kg.m^2)	Magnetic field (T)	Angular displacement (rad)

	0	0.002
0.0002	0.06	0.008
0.00041	0.12	0.011
0.00082	0.18	0.015
0.0012	0.21	0.019
	0.28	

7.4. Results and Discussions

Figure 7-3 shows the field-dependent acceleration transmissibility plot for the rotor of inertia of 0.0002 kg.m^2 and angular displacement of 0.002 rad. The ordinate represents the ratio of the output acceleration to the input acceleration, while the abscissa represents the frequency of the torsional system. It is observed that the torsional natural frequency of the system under the absence of an external magnetic field is 25 Hz (Figure 7-3). With the increase in the magnetic field, there is a rightward shift in the frequency and it reaches a maximum of 28 Hz at 0.28 T. With an overall shift of 3 Hz, the graph reveals the field-induced increment in the torsional natural frequency of the MRE.

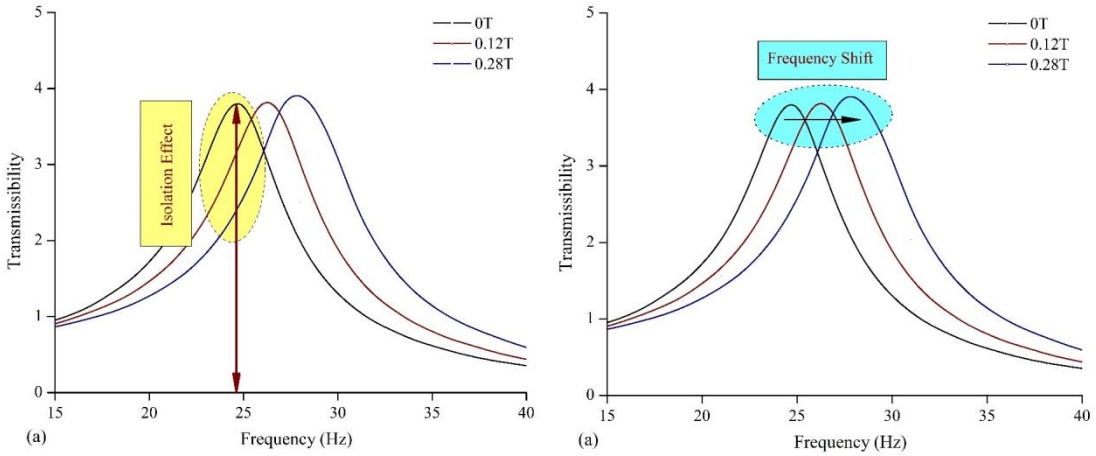

Figure 7-3: Isolation effect and Frequency shift for SDoF torsional isolation system

As discussed, the field-dependent increase in the torsional natural frequency is attributed to the field stiffening effect of the MRE. Under the influence of the magnetic field, the filler iron particles form dipoles, which increases the compressive force between the filler and the matrix, thereby increasing the stiffness of the MRE. The increased stiffness results in an increase in the torsional frequency of the MRE. Figure 7-4 depicts the frequency variations for the rest of the inertias and displacements.

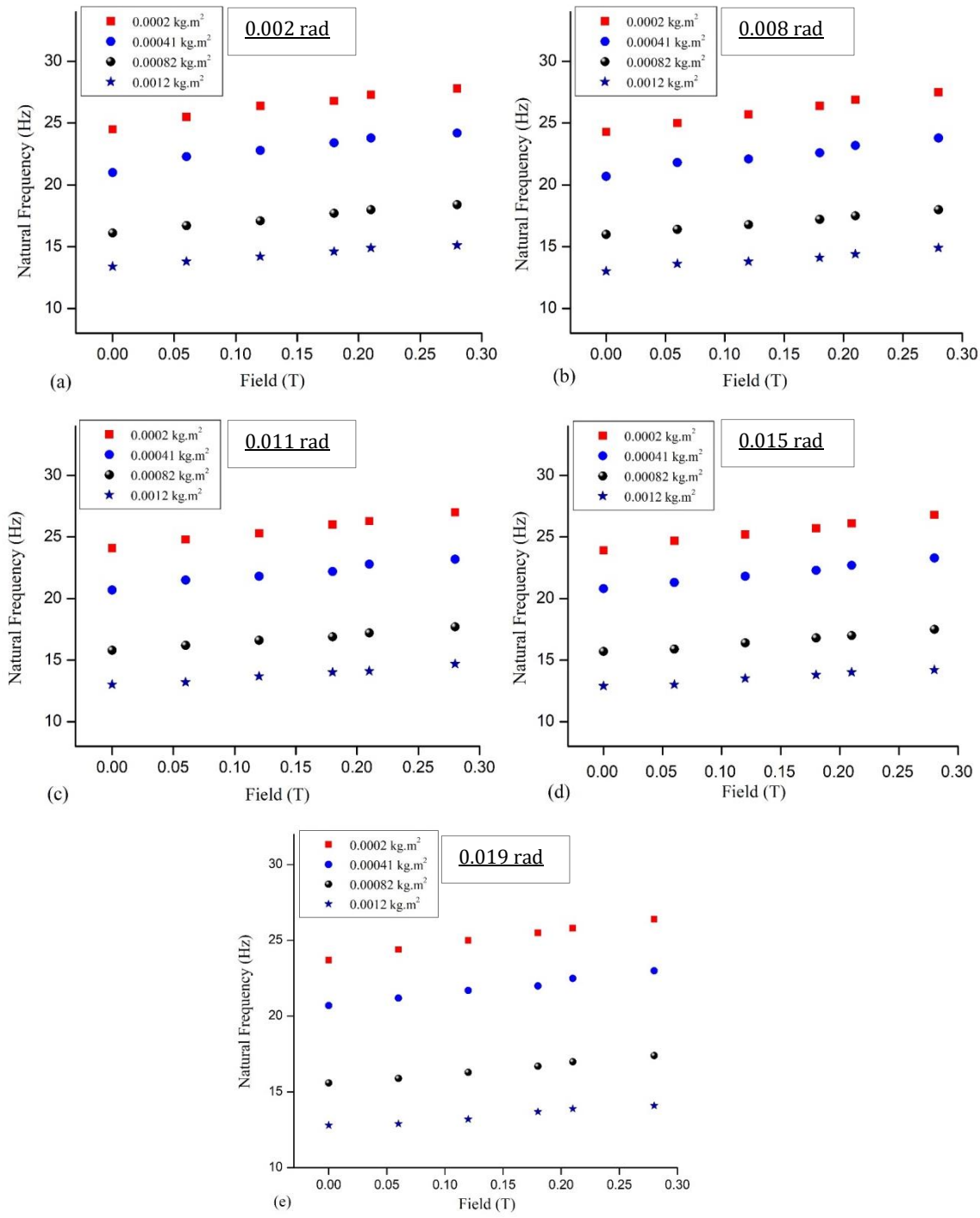

Figure 7-4: Natural Frequency variations for varying input displacements (a) 0.002 rad (b) 0.008 rad (c) 0.011 rad (d) 0.015 rad (e) 0.019 rad

7.5. Isolation effect

The field-induced shift in the torsional natural frequency highlights the semi-active isolation capabilities of the MRE. The reduction in the transmissibility ratio ascertains

the field-induced isolation capabilities of the MRE isolator (Figure 7-3 a). To analyze these reductions, the base transmissibility responses of the system are compared. The base transmissibility ratio of the system is defined as the field-induced transmissibility ratio of the system corresponding to the zero magnetic field condition.

Under the effect of the magnetic field, a shift in the natural frequency of the system is observed. This shift reduces the base transmissibility ratio and the reduction is further referred to as the isolation effect. Mathematically, it is defined as,

$$Isolation\ Effect\ (\%)\ = \left(\frac{T_{0T} - T_{mb}}{T_{0T}}\right) \times 100 \tag{7.6}$$

Where T_{0T} is the transmissibility of the system at 0T and T_{mb} is the Transmissibility of the system at a given field corresponding to the base frequency,f_0, (also termed as base transmissibility ratio). Table 7.2 presents the isolation effect for 0.0002 kg.m^2 at 0.002 rad.

Table 7.2: Isolation Effect (%) for 0.0002 kg.m^2 at 0.002 rad

Field (T)	Transmissibility Ratio (T_{mb})	Isolation Effect (%)
0	3.8	--
0.06	3.55	6.57
0.12	3.14	17.36
0.18	2.82	25.78
0.21	2.55	32.89
0.28	2.38	37.36

It is apparent that the transmissibility ratio reduces from 3.8 to 2.38, with an absolute reduction of 37.36%. Also, it is noticeable that the absolute isolation effect reduces with an increase in the magnetic field. In other words, the absolute decrease in the base transmissibility ratio reduces with an increase in the magnetic field. The decrease demonstrates the saturation of the field-induced variations between the fillers. The saturation thus results in reduced increment in the compressive forces on the matrix, thereby decreasing the relative shift in the torsional natural frequency. Figure 7-5 shows the exact nature of the reduction where the slope of the isolation effect reduces.

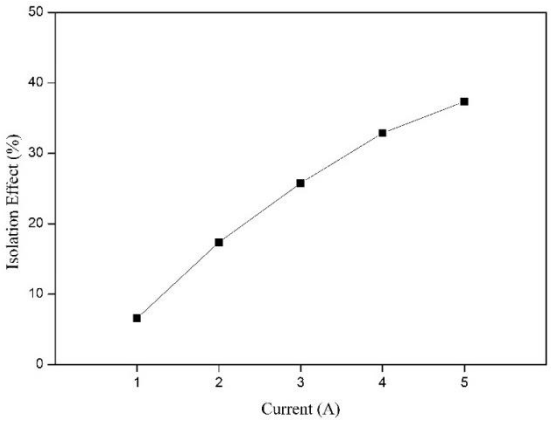

Figure 7-5: Absolute isolation effect variation with current

7.6. Effect of varying inertia and input displacement

Table 7.3 -Table 7.6 compiles the isolation effect of the MRE for different sets of inertia and angular displacement. Corresponding to the four rotors of inertia cases described in table (7.1), the base natural frequencies are 24 Hz (0.0002 kg.m^2), 21 Hz (0.00041 kg.m^2), 16.5 Hz (0.00082 kg.m^2) and 13 Hz (0.0012 kg.m^2). As discussed in the previous section, it is observed that the trend in the isolation effect remains the same for the given range of parameters. Figure 7-6 to Figure 7-9 shows the corresponding transmissibility plots.

Table 7.3: Isolation Effect for 0.0002 kg.m^2

B (T)	Transmissibility Ratio (T_{mb})					Isolation Effect (%)				
	0.002 rad	**0.008 rad**	**0.011 rad**	**0.015 rad**	**0.019 rad**	**0.002 rad**	**0.008 rad**	**0.011 rad**	**0.015 rad**	**0.019 rad**
0	3.80± 0.032	4.08± 0.029	4.30± 0.034	4.32± 0.036	4.36± 0.030	--	--	--	--	
0.06	3.54± 0.034	3.80± 0.034	3.90± 0.030	3.90± 0.029	3.95± 0.029	6.57	6.86	9.29	9.72	9.40
0.12	3.14± 0.036	3.38± 0.039	3.50± 0.036	3.50± 0.040	3.50± 0.036	17.36	17.15	18.60	18.98	19.72
0.18	2.82± 0.032	2.95± 0.027	3.05± 0.032	3.10± 0.029	3.15± 0.034	25.78	27.68	29.06	28.24	27.75
0.21	2.54± 0.019	2.80± 0.030	2.80± 0.039	2.95± 0.027	2.90± 0.036	32.89	31.37	34.88	31.71	32.34
0.28	2.38± 0.030	2.35± 0.029	2.50± 0.039	2.56± 0.040	2.61± 0.039	37.36	42.40	41.86	40.74	40.14

Table 7.4: Isolation Effect for 0.00041 kg.m^2

B (T)	Transmissibility Ratio(T_{mb})					Isolation Effect (%)				
	0.002 rad	0.008 rad	0.011 rad	0.015 rad	0.019 rad	0.002 rad	0.008 rad	0.011 rad	0.015 rad	0.019 rad
0	3.77± 0.031	4.04± 0.029	4.26± 0.031	4.37± 0.031	4.50± 0.032	-	-	-	-	-
0.06	3.28± 0.037	3.64± 0.036	4.00± 0.041	4.05± 0.039	4.15± 0.037	12.99	9.65	6.10	7.32	7.77
0.12	2.90± 0.030	3.38± 0.039	3.64± 0.040	3.70± 0.031	3.80± 0.034	22.07	16.34	14.32	15.33	15.56
0.18	2.65± 0.029	3.10± 0.040	3.40± 0.029	3.30± 0.039	3.40± 0.029	29.71	22.26	22.53	24.49	24.44
0.21	2.45± 0.039	2.70± 0.029	3.10± 0.031	3.00± 0.040	3.10± 0.041	35.01	33.17	27.23	31.35	31.11
0.28	2.20± 0.036	2.50± 0.030	2.80± 0.034	2.70± 0.031	2.80± 0.039	41.64	38.12	34.27	38.21	37.78

Table 7.5: Isolation Effect for 0.00082 kg.m^2

B (T)	Transmissibility Ratio (T_{mb})					Isolation Effect (%)				
	0.002 rad	**0.008 rad**	**0.011 rad**	**0.015 rad**	**0.019 rad**	**0.002 rad**	**0.008 rad**	**0.011 rad**	**0.015 rad**	**0.019 rad**
0	3.53± 0.041	4.43± 0.031	4.57± 0.031	4.61± 0.031	4.70± 0.031	-	-	-	-	-
0.06	3.30± 0.029	4.10± 0.042	4.30± 0.041	4.40± 0.039	4.40± 0.030	6.51	7.44	5.90	4.56	6.38
0.12	3.00± 0.031	3.60± 0.036	3.80± 0.039	3.90± 0.039	4.00± 0.036	15.01	14.22	16.84	15.40	14.89
0.18	2.75± 0.031	3.25± 0.031	3.40± 0.042	3.50± 0.039	3.60± 0.039	22.09	18.73	25.60	22.91	22.99
0.21	2.50± 0.036	2.90± 0.030	3.00± 0.031	3.20± 0.031	3.20± 0.041	29.18	34.53	34.54	30.59	31.91
0.28	2.30± 0.041	2.70± 0.049	2.70± 0.036	2.80± 0.042	2.90± 0.042	34.84	39.05	40.92	39.26	38.29

Table 7.6: Isolation Effect for 0.0012 kg.m^2

B (T)	Transmissibility Ratio(T_{mb})					Isolation Effect (%)				
	0.002 rad	**0.008 rad**	**0.011 rad**	**0.015 rad**	**0.019 rad**	**0.002 rad**	**0.008 rad**	**0.011 rad**	**0.015 rad**	**0.019 rad**
0	3.45± 0.031	4.16± 0.031	4.60± 0.031	4.70± 0.032	4.65± 0.040	-	-	-	-	-
0.06	3.30± 0.040	3.90± 0.037	4.20± 0.041	4.30± 0.034	4.50± 0.040	4.34	6.25	8.69	8.51	3.22
0.12	3.00± 0.032	3.50± 0.034	3.70± 0.034	3.90± 0.039	4.00± 0.031	13.04	15.86	19.56	17.02	13.98
0.18	2.80± 0.030	3.20± 0.032	3.30± 0.039	3.50± 0.036	3.60± 0.032	18.84	22.08	28.26	25.53	22.58
0.21	2.60± 0.039	3.00± 0.034	3.20± 0.034	3.20± 0.041	3.20± 0.036	24.63	27.88	30.43	31.91	31.18
0.28	2.29± 0.029	2.60± 0.040	2.70± 0.026	2.90± 0.042	2.80± 0.031	33.34	37.50	41.30	38.29	39.78

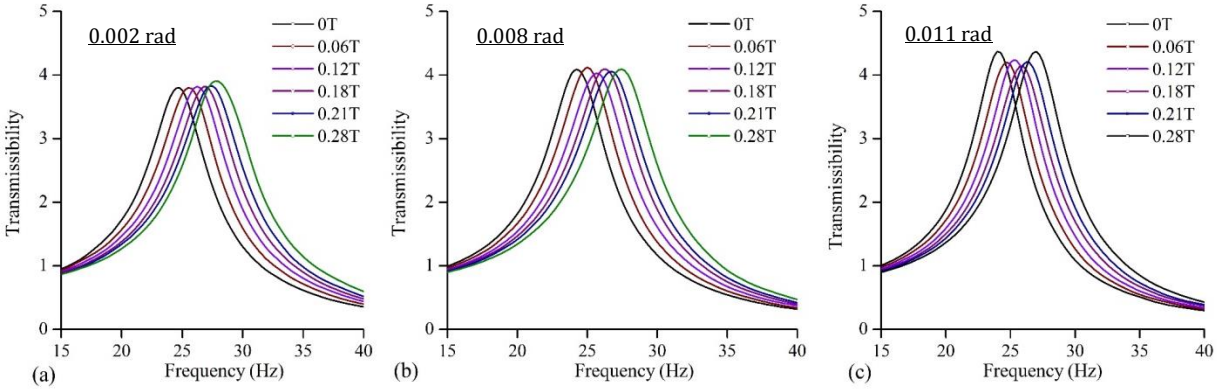

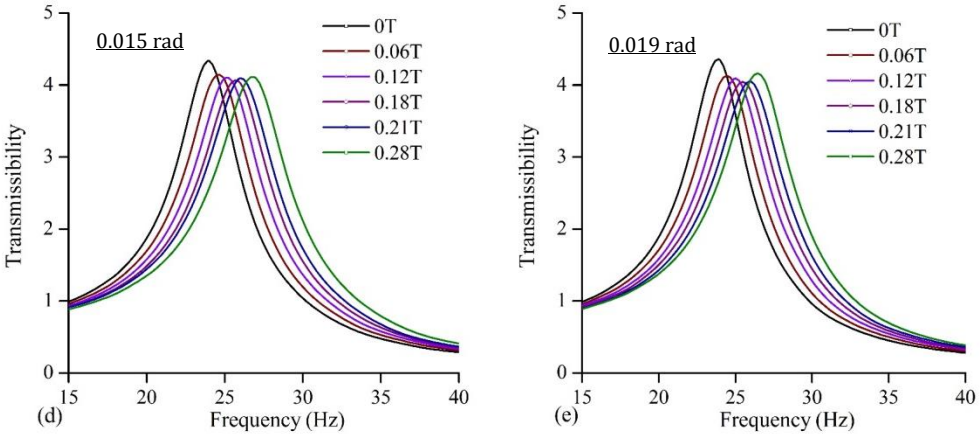

Figure 7-6: Field dependent Transmissibility curves at 0.0002 kg.m^2 at varying displacement (a) 0.002 rad (b) 0.008 rad (c) 0.011 rad (d) 0.015 rad (e) 0.019 rad

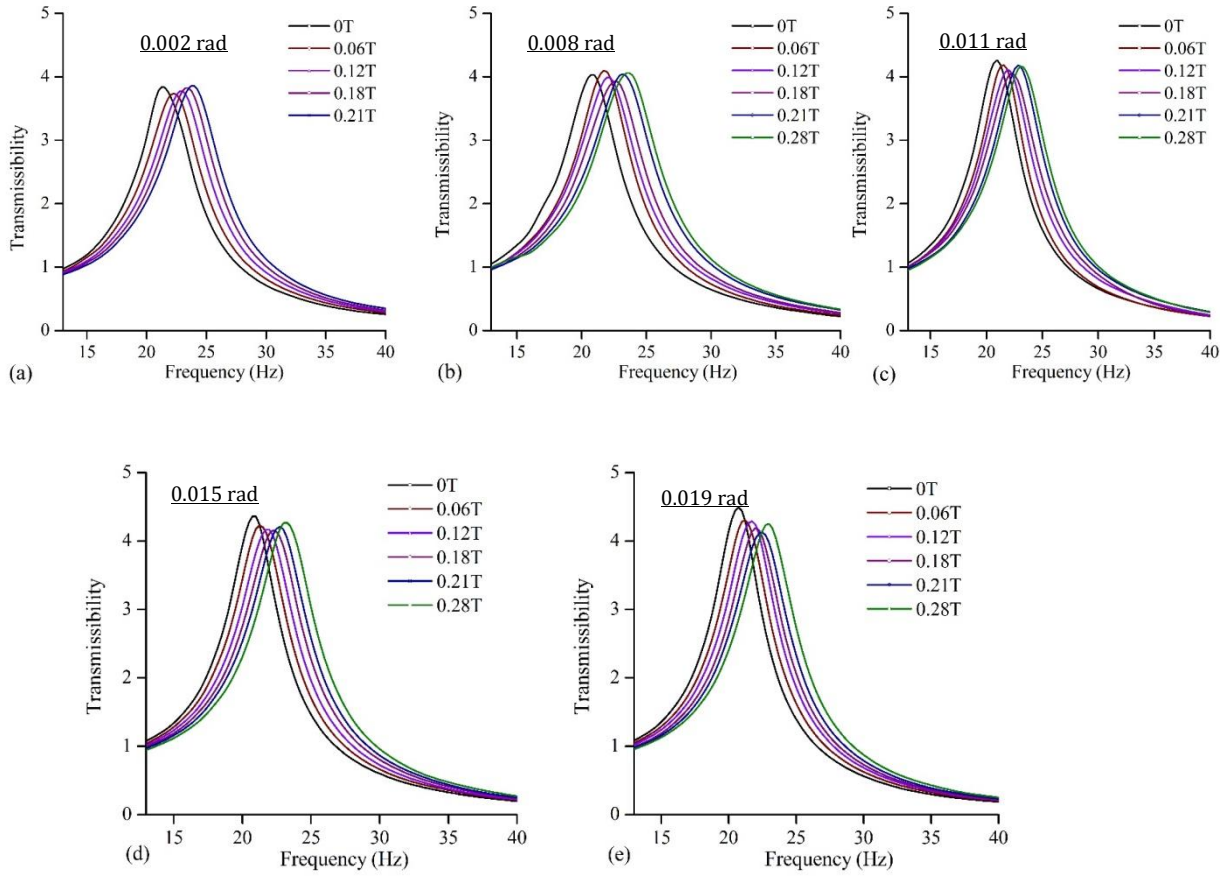

Figure 7-7: Field dependent Transmissibility curves at 0.00041 kg.m^2 at varying displacement (a) 0.002 rad (b) 0.008 rad (c) 0.011 rad (d) 0.015 rad (e) 0.019 rad

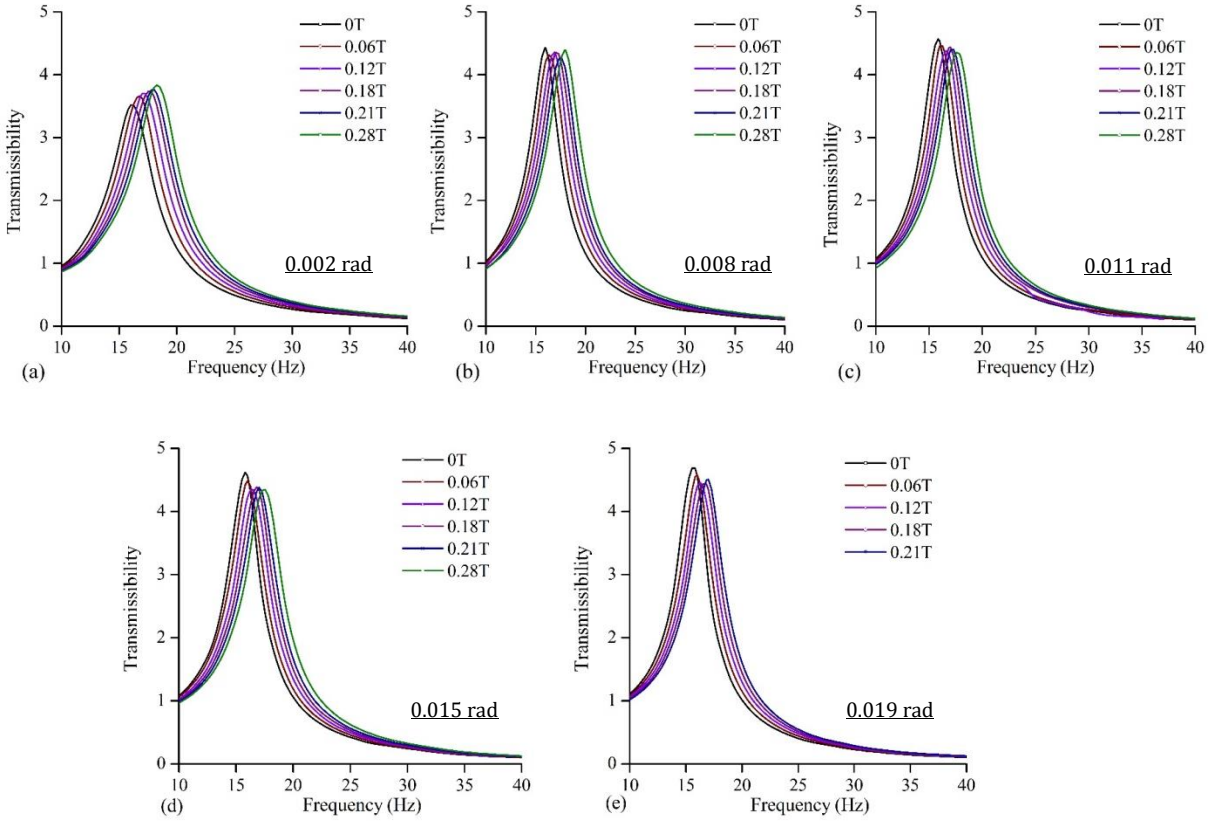

Figure 7-8: Field dependent Transmissibility curves at 0.00082 kg.m^2 at varying displacement (a) 0.002 rad (b) 0.008 rad (c) 0.011 rad (d) 0.015 rad (e) 0.019 rad

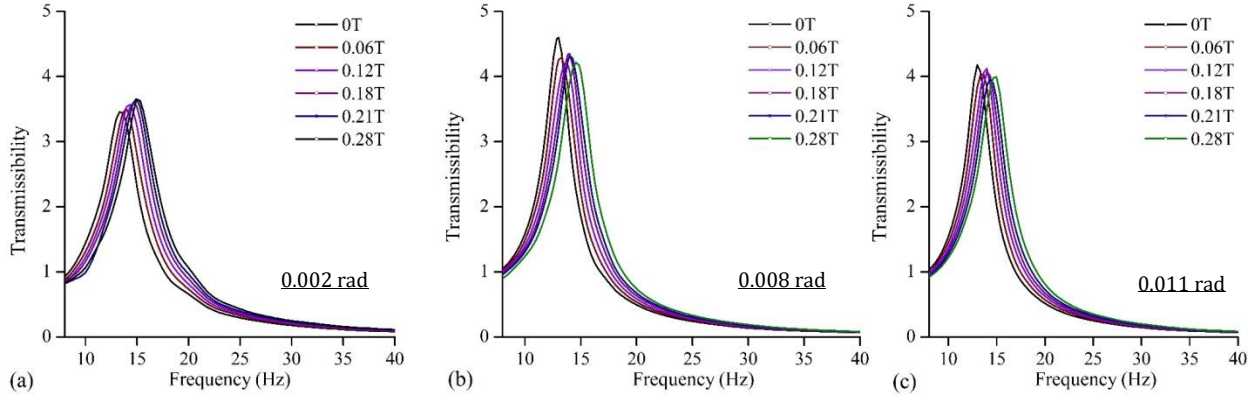

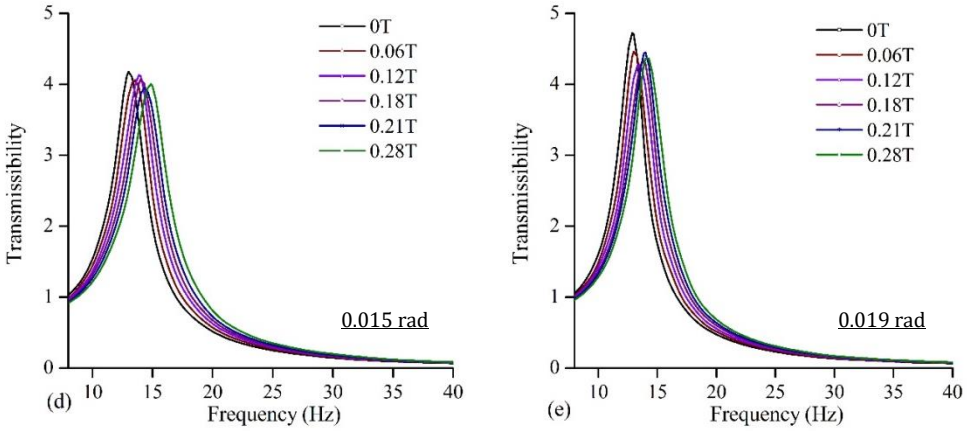

Figure 7-9: Field dependent Transmissibility curves at 0.0012 kg.m^2 at varying displacement (a) 0.002 rad (b) 0.008 rad (c) 0.011 rad (d) 0.015 rad (e) 0.019 rad

Figure 7-10 depicts the effect of the angular displacement on the dynamics of the SDoF torsional isolation system. It is indicated that the increase in the angular displacement decreases the torsional natural frequency of the system. As an example, for constant inertia of 0.0002 kg.m^2, the natural frequency of the system reduces from 24.5 Hz to 23.75 Hz with the increase in the angular displacement from 0.002 rad to 0.019 rad. A similar effect is apparent for the rest of the inertia and displacements. The reduction in the torsional natural frequency is attributed to the displacement dependent reduction of the complex stiffness of the MRE. As comprehended from chapter 5, the decrease in the complex stiffness of the MRE is explained using the Bound rubber theory. With the increase in the angular displacement, the stress concertation between the CIP and the rubber increases, subsequently forming a gap around the CIP. The formed gap leads to the reduction of intact bonds within the MRE, leading to a decrease in the overall torsional stiffness. With the reduction of the complex stiffness, the torsional natural frequency reduces as observed.

Also, an increase in the angular displacement reduces the absolute shift in the natural frequency of the torsional system. The frequency shift is defined as the difference in the natural frequency at no field condition with the natural frequency at the maximum field condition, given as,

$$Frequency\ Shift = (Natural\ Frequency)_{0.28T} - (Natural\ Frequency)_0 \quad (7.7)$$

To illustrate this (Figure 7-11, a), for constant rotors of inertia of 0.0002 kg.m^2, the field-dependent absolute shift in the torsional natural frequency at 0.002 rad is 3.3 Hz. With the displacement increased to 0.019 rad, the absolute shift reduces to 2.7 Hz. Similar results are observed for the rest of the inertia.

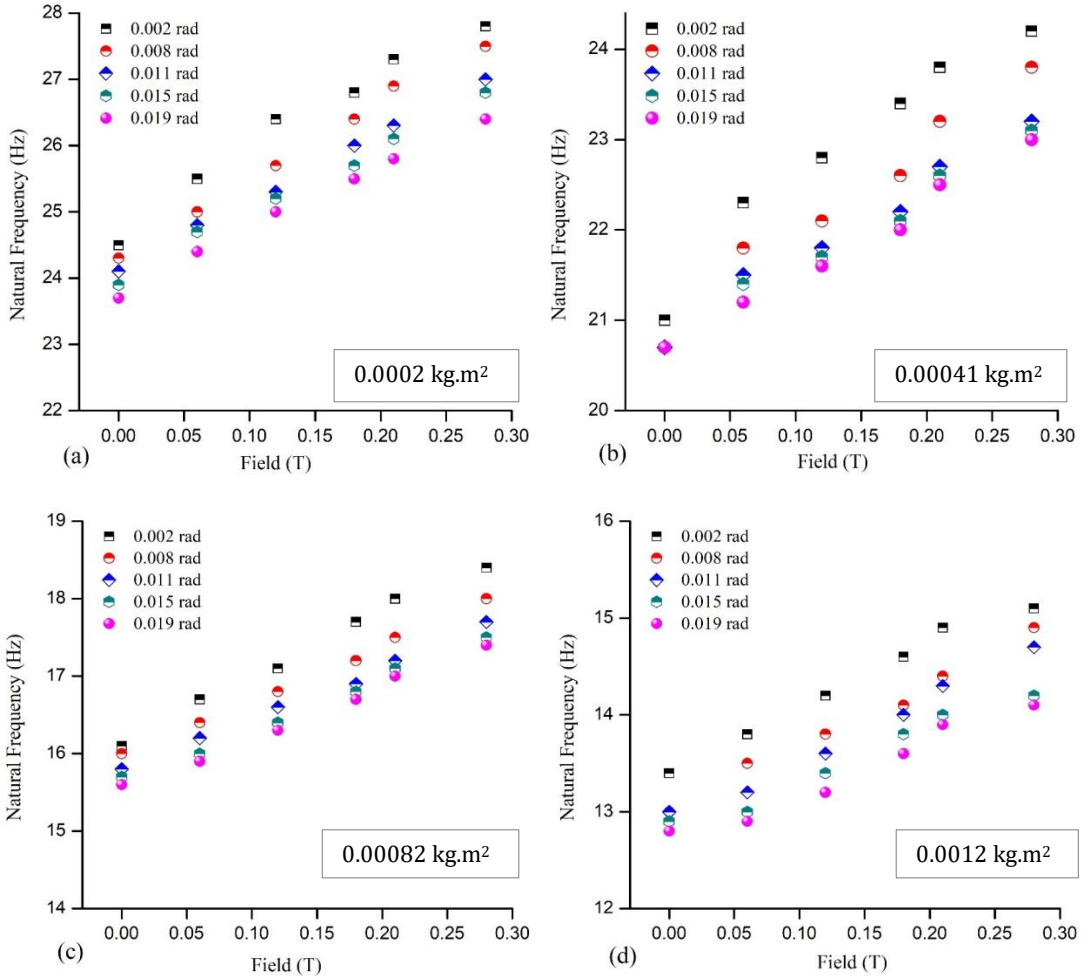

Figure 7-10: Influence of input displacement on natural frequency (a) 0.0002 kg.m^2 (b) 0.00041 kg.m^2 (c) 0.00082 kg.m^2 (d) 0.0012 kg.m^2

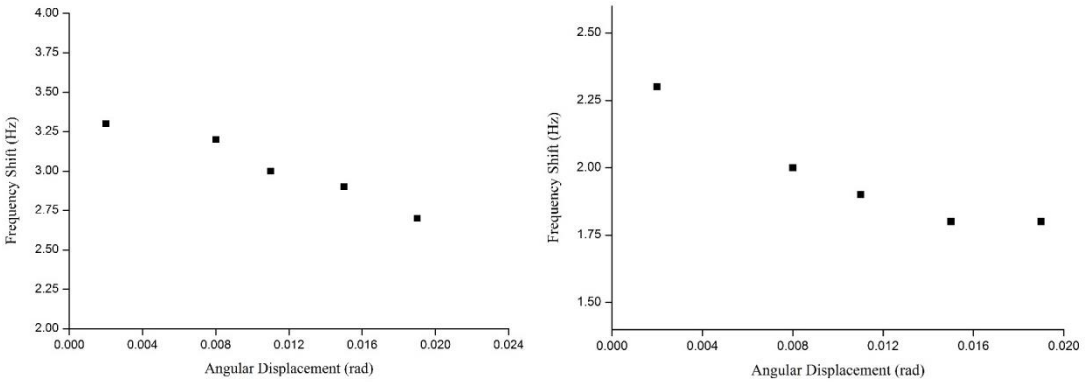

Figure 7-11: Frequency shift variations with displacement at inertia of (a) 0.0002 kg.m^2 (b) 0.00041 kg.m^2

7.7. Relation between base transmissibility ratio (T_{mb}), applied field and angular displacement

The relation between the base transmissibility ratio (T_{mb}), applied field and the input angular displacement is as illustrated in Figure 7-12. It is observed that irrespective of the applied field, the base transmissibility ratio increases with an increase in the angular displacement. This suggests the reduction of the isolation capabilities of the MRE isolator for torsional vibrations. The reduction in the isolation ability is attributed to the reduction of the complex stiffness of the MRE isolator.

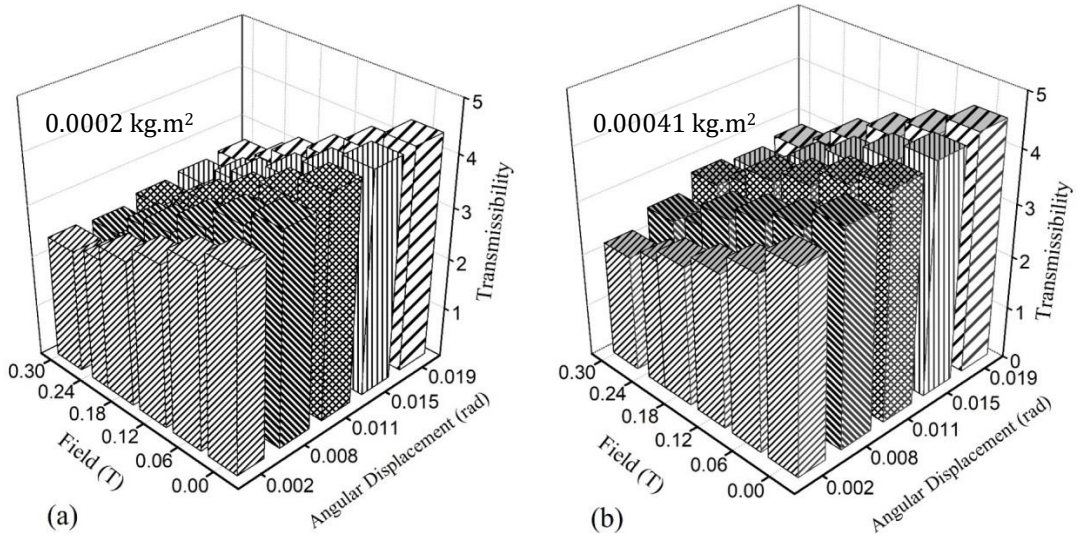

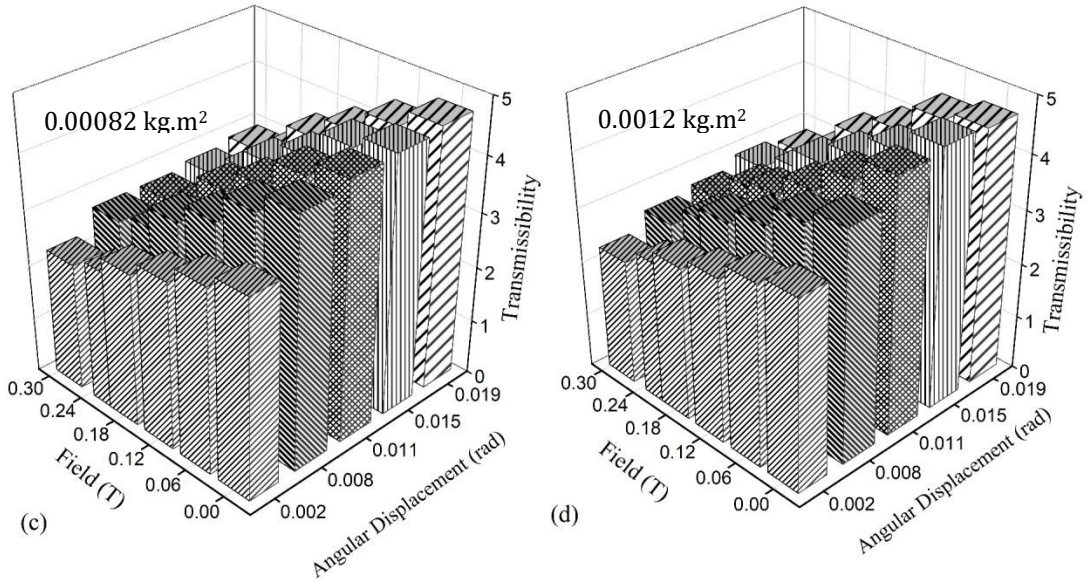

Figure 7-12: base transmissibility ratio variation for field and displacement fields (a) 0.0002 kg.m^2 (b) 0.00041 kg.m^2 (c) 0.00082 kg.m^2 (d) 0.0012 kg.m^2

7.8. Field dependent Transmissibility ratio variations for varying input displacement

Apart from the isolation effect, the damping capabilities of the MRE isolator under varying parameters are also explored. Figure 7-13 shows the amplitude variations of the peak transmissibility ratio corresponding to different fields. Peak Transmissibility ratio represents the transmissibility values for individual Transmissibility curves. From the figure, it is observed that the field-dependent variations across the angular displacements are inconsistent. This is true for all the measured values across the rotors inertia. Similar results are highlighted in the cases of vibration isolators where the peaks vary inconsistently (Behrooz et al. 2014b)(Lee et al. 2019)(Hashi et al. 2016)

The results correlate the variations observed in the loss factor for the characterization of the MRE isolator. These variations suggest that the MRE, while effectively performs as an isolator, cannot effectively be used a damper for torsional vibration isolation. From the point of view of implementing a control strategy, this reveals an important aspect. During vibration control, it is seen that the stiffness is varied at any given resonant frequency by changing the field induced. This reduces the amount of vibration transmitted from the base to the system. However, it is seen that this works until the operating frequency is at the resonant frequency of the system at

0T. Once the operating speed varies, it becomes mandatory for the control system to change the stiffness compulsorily to change the resonant frequency. This remains to be true for all amplitudes within the linear viscoelastic range.

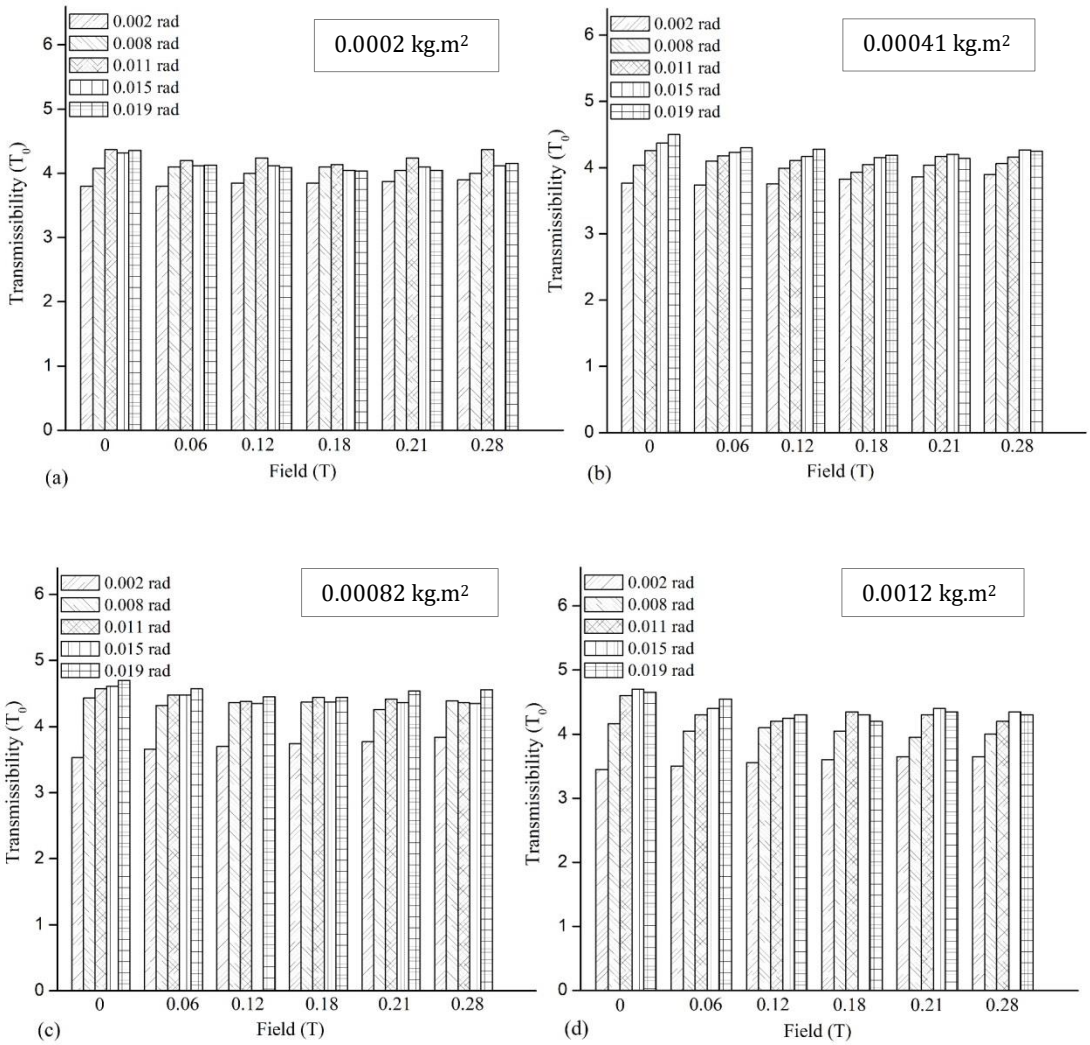

Figure 7-13: Peak Transmissibility ratio variation at varying fields (a) 0.0002 kg.m^2 (b) 0.00041 kg.m^2 (c) 0.00082 kg.m^2 (d) 0.0012 kg.m^2

7.9. System Parameters

The calculation of the system parameters (Stiffness and Damping) is carried out, and the values are presented in the following sections.

7.9.1. Stiffness

Figure 7-14 shows the field-dependent variations in the torsional stiffness of the MRE isolator system for 0.002 rad and 0.00041 kg. m^2. At 0T (0A), the stiffness of the system is found to be 6.96 N.m rad^{-1}. Under the influence of the magnetic field, there is a considerable increase in the torsional stiffness. At a maximum of 0.28T (5A), the stiffness increases to 9.4 N.m rad^{-1}. Similar variations are observed for the rest of the measured parameters and the values are tabulated in Table 7.7- Table 7.8.

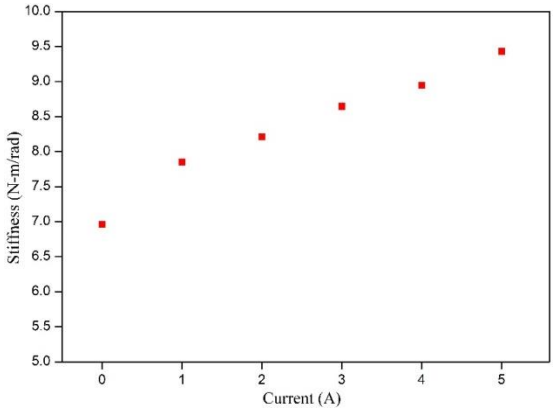

Figure 7-14: Variation of system stiffness with varying input current for 0.002 rad and 0.00041 kg. m^2

Table 7.7: Torsional stiffness for 0.0002 kg.m^2 and 0.00041 kg.m^2

I (A)	Stiffness (N.m rad^{-1})									
	0.0002 kg.m^2					**0.00041 kg.m^2**				
	0.002 rad	**0.008 rad**	**0.011 rad**	**0.015 rad**	**0.019 rad**	**0.002 rad**	**0.008 rad**	**0.011 rad**	**0.015 rad**	**0.019 rad**
0	4.74± 0.092	4.66± 0.092	4.58± 0.090	4.49± 0.104	4.43± 0.090	6.96± 0.102	6.76± 0.099	6.76± 0.102	6.76± 0.104	6.76± 0.106
1	5.13± 0.099	4.89± 0.106	4.84± 0.102	4.82± 0.100	4.70± 0.094	7.81± 0.107	7.50± 0.090	7.29± 0.102	7.21± 0.106	7.09± 0.096
2	5.50± 0.100	5.21± 0.096	5.04± 0.098	5.01± 0.090	4.89± 0.096	8.20± 0.096	7.71± 0.096	7.50± 0.096	7.43± 0.109	7.36± 0.096
3	5.67± 0.090	5.50± 0.092	5.34± 0.089	5.21± 0.096	5.09± 0.096	8.64± 0.090	8.06± 0.089	7.78± 0.096	7.71± 0.096	7.64± 0.104
4	5.88± 0.101	5.71± 0.088	5.46± 0.096	5.38± 0.101	5.26± 0.090	8.94± 0.096	8.49± 0.090	8.13± 0.090	8.06	7.99± 0.106
5	6.10± 0.106	5.96± 0.090	5.71± 0.102	5.67± 0.092	5.50± 0.091	9.42± 0.102	8.94± 0.090	8.49± 0.090	8.42± 0.096	8.32± 0.106

Table 7.8: Torsional stiffness for 0.0082 kg.m^2 and 0.0012 kg.m^2

I (A)	Stiffness (N.m rad^{-1})									
	0.00082 kg.m^2					**0.0012 kg.m^2**				
	0.002 rad	**0.008 rad**	**0.011 rad**	**0.015 rad**	**0.019 rad**	**0.002 rad**	**0.008 rad**	**0.011 rad**	**0.015 rad**	**0.019 rad**
0	8.44± 0.102	8.31± 0.104	8.10± 0.101	8.02± 0.101	7.92± 0.102	8.76± 0.103	8.27± 0.101	8.29± 0.101	8.12± 0.106	8.00± 0.104
1	9.08± 0.102	8.76± 0.104	8.54± 0.102	8.31± 0.100	8.21± 0.101	9.29± 0.102	8.89± 0.090	8.50± 0.109	8.24± 0.106	8.12± 0.104
2	9.52± 0.106	9.19± 0.090	8.97± 0.106	8.76± 0.096	8.61± 0.100	9.84± 0.109	9.29± 0.102	9.03± 0.102	8.76± 0.101	8.50± 0.107
3	10.20± 0.109	9.61± 0.096	9.30± 0.096	9.16± 0.090	9.08± 0.101	10.40± 0.101	9.70± 0.106	9.57± 0.106	9.29± 0.102	9.03± 0.103
4	10.51± 0.101	9.97± 0.097	9.63± 0.096	9.52± 0.096	9.41± 0.090	10.84± 0.104	10.12± 0.102	9.98± 0.109	9.56± 0.101	9.43± 0.101
5	11.02± 0.109	10.51±0.102	10.20± 0.104	9.97± 0.090	9.86± 0.101	11.13± 0.103	10.84± 0.103	10.50± 0.106	9.84± 0.104	9.70± 0.102

7.9.1. Damping Ratio and Damping Coefficient

Figure 7.16 shows the variation of damping ratio with the input current for various inertia. Unlike the stiffness variation, there is an absence of a clear trend in the damping

Furthermore, table 7.9, 7.10 shows the Damping Coefficients for all the parameters.

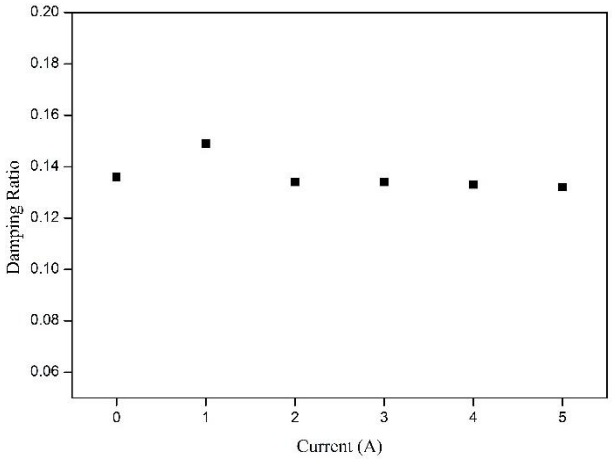

0.0002 kg.m^2

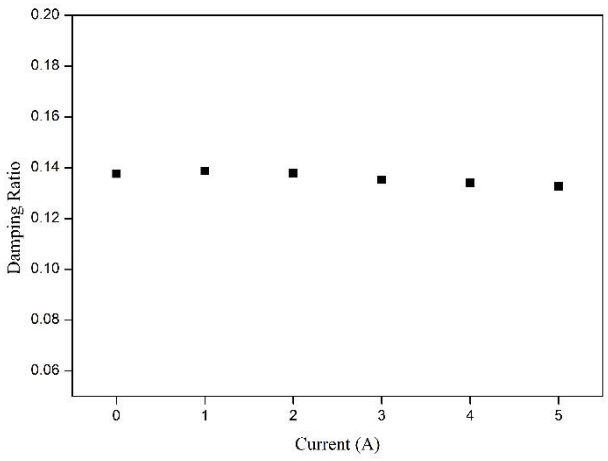

0.00041 kg.m^2

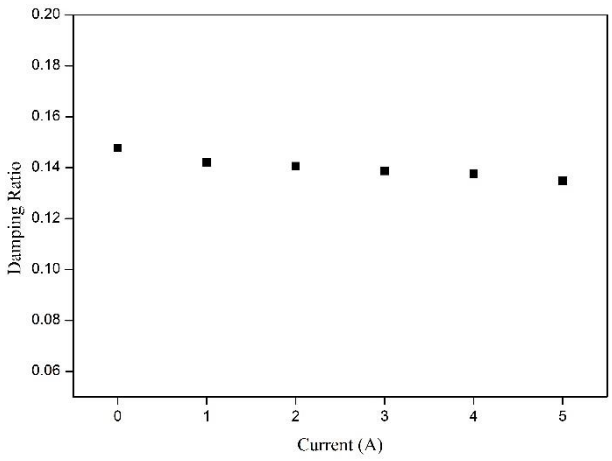

0.0082 kg.m^2

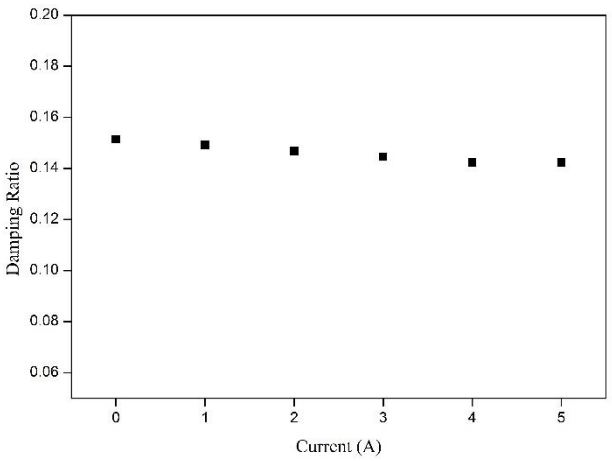

0.0012 kg.m^2

Figure 7-15: Damping ratio

Table 7.9: Damping Coefficient for 0.0002 and 0.00041 kg.m^2

I (A)	Damping Coefficient (kg.m^{2}rad^{-1}sec^{-1})(10^{-2})									
	0.0002 kg.m^2					**0.00041 kg.m^2**				
	0.002 rad	**0.008 rad**	**0.011 rad**	**0.015 rad**	**0.019 rad**	**0.002 rad**	**0.008 rad**	**0.011 rad**	**0.015 rad**	**0.019 rad**
0	0.84± 0.016	0.77± 0.019	0.71± 0.014	0.71± 0.019	0.70± 0.017	1.45± 0.012	1.33± 0.019	1.26± 0.019	1.22± 0.016	1.19± 0.019
1	0.87± 0.012	0.79± 0.016	0.76± 0.012	0.78± 0.013	0.77± 0.019	1.54± 0.013	1.38± 0.016	1.33± 0.013	1.31± 0.019	1.28± 0.016
2	0.89± 0.019	0.83± 0.017	0.77± 0.012	0.79± 0.017	0.79± 0.019	1.58± 0.016	1.47± 0.013	1.37± 0.016	1.34± 0.014	1.30± 0.020
3	0.91± 0.017	0.83± 0.017	0.81± 0.016	0.82± 0.017	0.82± 0.016	1.59± 0.017	1.49± 0.014	1.42± 0.017	1.38± 0.012	1.36± 0.012
4	0.92± 0.019	0.86± 0.016	0.80± 0.016	0.82± 0.019	0.83± 0.014	0.0160	1.49± 0.019	1.41± 0.014	1.39± 0.020	1.41± 0.019
5	0.93± 0.019	0.89± 0.016	0.79± 0.019	0.84± 0.016	0.82± 0.016	1.63± 0.016	1.52± 0.019	1.44± 0.014	1.40± 0.020	1.40± 0.019

Table 7.10: Damping Coefficient for 0.0082 and 0.0012 kg.m^2

I (A)	Damping Coefficient (kg.m^2 rad^{-1}sec^{-1}) (10^{-2})									
	0.00082 kg.m^2					**0.0012 kg.m^2**				
	0.002 rad	**0.008 rad**	**0.011 rad**	**0.015 rad**	**0.019 rad**	**0.002 rad**	**0.008 rad**	**0.011 rad**	**0.015 rad**	**0.019 rad**
0	2.43± 0.019	1.89± 0.019	1.81± 0.020	1.78± 0.020	1.73± 0.016	3.11± 0.016	2.46± 0.017	2.22± 0.014	2.15± 0.014	2.16± 0.013
1	2.42± 0.014	1.99± 0.013	1.89± 0.019	1.87± 0.020	1.82± 0.014	3.30± 0.014	2.63± 0.013	2.41± 0.017	2.29± 0.013	2.22± 0.016
2	2.45± 0.013	2.02± 0.013	1.99± 0.013	1.98± 0.017	1.92± 0.019	3.19± 0.019	2.66± 0.016	2.55± 0.019	2.48± 0.019	2.42± 0.019
3	2.51± 0.016	2.06± 0.019	1.99± 0.017	2.01± 0.014	1.97± 0.019	3.24± 0.013	2.71± 0.019	2.53± 0.019	2.53± 0.014	2.54± 0.019
4	2.53± 0.012	2.16± 0.018	2.04± 0.014	2.06± 0.019	1.96± 0.017	3.26± 0.017	2.88± 0.019	2.62± 0.016	2.50± 0.016	2.51± 0.014
5	2.53± 0.019	2.15± 0.016	2.12± 0.014	2.11± 0.014	2.00± 0.014	3.29± 0.016	2.94± 0.020	2.74± 0.020	2.57± 0.019	2.59± 0.014

7.10. Overview

In the present chapter, the implementation of the MRE isolator for the torsional vibration isolation is studied. The study is carried out on a custom made SDoF torsional system. The constant torsional oscillations were provided by a shaker at a fixed distance from the axis of the shaft. The input and the output angular displacements were measured as per the Serial Arrangement of the Accelerometers (SAA) technique, which provides the torsional modes of the system. Isolation of the vibration is measured by the amount of the reduction in the transmissibility ratios of the system. The plots reveal a shift in the natural frequency of the system under the influence of the magnetic fields. Due to this, the transmissibility ratio of the system reduces. Similarly, the effect of the damping was also addressed, though the trends revealed inconsistency. Following this, an evaluation of the system parameters of the torsional system is carried out.

8. Model-based PID controller for MRE torsional vibration isolation

8.1. Introduction

The Real-time implementation of the MRE torsional vibration isolation depends on the control current supplied to the electromagnet. The designed control is needed to change the input current based on the output of the MRE isolator. To achieve the semi-active vibration control with the MRE isolator, the current control to the flux is achieved with a Proportional-Integral-Derivative (PID) feedback loop applied in the time domain. The PID controller is developed based on the parametric modeling derived in chapter 6.

The initial discussions focus on extracting the field-dependent function equations from the six parameters of the derived parametric model. Following this, the general differential equation of the SDoF torsional isolation system is revisited with the focus on the shift in the torsional natural frequency under the applied field. The corresponding stiffness and damping coefficient of the SDoF system are tabulated. With the obtained values, the state space equations are derived. The latter sections discuss the simulation of the model-based PID controller.

8.2. Identification of the function parameters for the fractional derivative based Pointing-Thomson model

It was observed in chapter 6 that the six parameters of the fractional model were dependent on the applied magnetic fields. Hence, for the implementation of the model-based control, the identification of the field-dependency of the parameters is essential. Following this, the six parameters for the MRE isolator for 20Hz, 0.016 rad is tabulated in Table 8.1

Table 8.1: Parameters for 20 Hz, 0.016 rad

I(A)	K_1	K_2	K_3	C_2	C_3	α
0	19.324	6.099	2.784	0.0136	0.0114	0.790
1	19.449	6.302	2.822	0.0144	0.0108	0.796
2	19.599	6.494	2.840	0.0150	0.0107	0.806
3	19.742	6.643	2.869	0.0156	0.0099	0.818
4	19.882	6.769	2.902	0.0160	0.0092	0.821
5	19.996	6.862	2.942	0.0167	0.0086	0.829

Each of the above parameters is plotted for varying current and the relationship between the individual parameters with the current is depicted in Figure 8-1.

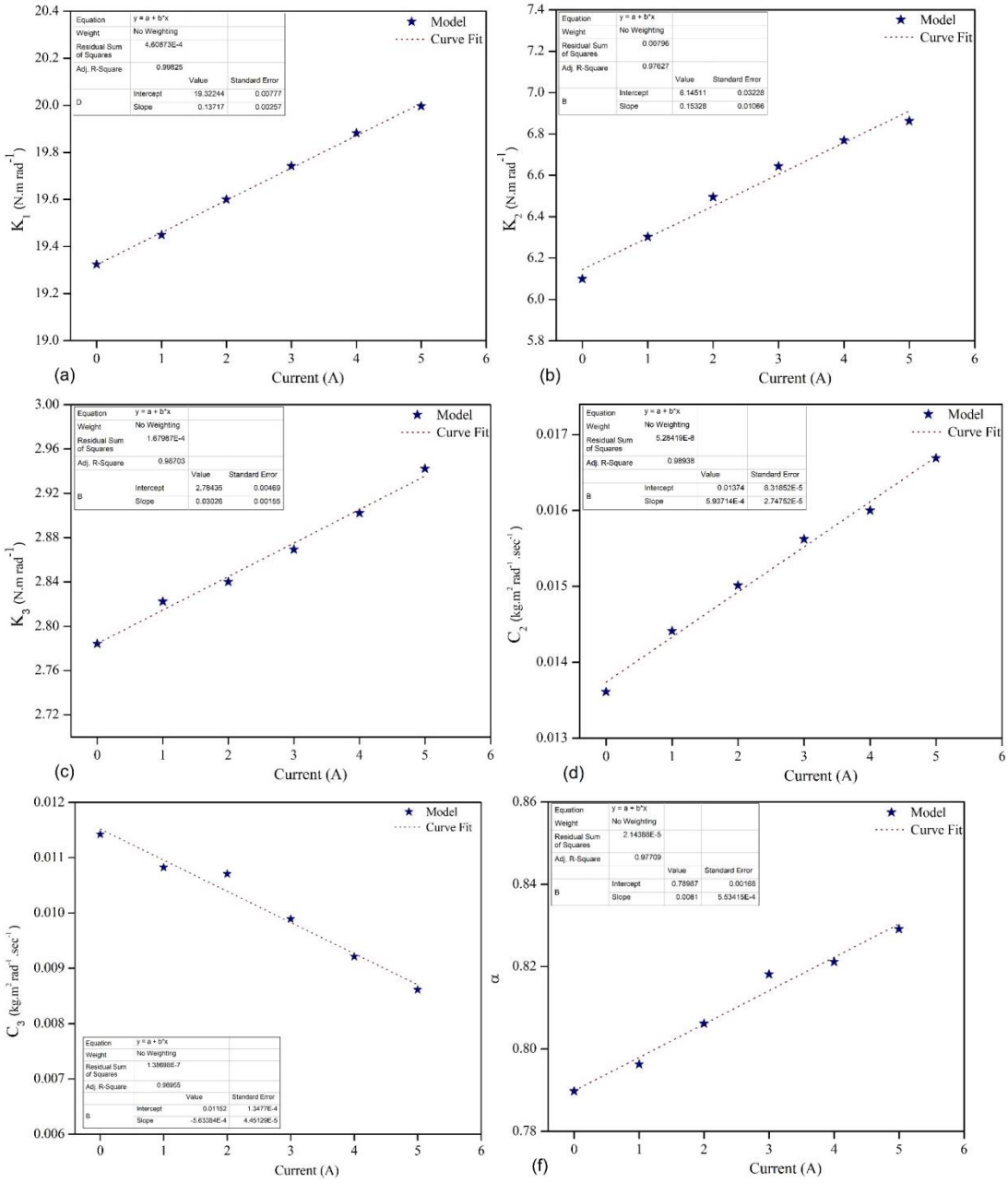

Figure 8-1: Relationship between the parameters and the field. Experimental and fitted data for (a) K_1 (b) K_2 (c) K_3 (d) C_2 (e) C_3 (f) α for 20 Hz, 0.016 rad

From Figure 8-1, it is comprehended that the parameters vary linearly with the current, suggesting that the parameters can be explained as a linear function of the applied input current to the electromagnet. The expressions for the parameters of the MRE isolator is,

$$
\begin{aligned}
K_1 &= K_{10} + iK_{1b} \\
K_2 &= K_{20} + iK_{2b} \\
K_3 &= K_{30} + iK_{3b} \\
C_2 &= C_{20} + iC_{2b} \\
C_3 &= C_{30} + iC_{3b} \\
\alpha &= \alpha_0 + i\alpha_b
\end{aligned}
\tag{8.1}
$$

Where *i* is the input current to the electromagnet

The identified parameters for the corresponding linear functions from the above equation are tabulated below.

Table 8.2: Function parameters for the viscoelastic modeling **(**20 Hz, 0.016 rad)

Parameters	
K_{10} (N.m rad^{-1})	19.322
iK_{1b} (N.m rad^{-1})	0.137
K_{20} (N.m rad^{-1})	6.145
iK_{2b} (N.m rad^{-1})	0.153
K_{30} (N.m rad^{-1})	2. 784
iK_{3b} (N.m rad^{-1})	0.0302
C_{20}(kg.m^2 rad^{-1} .sec^{-1})	0.01377
iC_{2b}(kg.m^2 rad^{-1} .sec^{-1})	5.93714E-4
C_{30}(kg.m^2 rad^{-1} .sec^{-1})	0.01152
iC_{3b}(kg.m^2 rad^{-1} .sec^{-1})	-5.63384E-4
α_0	0.78987
$i\alpha_b$	0.0081

8.3. MRE based torsional vibration isolation for moving base

The SDoF system for the MRE based torsional vibration isolation is as shown in Figure 8-2, where the moving base represents the core of the electromagnet. The corresponding terms are as tabulated in Table 8.3

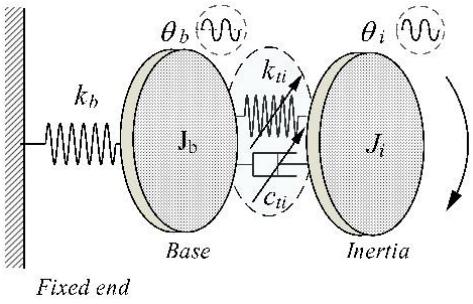

Figure 8-2: MRE based torsional isolator

Table 8.3: Nomenclature of parameters

Nomenclature	Terminologies
J_b	Inertia of the base
$\theta_b, \dot{\theta}_b \ddot{\theta}_b$	Angular Displacement, velocity and acceleration of base
k_{tb}	Torsional Stiffness of the base
k_{ti}	Torsional Stiffness of the isolator
$\theta_i, \dot{\theta}_i \ddot{\theta}_i,$	Angular Displacement, velocity and acceleration of the SDoF system
J_i	Inertia of the SDoF system

8.4. Design of controller

With the system parameters identified, the next step is to design a suitable controller. This is carried out by identifying the acceleration terms of the input and the output, i.e., the base and the inertial component.

8.4.1. The general differential equation of the system with input

The general differential equation for the MRE isolator with a control input is given as,

$$J_b\ddot{\theta}_b + k_{tb}\theta_b + k_{ti}(\theta_b - \theta_i) + c_{ti}\left(\dot{\theta}_b - \dot{\theta}_i\right) = T(t) + u(t) \quad (8.2)$$

$$J_i\ddot{\theta}_i + k_{ti}(\theta_i - \theta_b) + c_{ti}\left(\dot{\theta}_i - \dot{\theta}_b\right) = -u(t) \quad (8.3)$$

Where $T(t)$, $u(t)$ represents the Torque and the current, respectively. From the above, the acceleration term for the base is written as,

$$\ddot{\theta}_b = \frac{T(t)+u(t)-\left(k_{tb}\theta_b+k_{ti}(\theta_b-\theta_i)+c_{ti}\left(\dot{\theta}_b-\dot{\theta}_i\right)\right)}{J_b} \quad (8.4)$$

Similarly, the acceleration term for the inertial component is

$$\ddot{\theta}_i = \frac{-u(t)-\left(k_{ti}(\theta_i-\theta_b)+c_{ti}(\dot{\theta}_\iota-\dot{\theta_b})\right)}{J_i} \tag{8.5}$$

8.4.2. State space equations

The state equation for the system is given as

$$\dot{x} = Ax + Bu \tag{8.6}$$

Where x is the state vector, and $\dot{x}$, defines how the state vector changes as the linear combination of the current state and the inputs, both as a function of time. *A* matrix is called as the state matrix, while the *B* matrix is called the input matrix. The state matrix defines how the input to the system changes the variables while the input matrix explains how the inputs enter into the system.

The corresponding output equation is given as,

$$y = Cx + Du \tag{8.7}$$

Where *y* is the output vector. *C* matrix, also called the output matrix, describes how the states are combined to get the required output. *D* is called the feedthrough matrix. For the current system,

$$[A] = \begin{vmatrix} 0 & 0 & 1 & 0 \\ 0 & 0 & 0 & 1 \\ -\frac{k_{ti}}{J_i} & \frac{k_{ti}}{J_i} & -\frac{c_{ti}}{J_i} & \frac{c_{ti}}{J_i} \\ \frac{k_{ti}}{J_b} & \frac{-(k_{tb}+k_{ti})}{J_b} & \frac{c_{ti}}{J_b} & -\frac{c_{ti}}{J_b} \end{vmatrix}; \qquad [B] = \begin{vmatrix} 0 & 0 \\ 0 & 0 \\ -\frac{1}{J_i} & 0 \\ \frac{1}{J_i} & \frac{1}{J_b} \end{vmatrix}$$

$$[C] = \begin{vmatrix} 1 & 0 & 0 & 0 \\ 0 & 1 & 0 & 0 \\ 0 & 0 & 1 & 0 \\ 0 & 0 & 0 & 1 \end{vmatrix}; \qquad [D] = \begin{vmatrix} 0 & 0 \\ 0 & 0 \\ 0 & 0 \\ 0 & 0 \end{vmatrix}$$

Substituting the above for equations (8.6) and (8.7),

$$\begin{bmatrix} \theta_i \\ \theta_b \\ \dot{\theta}_\iota \\ \dot{\theta_b} \end{bmatrix} = \begin{vmatrix} 0 & 0 & 1 & 0 \\ 0 & 0 & 0 & 1 \\ -\frac{k_{ti}}{J_i} & \frac{k_{ti}}{J_i} & -\frac{c_{ti}}{J_i} & \frac{c_{ti}}{J_i} \\ \frac{k_{ti}}{J_b} & \frac{-(k_{tb}+k_{ti})}{J_b} & \frac{c_{ti}}{J_b} & -\frac{c_{ti}}{J_b} \end{vmatrix} x + \begin{vmatrix} 0 & 0 \\ 0 & 0 \\ -\frac{1}{J_i} & 0 \\ \frac{1}{J_i} & \frac{1}{J_b} \end{vmatrix} u \tag{8.8}$$

$$y = \begin{vmatrix} 1 & 0 & 0 & 0 \\ 0 & 1 & 0 & 0 \\ 0 & 0 & 1 & 0 \\ 0 & 0 & 0 & 1 \end{vmatrix} \theta + \begin{vmatrix} 0 & 0 \\ 0 & 0 \\ 0 & 0 \\ 0 & 0 \end{vmatrix} u \tag{8.9}$$

8.4.3. PID controller

The Proportional Integral Derivative (PID) is one of the widely used generic classical controllers used in vibration reduction strategies. The PID measures the difference between a suitable reference value and the measured output, thereby attempting to reduce the error between the signals.

$$G_c(S) = K_p + \frac{K_i}{S} + K_d S$$

Where the K_p, K_i and K_d represents the proportional, integral and derivative gain, respectively.

The usage of the PID controller lies in generating an actuating signal which enables to track the reference input to reduce the vibration amplitudes. The integral control effectively eliminates the error due to the steady-state response of the system. Similarly, the stability of the system and overshoot of the transient response is improved by the derivative gain of the PID system. In the present study, the current control of the electromagnet is achieved using the PID feedback loop.

$$J_i\ddot{\theta}_i + k_{ti}(\theta_i - \theta_b) + c_{ti}\left(\dot{\theta}_i - \dot{\theta_b}\right) = -u(t)$$

8.4.4. Clipped control algorithm

$$f(i) = i = 5A,\ T_c > T_m,$$

$$i = 0A,\ T_c \leq T_m$$

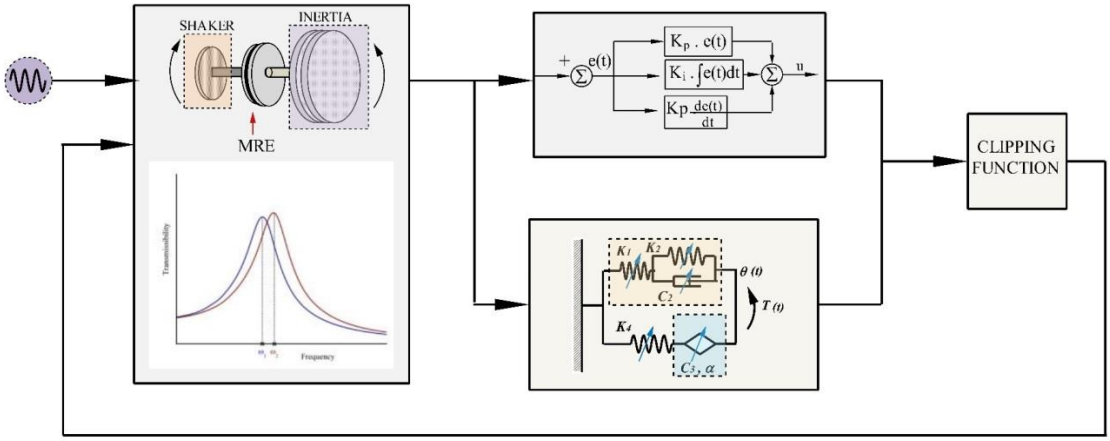

Figure 8-3: Flow-chart of the PID control feedback loop

8.5. Simulation of Single frequency excitations

The simulation of the PID control is carried out in MATLAB Simulink. The analysis is carried out for 20Hz, which is the desired system frequency. For the simulation, the corresponding parameters of the system are Inertia, J_i=0.000825 kg. m^2; Stiffness, k_{ti}=8.96 N.m rad^{-1}; Damping coefficient, c_{ti}=0.019 kg.m^{2}rad^{-1}sec^{-1}; Similarly for the base, the properties are: Inertia, J_b=0.00125 kg. m^2; Stiffness, k_{tb}=26.56 N.m rad^{-1}; Also, the gains of the PID, K_p, K_i and K_d are 4, 0.02, 0.049, respectively. The MATLAB Simulink program for PID control is shown in Figure 8-4.

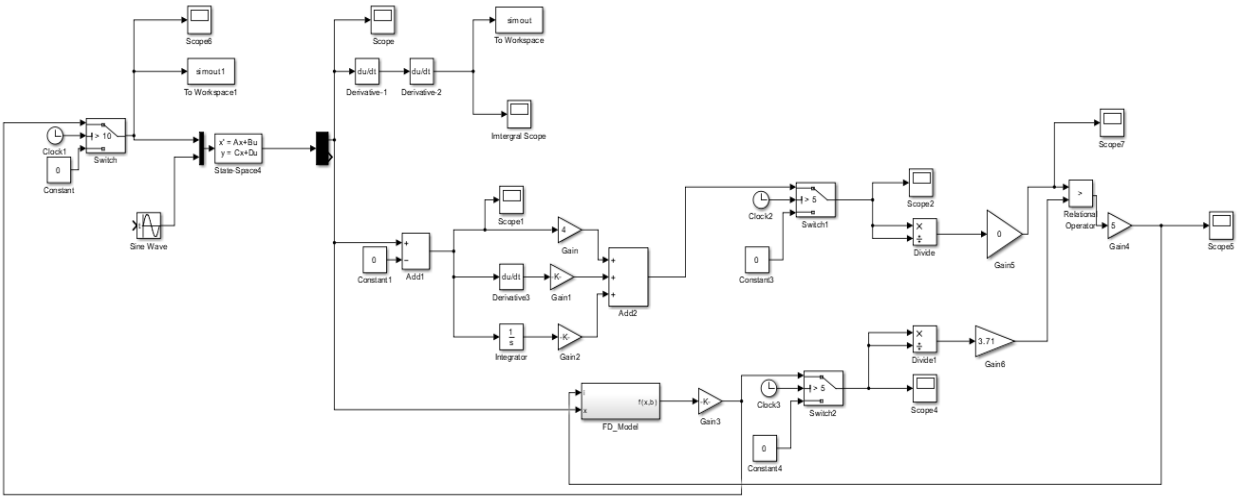

Figure 8-4: MATLAB Simulink program for PID

8.6. Results and Discussions

The simulation results for the PID control is shown in Figure 8-5. The figure shows the simulated time response of the MRE isolator for the frequency response of 20 Hz. As seen, for the first 5 secs, the system is excited at a constant frequency of 20Hz, keeping the controller in the OFF conditions. Under this condition, the displacement amplitude of the system is 0.016 rad. For the 15 seconds, the system is excited with the PID control switched ON, and the computed displacement value is 0.013 rad. The total reduction in the amplitudes corresponds to 18.76%. Figure 8-5 (b) shows the required control force to the MRE isolator.

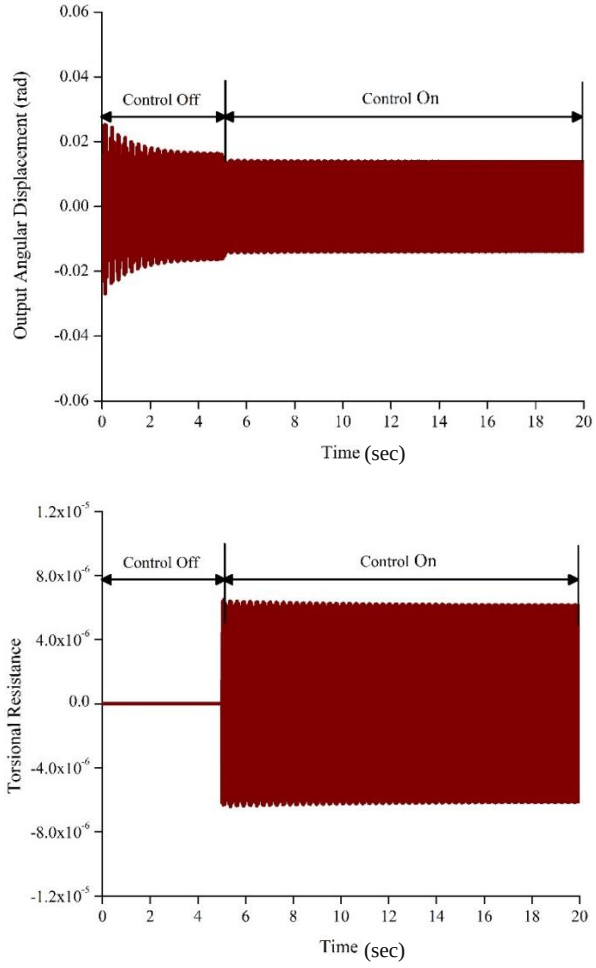

Figure 8-5: PID Simulation for 20 Hz

8.7. Summary

The present chapter discusses the implementation of a Model-based control strategy based on the classical PID control. The field-dependent function equations are extracted from the parameters of the parametric model. This is followed by the design of the controller, where the state space equations are derived. With the implementation of the PID control theory, a MATLAB simulation is carried out for Single-frequency excitation at the 20 Hz. Results highlight a reduction of 18.76% of the output displacement amplitudes.

9. Summary and Conclusions

9.1. Summary

Vibration isolation using a passive isolator offers its advantages; however, an inherent drawback of non-adaptability of the isolator to changes in the operating frequencies limits the usage. These are effectively addressed with the use of semi-active vibration isolators. They use smart materials such as Magnetorheological Elastomer, which change their properties under the effect of external forces. Implementation of a Magnetorheological Elastomer based torsional vibration isolator requires a thorough understanding of its rheological properties under the influence of operating parameters such as applied field, operating frequency and input angular displacement. However, the literature confirms the absence of an experimental method to substantiate and evaluate the effects of torsional loads on the viscoelastic parameters. The properties of the MRE isolator vary with the loading conditions and hence, interconversion of these properties between different loading conditions is impractical. Therefore, the first objective in the present study is to develop an experimental setup to estimate the performance of the MRE isolator under torsional loading conditions.

To evaluate the viscoelastic properties of the MRE isolator under torsional loading conditions, the setup is built based on the ISO 10846-2 standard, also known as the blocked transfer stiffness method. One end of the specimen is rigidly fixed and the other end is subjected to a known angular displacement. The Lissajous curves are obtained from the input angular displacement and the output torque. From the plots, the variations in the complex stiffness and loss factor are assessed.

The applied magnetic field is varied between 0T to 0.28T, under an operating frequency of 10Hz to 30Hz. Field-dependent variations in the torsional stiffness of the MRE are studied by considering the interaction energy between the dipoles. Furthermore, the mechanical strain on the dipole is analyzed using the Magneto-static and structural based numerical simulations using ANSYS 19.1. Also, experimental results highlight the stronger influence of the field on the torsional stiffness in comparison with the frequency. The characterization study also indicates the predominant behavior of the angular displacement on the rheological properties of the MRE. The angular displacement is varied within the range of 0.002 rad to 0.016 rad.

To comprehend the effect of the angular displacement, the well established bound rubber theory is used. It is also observed that the damping capacity of the MRE is dependent on the angular displacement and the dissipation capacity of the elastomer is evaluated in terms of loss factor.

To create a constitute relationship between the operating parameters, a viscoelastic based parametric model is derived. The derived model is based on the Poynting-Thomson model to which a fractional element is added. This accurately predicts the properties for the given range of parameters. It consists of six parameters which are obtained by minimizing the error between the experimentally obtained results and the modeled results. The present study is carried out for five levels of input frequency, five levels of angular displacement & six levels of magnetic field corresponding to 150 sets of experimental data. The comparison between the values suggests that the derived model accurately encompasses the effect of field, frequency and the displacement dependency of the MRE isolator.

With the viscoelastic properties of the MRE isolator established and the constitutive relationship derived, the latter part of the present study deals with the understanding and implementation of a Magnetorheological Elastomer based isolator for the torsional vibration isolation. The isolation study is carried out using a custom made torsional SDoF system. The angular displacement is measured using the Serial Arrangement of the Accelerometer (SAA) technique, which enhances the torsional modes of the system. To evaluate its performance, the transmissibility ratio of the SDoF system is assessed for varying input fields. Also, the field-induced shift in the natural frequency is observed. Furthermore, the system is studied for various inertia, field and angular displacement. Following this, an evaluation of the system parameters of the torsional system is carried out.

To further comprehend the semi-active vibration isolation of the MRE isolator, a model based PID is adapted. The fractional-derivative based Poynting-Thomson model is implemented in the PID control logic with the use of the clipping function.

9.2. Conclusions

The dynamic viscoelastic properties of MRE under torsion are sensitive to changes observed in the magnetic field and input frequency. This is evident from the results obtained from the Torque-displacement hysteresis curves. Results indicate that the magnetic field dependence is stronger compared to the frequency-dependent characteristics. The field-sensitive characteristics expressed by the absolute MR effect increased by 8.87%. Compared to the rheometric studies, the field-induced enhancements are lower as the thickness of MRE plays a prominent role. With increase in the sample thickness, intensity of the magnetic field for a fixed sample-pole distance is affected and the increase in the torsional stiffness of the MRE is reduced. The cumulative contributions from the geometry and the magnetic field define the overall property enhancements of MRE. Numerical simulations were carried out which indicate the same. It is also to be noted that the field sensitive properties could be enhanced by a stronger magnetic field, which could create an increased interaction between the fillers embedded in the matrix. The ferromagnetic fillers inside the matrix diminish the frequency-dependent characteristics of MRE and the present MRE sample could show a maximum enhancement of 5.59% stiffness for the frequency variation from 10Hz to 30Hz. Variations in the loss factor suggest the dominance of the field-induced changes in the imaginary part of the complex stiffness, which explains its variations with the magnetic field.

The obtained angular-displacement results showcase the effectiveness of the novel method in capturing the dynamic properties of the MRE under torsional shear. The angular displacement-dependent variations demonstrate a reduction in the measured values of the dynamic torsional stiffness. The variations in the values are effectively explained by adapting the bound rubber theory. In the presence of the magnetic field, however, the displacement dependent decrease in the dynamic torsional stiffness reduced from 9.96% to 8.02%, which emphasized the existence of field-induced dipoles. Furthermore, the MR effect calculated across different angular displacements revealed the field-induced increase in the dynamic torsional stiffness. The frequency induced variations in the MRE highlighted the attributes of the filled rubber. Besides, variations in the damping capacity of the MRE are assessed in terms of the loss factor. From the observed values, it is concluded that the interfacial damping

played a dominant role and the loss factor increased with the increase in the angular displacement to as high as 18.62%. Moreover, the results further suggest the reduced influence of the magnetic field on the variations in the loss factor. Finally, the obtained results suggest that the torsional properties of MRE vary similarly to that of lateral shear.

The hysteresis plots of the isolator reveal that the modeled data accurately fits with the experimental plots for all the parameters of the field, frequency and the angular displacement. Furthermore, it is also evident that the complex stiffness and the real part are more accurately predicted with the accuracy rate of more than 95% and 96%, respectively. However, it is seen that the predicted K''values are not as accurate and differ with the accuracy as low as 90.7%. This reduced accuracy, however, is ascribed to the fluctuations of the K'' in the experimental data and not of the derived model itself.

The effectiveness of the MRE in isolating the torsional vibrations is assessed by the transmissibility plots for varying magnetic fields. The plots indicate the field-induced increase in the torsional natural frequency. This is attributed to the increase in the torsional stiffness in the presence of the field. The shift in the frequency results in the reduction in the transmissibility ratios implying the isolation of the SDoF system. Similar results are observed for the various inertia, angular displacement and magnetic fields. Overall, an isolation effect as high as 42% is observed for the present MRE isolator. Further, varying inertia and angular displacement also influence the isolation capabilities of the MRE isolator, which further ascertains the results obtained from the characterization process. It is also observed that the trends in the damping ratio are inconsistent, which signifies that the damping effect in the MRE under torsional shear varied similarly as that of the inconsistencies in the linear shear, as reported by literature. The system parameters such as the stiffness and the damping ratio of the SDoF system is further calculated.

From the simulation, it is observed that the PID control strategy is effective in the reduction of the amplitudes of the system. With the control strategy in place, the MRE isolator reduces the output displacement of the system by 18.76%.

9.3. Scope for further work

The present work presented a study on the experimental investigation of the Magnetorheological Elastomer based Torsional vibration isolation system. Initial studies revolved around the characterization of the MRE isolator for varying operating parameters. Apart from the frequency of operation, angular displacement and the field, other parameters such as operating temperature could be explored. Temperature plays an important aspect since the behavior of the viscoelastic based MRE transits between phases in the presence of high temperatures.

It was also observed that the field-induced variations for the present isolator resulted in a reduced MR effect. This can be further explored and improved with the addition of additives such as CNT into the base MRE. Also, studies on the MRE isolator with anisotropic behavior could be focused, though dedicated equipment for imparting sustained magnetic field at higher field strength is required for such studies.

The angular displacement for the preset study was restricted to the Linear Viscoelastic (LVE) limit, which made sure that the MRE was within the linear region of its operating conditions. This was done based on the assumption that the angular displacement would be less for lower inertial forces on rotating members. Further analysis could be effectively carried out for larger inertial forces. Though, it becomes quite essential that the parametric modeling techniques are modified to accommodate the non-linear behavior of the MRE isolator.

The derived parametric model was highly efficient in forming the constitutive relations between the parameters. However, this was restricted to understand the behavior of the operating parameters of the MRE isolator. The approach can be extended further and implemented to the SDoF system, which helps in better comprehension of the system.

Apart from the above, the other aspect on which further research could be carried out is the design aspect of the MRE isolator. In the present study, the loading conditions on the isolator is torsional shear. An alternate approach would be designing the MRE isolator to work in compression mode. The important aspect here is to study the effects of the magnetic fields on the MRE. Based on the study, further

improvements in the electromagnet design could be incorporated to suit the parallel direction of the field.

In the present study, a PID based controller was designed with incorporating the derived parametric model. However, the actual implementation of the PID on a real-time basis was not studied. Further studies could involve the real-time implementation of various types of controllers ranging from model based to model-less strategies.

References

Agirre-Olabide, I., Berasategui, J., Elejabarrieta, M. J., and Bou-Ali, M. M. (2014a). "Characterization of the linear viscoelastic region of magnetorheological elastomers." *J. Intell. Mater. Syst. Struct.*, 25(16), 2074–2081.

Agirre-Olabide, I., Berasategui, J., Elejabarrieta, M. J., and Bou-Ali, M. M. (2014b). "Characterization of the linear viscoelastic region of magnetorheological elastomers." *J. Intell. Mater. Syst. Struct.*

Agirre-Olabide, I., and Elejabarrieta, M. J. (2017). "Effect of synthesis variables on viscoelastic properties of elastomers filled with carbonyl iron powder." *J. Polym. Res.*, 24(9).

Agirre-Olabide, I., and Elejabarrieta, M. J. (2018). "A new magneto-dynamic compression technique for magnetorheological elastomers at high frequencies." *Polym. Test.*, 66(January), 114–121.

Agirre-Olabide, I., Kuzhir, P., and Elejabarrieta, M. J. (2018). "Linear magneto-viscoelastic model based on magnetic permeability components for anisotropic magnetorheological elastomers." *J. Magn. Magn. Mater.*, 446, 155–161.

Ahmad Khairi, M. H., Mazlan, S. A., Ubaidillah, Ku Ahmad, K. Z., Choi, S. B., Abdul Aziz, S. A., and Yunus, N. A. (2017). "The field-dependent complex modulus of magnetorheological elastomers consisting of sucrose acetate isobutyrate ester." *J. Intell. Mater. Syst. Struct.*, 28(14), 1993–2004.

Bastola, A. K., and Li, L. (2018). "A new type of vibration isolator based on magnetorheological elastomer." *Mater. Des.*, 157, 431–436.

Bastola, A. K., Paudel, M., and Li, L. (2020). "Dot-patterned hybrid magnetorheological elastomer developed by 3D printing." *J. Magn. Magn. Mater.*, 494(May 2019).

Bazinenkov, A. M., and Mikhailov, V. P. (2015). "Active and Semi Active Vibration Isolation Systems Based on Magnetorheological Materials." *Procedia Eng.*, 170–174.

Behrooz, M., Wang, X., and Gordaninejad, F. (2014a). "Modeling of a new semi-active/passive magnetorheological elastomer isolator." *Smart Mater. Struct.*, 23(4).

Behrooz, M., Wang, X., and Gordaninejad, F. (2014b). “Performance of a new magnetorheological elastomer isolation system.” *Smart Mater. Struct.*, 23(4).

Bell, R. C., Zimmerman, D. T., and Wereley, N. M. (2010). “Impact of Nanowires on the Properties of Magnetorheological Fluids and Elastomer Composites.” (February).

Bellelli, A., and Spaggiari, A. (2019). “Magneto-mechanical characterization of magnetorheological elastomers.” *J. Intell. Mater. Syst. Struct.*, 1–10.

Bica, I., Anitas, E. M., Bunoiu, M., Vatzulik, B., and Juganaru, I. (2014). “Hybrid magnetorheological elastomer: Influence of magnetic field and compression pressure on its electrical conductivity.” *J. Ind. Eng. Chem.*

Bodelot, L., Voropaieff, J. P., and Pössinger, T. (2018). “Experimental investigation of the coupled magneto-mechanical response in magnetorheological elastomers.” *Exp. Mech.*, 58(2), 207–221.

Borin, D., Kolsch, N., Stepanov, G., and Odenbach, S. (2018). “On the oscillating shear rheometry of magnetorheological elastomers.” *Rheol. Acta*, 57(3), 217–227.

Borin, D. Y., and Stepanov, G. V. (2015). “Elastomer with magneto- and electrorheological properties.” *J. Intell. Mater. Syst. Struct.*, 1893–1898.

Brown, R. (2006). *Physical testing of rubber*. *Phys. Test. Rubber*.

Carlson, J. D., and Jolly, M. R. (2000). “MR fluid, foam and elastomer devices.” *Mechatronics*, 10(4), 555–569.

Chandra, R., Singh, S. P., and Gupta, K. (1999). “Damping studies in fiber-reinforced composites - a review.” *Compos. Struct.*, 46(1), 41–51.

Chen, D., Yu, M., Zhu, M., Qi, S., and Fu, J. (2016). “Carbonyl iron powder surface modification of magnetorheological elastomers for vibration absorbing application.” *Smart Mater. Struct.*, 25(11).

Chen, L., and Gong, X. L. (2008). “Damping of magnetorheological elastomers.” *J. Cent. South Univ. Technol. (English Ed.)*, 15(1 SUPPL.), 271–274.

Chen, L., Gong, X. L., Jiang, W. Q., Yao, J. J., Deng, H. X., and Li, W. H. (2007). “Investigation on magnetorheological elastomers based on natural rubber.” *J. Mater.*

Sci., 42(14), 5483–5489.

Chen, L., Gong, X. L., and Li, W. H. (2008a). "Effect of carbon black on the mechanical performances of magnetorheological elastomers." *Polym. Test.*, 27(3), 340–345.

Chen, L., Gong, X. L., and Li, W. H. (2008b). "Damping of magnetorheological elastomers." *Chinese J. Chem. Phys.*, 21(6).

Chertovich, A. V., Stepanov, G. V., Kramarenko, E. Y., and Khokhlov, A. R. (2010). "New composite elastomers with giant magnetic response." *Macromol. Mater. Eng.*, 295(4), 336–341.

Deng, L., Zhang, J., and Xiang, L. (2018). "Design Torsional Vibration Damper of Engine based on Classical Optimal Approach." *IOP Conf. Ser. Mater. Sci. Eng.*, 452(2).

Dong, X. M., Yu, M., Liao, C. R., and Chen, W. M. (2009). "A new variable stiffness absorber based on magneto-rheological elastomer." *Trans. Nonferrous Met. Soc. China (English Ed.*

Eem, S. H., Jung, H. J., and Koo, J. H. (2012). "Modeling of magneto-rheological elastomers for harmonic shear deformation." *IEEE Trans. Magn.*

Fan, Y. C., Gong, X. L., Jiang, W. Q., Zhang, W., Wei, B., and Li, W. H. (2010). "Effect of maleic anhydride on the damping property of magnetorheological elastomers." *Smart Mater. Struct.*, 19(5).

Fu, J., Li, P., Wang, Y., Liao, G., and Yu, M. (2016). "Model-free fuzzy control of a magnetorheological elastomer vibration isolation system : analysis and experimental evaluation." 25.

Gamota, D. R., and Filisko, F. E. (1991). "Dynamic mechanical studies of electrorheological materials: Moderate frequencies." *J. Rheol. (N. Y. N. Y).*, 35(3), 399–425.

Gao, P., Xiang, C., Liu, H., and Zhou, H. (2018). "Reducing variable frequency vibrations in a powertrain system with an adaptive tuned vibration absorber group." *J. Sound Vib.*, 425, 82–101.

Garcia Tarrago, M. J. (2006). “Engineering rubber bushing stiffness formulas including dynamic amplitude dependence.” *Eng. Sci.*

Ge, L., Gong, X., Fan, Y., and Xuan, S. (2013). “Preparation and mechanical properties of the magnetorheological elastomer based on natural rubber/rosin glycerin hybrid matrix.” *Smart Mater. Struct.*, 22(11).

Gent, A. N. (2012). “Preface - Engineering with Rubber: How to Design Rubber Components.” *Eng. with Rubber How to Des. Rubber Components*, 434.

Ginder, J. M. (2001). “Magnetorheological elastomers in tunable vibration absorbers.” *Proc. SPIE*, 4331, 103–110.

Ginder, J. M., Clark, S. M., Schlotter, W. F., and Nichols, M. E. (2002). “Magnetostrictive phenomena in magnetorheological elastomers.” *Int. J. Mod. Phys. B*, 2412–2418.

Ginder, J. M., Nichols, M. E., Elie, L. D., and Clark, S. M. (2000). “Controllable-stiffness components based on magnetorheological elastomers.” *Smart Struct. Mater. 2000 Smart Struct. Integr. Syst.*, 3985, 418.

Gong, X., Fan, Y., Xuan, S., Xu, Y., and Peng, C. (2012). “Control of the damping properties of magnetorheological elastomers by using polycaprolactone as a temperature-controlling component.” *Ind. Eng. Chem. Res.*, 51(18), 6395–6403.

Gong, X. L., Zhang, X. Z., and Zhang, P. Q. (2005). “Fabrication and characterization of isotropic magnetorheological elastomers.” *Polym. Test.*, 24(5), 669–676.

Gu, X., Li, J., Li, Y., and Askari, M. (2015). “Frequency control of smart base isolation system employing a novel adaptive magneto-rheological elastomer base isolator.” *J. Intell. Mater. Syst. Struct.*, 849–858.

Guo, C. Y., Gong, X. L., Xuan, S. H., Zhang, Y. L., and Jiang, W. Q. (2012). “An experimental investigation on the normal force behavior of magnetorheological suspensions.” *Korea Aust. Rheol. J.*, 24(3), 171–180.

Haddow, A., and Shaw, S. (2003). “Centrifugal Pendulum Vibration Absorbers: An Experimental and Theoretical Investigation.” *Nonlinear Dyn.*, 34, 293–307.

Hashi, H. A., Muthalif, A. G. A., and Diyana Nordin, N. H. (2016). “Dynamic tuning

of torsional transmissibility using magnetorheological elastomer: Modelling and experimental verification." *Iran. J. Sci. Technol. - Trans. Mech. Eng.*, 40(3), 181–187.

Hegde, S., Kiran, K., and Gangadharan, K. V. (2015). "A novel approach to investigate effect of magnetic field on dynamic properties of natural rubber based isotropic thick magnetorheological elastomers in shear mode." *J. Cent. South Univ.*, 22(7), 2612–2619.

Hegde, S., Poojary, U. R., and Gangadharan, K. V. (2014). "Experimental Investigation of Effect of Ingredient Particle Size on Dynamic Damping of RTV Silicone Base Magnetorheological Elastomers." *Procedia Mater. Sci.*, 5, 2301–2309.

Hoang, N., Zhang, N., and Du, H. (2011). "An adaptive tunable vibration absorber using a new magnetorheological elastomer for vehicular powertrain transient vibration reduction." *Smart Mater. Struct.*, 20(1).

Hoang, N., Zhang, N., Li, W. H., and Du, H. (2013). "Development of a torsional dynamic absorber using a magnetorheological elastomer for vibration reduction of a powertrain test rig." *J. Intell. Mater. Syst. Struct.*, 24(16), 2036–2044.

International Organization for Standardization. (2002). *Acoustics and vibration — Laboratory measurement of vibro-acoustic transfer properties of resilient elements — Part 2: Direct method for determination of the dynamic stiffness of resilient supports for translatory motion*. *Communication*.

Iso, B. S. E. N. (2009). "Acoustics and vibration — measurement of vibro- acoustic transfer properties of resilient elements." 3(1).

Johnson, N., Gordaninejad, F., and Wang, X. (2018). "Dynamic behavior of thick magnetorheological elastomers." *J. Intell. Mater. Syst. Struct.*, 29(2), 183–193.

Jolly, M. R., Carlson, J. D., and Muñoz, B. C. (1996a). "A model of the behaviour of magnetorheological materials." *Smart Mater. Struct.*, 5(5), 607–614.

Jolly, M. R., Carlson, J. D., Muñoz, B. C., and Bullions, T. A. (1996b). "The magnetoviscoelastic response of elastomer composites consisting of ferrous particles embedded in a polymer matrix." *J. Intell. Mater. Syst. Struct.*, 7(6), 613–622.

Ju, B. X., Yu, M., Fu, J., Yang, Q., Liu, X. Q., and Zheng, X. (2012a). "A novel

porous magnetorheological elastomer: Preparation and evaluation." *Smart Mater. Struct.*, 21(3).

Ju, B. X., Yu, M., Fu, J., Yang, Q., Liu, X. Q., and Zheng, X. (2012b). "A novel porous magnetorheological elastomer: Preparation and evaluation." *Smart Mater. Struct.*, 21(3).

Jung, H. J., Eem, S. H., Jang, D. D., and Koo, J. H. (2011). "Seismic performance analysis of a smart base-isolation system considering dynamics of MR elastomers." *J. Intell. Mater. Syst. Struct.*, 22(13), 1439–1450.

Kaleta, J., Lewandowski, D., and Zitek, G. (2007). "Inelastic properties of magnetorheological composites: II. Model, identification of parameters." *Smart Mater. Struct.*, 16(5), 1954–1960.

Kallio, M. (2005). *The elastic and damping properties of magnetorheological elastomers*. *VTT Publ.*

Khimi, S. R., and Pickering, K. L. (2015). "Comparison of dynamic properties of magnetorheological elastomers with existing antivibration rubbers." *Compos. Part B Eng.*, 83, 175–183.

Kuang, J.-H. (1994). "ACCELEROMETER PAIR MEASUREMENTS FOR SHAFT DYNAMIC PARAMETERS ANALYSIS." *Proc. SPIE - Int. Soc. Opt. Eng.*

Kumar, V., and Lee, D. J. (2017). "Iron particle and anisotropic effects on mechanical properties of magneto-sensitive elastomers." *J. Magn. Magn. Mater.*, 441, 105–112.

Kumar, V., and Lee, D. J. (2019). "Mechanical properties and magnetic effect of new magneto-rheological elastomers filled with multi-wall carbon nanotubes and iron particles." *J. Magn. Magn. Mater.*, 482(September 2018), 329–335.

Ladouce-Stelandre, L., Bomal, Y., Flandin, L., and Labarre, D. (2003). "Dynamic Mechanical Properties of Precipitated Silica Filled Rubber: Influence of Morphology and Coupling Agent." *Rubber Chem. Technol.*, 76(1), 145–159.

Lakes, R. (2009). *Viscoelastic materials*. *Viscoelastic Mater.*

Leblanc, J. L. (2002). "Rubber-filler interactions and rheological properties in filled compounds." *Prog. Polym. Sci.*, 27(4), 627–687.

Lee, C. W., and Kim, I. (2018). “Fabrication and Characterization of Natural Rubber-Based Magnetorheological Elastomers at Large Strain for Base Isolators.” 2018.

Lee, K. H., Park, J. E., and Kim, Y. K. (2019). “Design of a stiffness variable flexible coupling using magnetorheological elastomer for torsional vibration reduction.” *J. Intell. Mater. Syst. Struct.*, 30(15), 2212–2221.

Leng, D., Wu, T., Liu, G., Wang, X., and Sun, L. (2018). “Tunable isolator based on magnetorheological elastomer in coupling shear–squeeze mixed mode.” *J. Intell. Mater. Syst. Struct.*, 29(10), 2236–2248.

Lerner, A. A., and Cunefare, K. A. (2008). “Performance of MRE-based vibration absorbers.” *J. Intell. Mater. Syst. Struct.*, 19(5), 551–563.

Li, J. F., and Gong, X. L. (2008a). “Dynamic damping property of magnetorheological elastomer.” *J. Cent. South Univ. Technol. (English Ed.*, 15(1 SUPPL.), 261–265.

Li, J. F., and Gong, X. L. (2008b). “Dynamic damping property of magnetorheological elastomer.” *J. Cent. South Univ. Technol. (English Ed.*

Li, W. H., Zhou, Y., and Tian, T. F. (2010). “Viscoelastic properties of MR elastomers under harmonic loading.” *Rheol. Acta*, 49(7), 733–740.

Li, W., Qiao, X., Lu, X., Chen, J., Gong, X., Yang, T., Sun, K., Chen, X., and Li, W. (2012a). “Microstructure and magnetorheological properties of the thermoplastic magnetorheological elastomer composites containing modified carbonyl iron particles and poly(styrene-b-ethylene-ethylenepropylene-b-styrene) matrix.” *Smart Mater. Struct.*

Li, W., Qiao, X., Lu, X., Chen, J., Gong, X., Yang, T., Sun, K., Chen, X., and Li, W. (2012b). “Microstructure and magnetorheological properties of the thermoplastic magnetorheological elastomer composites containing modified carbonyl iron particles and poly(styrene-b-ethylene-ethylenepropylene-b-styrene) matrix.” *Smart Mater. Struct.*, 21(11).

Li, W., Qiao, X., Lu, X., Chen, J., Gong, X., Yang, T., Sun, K., Chen, X., and Li, W. (2012c). “Microstructure and magnetorheological properties of the thermoplastic

magnetorheological elastomer composites containing modified carbonyl iron particles and poly(styrene-b-ethylene-ethylenepropylene-b-styrene) matrix." *Smart Mater. Struct.*, 21(11).

Li, W., Zhang, X., and Du, H. (2012d). "Development and simulation evaluation of a magnetorheological elastomer isolator for seat vibration control." *J. Intell. Mater. Syst. Struct.*, 1041–1048.

Li, Y., Li, J., Li, W., and Du, H. (2014). "A state-of-the-art review on magnetorheological elastomer devices." *Smart Mater. Struct.*, 24(12).

Li, Y., Li, J., Li, W., and Samali, B. (2013). "Development and characterization of a magnetorheological elastomer based adaptive seismic isolator." *Smart Mater. Struct.*, 22(3).

Liao, G., Gong, X., and Xuan, S. (2013). "Magnetic field-induced compressive property of magnetorheological elastomer under high strain rate." *Ind. Eng. Chem. Res.*, 52(25), 8445–8453.

Liao, G. J., Gong, X. L., Xuan, S. H., Kang, C. J., and Zong, L. H. (2012). "Development of a real-time tunable stiffness and damping vibration isolator based on magnetorheological elastomer." *J. Intell. Mater. Syst. Struct.*, 23(1), 25–33.

Lin, T. R., Farag, N. H., and Pan, J. (2005). "Evaluation of frequency dependent rubber mount stiffness and damping by impact test." *Appl. Acoust.*, 66(7), 829–844.

Lokander, M., and Stenberg, B. (2003a). "Performance of isotropic magnetorheological rubber materials." *Polym. Test.*, 22, 245–251.

Lokander, M., and Stenberg, B. (2003b). "Improving the magnetorheological effect in isotropic magnetorheological rubber materials." *Polym. Test.*, 22(6), 677–680.

Lu, H., Wang, W., Yang, F., Wang, G., and Rui, X. (2018). "Effect of carbon black with large particle size on dynamic mechanical analysis of magnetorheological elastomers (MREs)." *Mater. Res. Express*, 5(9).

Lu, X., Qiao, X., Watanabe, H., Gong, X., Yang, T., Li, W., Sun, K., Li, M., Yang, K., Xie, H., Yin, Q., Wang, D., and Chen, X. (2012). "Mechanical and structural investigation of isotropic and anisotropic thermoplastic magnetorheological elastomer

composites based on poly(styrene-b-ethylene-co-butylene-b-styrene) (SEBS).” *Rheol. Acta*, 51(1), 37–50.

Nadeau, S., and Champoux, Y. (2000). “Application of the direct complex stiffness method to engine mounts.” *Exp. Tech.*, 24(3), 21–23.

Nam, T. H., Petríková, I., and Marvalová, B. (2020). “Experimental characterization and viscoelastic modeling of isotropic and anisotropic magnetorheological elastomers.” *Polym. Test.*, 81(December 2019).

Nayak, B., Dwivedy, S. K., and Murthy, K. S. R. K. (2015). “Fabrication and characterization of magnetorheological elastomer with carbon black.” *J. Intell. Mater. Syst. Struct.*, 26(7), 830–839.

Ni, Y. Q., Ying, Z. G., and Chen, Z. H. (2010). “Magneto-rheological elastomer (MRE) based composite structures for micro-vibration control.” *Earthq. Eng. Eng. Vib.*, 9(3), 345–356.

Ni, Z. C., Gong, X. L., Li, J. F., and Chen, L. (2009). “Study on a dynamic stiffness-tuning absorber with squeeze-strain enhanced magnetorheological elastomer.” *J. Intell. Mater. Syst. Struct.*, 20(10), 1195–1202.

Norouzi, M., Sajjadi Alehashem, S. M., Vatandoost, H., Ni, Y. Q., and Shahmardan, M. M. (2015). “A new approach for modeling of magnetorheological elastomers.” *J. Intell. Mater. Syst. Struct.*, 27(8), 1121–1135.

Ooi, L. E., and Ripin, Z. M. (2011). “Dynamic stiffness and loss factor measurement of engine rubber mount by impact test.” *Mater. Des.*, 32(4), 1880–1887.

Opie, S., and Yim, W. (2011). “Design and control of a real-time variable modulus vibration isolator.” *J. Intell. Mater. Syst. Struct.*, 22(2), 113–125.

Padalka, O., Song, H. J., Wereley, N. M., Filer, J. A., and Bell, R. C. (2010). “Stiffness and damping in Fe, Co, and Ni nanowire-based magnetorheological elastomeric composites.” *IEEE Trans. Magn.*, 2275–2277.

Palacios-Pineda, L. M., Perales-Martinez, I. A., Lozano-Sanchez, L. M., Martínez-Romero, O., Puente-Córdova, J., Segura-Cárdenas, E., and Elías-Zúñiga, A. (2017). “Experimental investigation of the magnetorheological behavior of PDMS elastomer

reinforced with iron micro/nanoparticles." *Polymers (Basel).*, 9(12).

Payne, A. R. R. (1962). "The dynamic properties of carbon black loaded natural rubber vulcanizates. Part II." *J. Appl. Polym. Sci.*, 6(21), 368–372.

Payne, A. R., and Whittaker, R. E. (1970). "Reinforcement of rubber with carbon black." *Composites*, 1(4), 203–214.

Pickering, K. L., Raa Khimi, S., and Ilanko, S. (2015). "The effect of silane coupling agent on iron sand for use in magnetorheological elastomers Part 1: Surface chemical modification and characterization." *Compos. Part A Appl. Sci. Manuf.*, 68, 377–386.

Poojary, U. R., and Gangadharan, K. V. (2016). "Experimental investigation on the effect of magnetic field on strain dependent dynamic stiffness of magnetorheological elastomer." *Rheol. Acta*, 55(11–12), 993–1001.

Poojary, U. R., and Gangadharan, K. V. (2017). "Magnetic field and frequency dependent LVE limit characterization of magnetorheological elastomer." *J. Brazilian Soc. Mech. Sci. Eng.*, 39(4), 1365–1373.

Poojary, U. R., and Gangadharan, K. V. (2018). "Integer and fractional order-based viscoelastic constitutive modeling to predict the frequency and magnetic field-induced properties of magnetorheological elastomer." *J. Vib. Acoust. Trans. ASME*, 140(4).

Poojary, U. R., Hegde, S., and Gangadharan, K. V. (2016). "Dynamic blocked transfer stiffness method of characterizing the magnetic field and frequency dependent dynamic viscoelastic properties of MRE." *Korea Aust. Rheol. J.*, 28(4), 301–313.

Poojary, U. R., Hegde, S., and Gangadharan, K. V. (2017). "Dynamic deformation–dependent magnetic field–induced force transmissibility characteristics of magnetorheological elastomer." *J. Intell. Mater. Syst. Struct.*, 28(11), 1491–1500.

Poojary, U. R., Hegde, S., and Gangadharan, K. V. (2018). "Experimental investigation on the effect of carbon nanotube additive on the field-induced viscoelastic properties of magnetorheological elastomer Composites." *J Mater Sci*, 53, 4229–4241.

Popp, K. M., Li, W., Zhang, X. Z., and Kosasih, P. B. (2010). "MRE properties under

shear and squeeze modes and applications.” *J. Intell. Mater. Syst. Struct.*, 1471–1477.

Rabinow, J. (1948). “The Magnetic Fluid Clutch.” *Trans. Am. Inst. Electr. Eng.*, 67(December), 1308–1315.

Ramorino, G., Vetturi, D., Cambiaghi, D., Pegoretti, A., and Ricco, T. (2003). “Developments in dynamic testing of rubber compounds: Assessment of non-linear effects.” *Polym. Test.*, 22(6), 681–687.

Ran, L., Yacamini, R., and Smith, K. S. (1996). *Torsional Vibrations in Electrical Induction Motor Drives During Start-up*. *J. Vib. Acoust.*

Rao, S. S. (2010). *Mechanical Vibrations*. *Recherche*.

Rigbi, Z., and Jilkén, L. (1983). “The response of an elastomer filled with soft ferrite to mechanical and magnetic influences.” *J. Magn. Magn. Mater.*, 37(3), 267–276.

Shen, Y., Golnaraghi, M. F., and Heppler, G. R. (2004). “Experimental research and modeling of magnetorheological elastomers.” *J. Intell. Mater. Syst. Struct.*, 15(1), 27–35.

Song, H. J., Wereley, N. M., Bell, R. C., Planinsek, J. L., and Filer, J. A. (2009). “Field dependent response of magnetorheological elastomers utilizing spherical Fe particles versus Fe nanowires.” *J. Phys. Conf. Ser.*, 149, 012097.

Stacer, R. G., Hubner, C., and Husband, D. M. (1990). “Binder/filler interaction and the nonlinear behavior of highly-filled elastomers.” *Rubber Chem. Technol.*, 63(4), 488–502.

Sternstein, S. S. (1983). “Transient and Dynamic Characterization of Viscoelastic Solids.” *Polym. Charact.*, Advances in Chemistry, AMERICAN CHEMICAL SOCIETY, 123-147 SE–7.

Sun, S., Deng, H., Yang, J., Li, W., Du, H., and Alici, G. (2015a). “Performance evaluation and comparison of magnetorheological elastomer absorbers working in shear and squeeze modes.” *J. Intell. Mater. Syst. Struct.*, 1757–1763.

Sun, S., Deng, H., Yang, J., Li, W., Du, H., Alici, G., and Nakano, M. (2015b). “An adaptive tuned vibration absorber based on multilayered MR elastomers.” *Smart Mater. Struct.*, 24(4), 45045.

Tian, T. F., Li, W. H., Alici, G., Du, H., and Deng, Y. M. (2011a). “Microstructure and magnetorheology of graphite-based MR elastomers.” *Rheol. Acta*.

Tian, T. F., Li, W. H., Alici, G., Du, H., and Deng, Y. M. (2011b). “Microstructure and magnetorheology of graphite-based MR elastomers.” *Rheol. Acta*, 50(9–10), 825–836.

Ubaidillah, Sutrisno, J., Purwanto, A., and Mazlan, S. A. (2015). “Recent progress on magnetorheological solids: Materials, fabrication, testing, and applications.” *Adv. Eng. Mater.*, 17(5), 563–597.

Vatandoost, H., Hemmatian, M., Sedaghati, R., and Rakheja, S. (2019). “Dynamic characterization of isotropic and anisotropic magnetorheological elastomers in the oscillatory squeeze mode superimposed on large static pre-strain.” *Compos. Part B Eng.*, 182(November 2019), 107648.

Vatandoost, H., Hemmatian, M., Sedaghati, R., and Rakheja, S. (2020). “Dynamic characterization of isotropic and anisotropic magnetorheological elastomers in the oscillatory squeeze mode superimposed on large static pre-strain.” *Compos. Part B Eng.*, 182, 107648.

Wan, Y., Xiong, Y., and Zhang, S. (2019). “Temperature effect on viscoelastic properties of anisotropic magnetorheological elastomers under compression.” *Smart Mater. Struct.*, 28(1).

Wang, M.-J. (1998). “Effect of Polymer-Filler and Filler-Filler Interactions on Dynamic Properties of Filled Vulcanizates.” *Rubber Chem. Technol.*, 71(3), 520–589.

Wang, Y., Hu, Y., Chen, L., Gong, X., Jiang, W., Zhang, P., and Chen, Z. (2006). “Effects of rubber/magnetic particle interactions on the performance of magnetorheological elastomers.” *Polym. Test.*, 25(2), 262–267.

Wen, Q., Shen, L., Li, J., Xuan, S., Li, Z., Fan, X., Li, B., and Gong, X. (2020). “Temperature dependent magneto-mechanical properties of magnetorheological elastomers.” *J. Magn. Magn. Mater.*, 497(October 2019), 165998.

Xu, L., Zou, A., Fu, J., Yu, M., and Bai, J. (2018). “Development and simulation evaluation of a magnetorheological elastomer isolator for transformer vibration

control.” *Proc. 30th Chinese Control Decis. Conf. CCDC 2018*, 0(0), 2600–2604.

Xu, Z.-D., Xu, Y., Yang, Q., Xu, C., Xu, F., and Wang, C. (2017). “Tests and Modeling of a New Vibration Isolation and Suppression Device.” *J. Dyn. Syst. Meas. Control*, 139(12), 121011.

Yang, C. Y., Fu, J., Yu, M., Zheng, X., and Ju, B. X. (2015). “A new magnetorheological elastomer isolator in shear-compression mixed mode.” *J. Intell. Mater. Syst. Struct.*, 26(10), 1290–1300.

Yang, J., Gong, X., Deng, H., Qin, L., and Xuan, S. (2012). “Investigation on the mechanism of damping behavior of magnetorheological elastomers.” *Smart Mater. Struct.*, 21(12).

Yang, Z., Qin, C., Rao, Z., Ta, N., and Gong, X. (2014). “Design and analyses of axial semi-active dynamic vibration absorbers based on magnetorheological elastomers.” *J. Intell. Mater. Syst. Struct.*, 25(17), 2199–2207.

Yao, H., Wang, T., Wen, B., and Qiu, B. (2018). “A tunable dynamic vibration absorber for unbalanced rotor system.” *J. Mech. Sci. Technol.*, 32(4), 1519–1528.

Yarra, S., Gordaninejad, F., Behrooz, M., and Pekcan, G. (2019). “Performance of natural rubber and silicone-based magnetorheological elastomers under large-strain combined axial and shear loading.” *J. Intell. Mater. Syst. Struct.*, 30(2), 228–242.

Yarra, S., Gordaninejad, F., Behrooz, M., Pekcan, G., Itani, A. M., and Publicover, N. (2018). “Performance of a large-scale magnetorheological elastomer–based vibration isolator for highway bridges.” *J. Intell. Mater. Syst. Struct.*, 29(20), 3890–3901.

Zhang, X., Gong, X., Zhang, P., and Li, W. (2007). “Existence of Bound-Rubber in Magnetorheological Elastomers and Its Influence on Material Properties.” *Chinese J. Chem. Phys.*, 20(2), 173–179.

Zhu, J. T., Xu, Z. D., and Guo, Y. Q. (2012). “Magnetoviscoelasticity parametric model of an MR elastomer vibration mitigation device.” *Smart Mater. Struct.*, 21(7).

Zu, Q. H., Chen, Z. Y., Shi, W. K., Mao, Y., and Chen, Z. Y. (2015). “Torsional Vibration Semiactive Control of Drivetrain Based on Magnetorheological Fluid Dual Mass Flywheel.” *Math. Probl. Eng.*, 2015.

List of Publications based on PhD Research Work

Sl. No.	Title of the paper	Authors (in the same order as in the paper. Underline the Research Scholar's name)	Name of the Journal/ Conference, Vol., No., Pages	Month, Year of Publication	Category*
1.	A novel method for dynamic characterization of angular displacement-dependent viscoelastic properties of Magnetorheological Elastomer under torsional loading conditions	Praveen Shenoy, KV Gangadharan	Smart Materials and Structures, Volume 28, Number 7, 075034.	12 June 2019	1
2.	A novel approach to characterize the magnetic field and frequency dependent dynamic properties of magnetorheological elastomer for torsional loading conditions	K Praveen Shenoy, Umanath Poojary, KV Gangadharan	Journal of Magnetism and Magnetic Materials, 166169	18 November 2019	1
3.	Performance of magnetorheological elastomer based torsional vibration isolation system for dynamic loading conditions	K Praveen Shenoy, Abhishek Kumar Singh, K Sai Aditya Raman, KV Gangadharan	Journal of Central South University	Accepted (06-Nov-2019)	1
4.	Experimental investigation of torsional vibration isolation using Magneto Rheological Elastomer	K Praveen Shenoy, Abhishek Kumar Singh, K Sai Aditya Raman, KV Gangadharan	International Conference on Research in Mechanical Engineering Sciences, MATEC Web of Conferences, Volume 144, Art. No. 01007	09 January 2018	3

*Category: 1: Journal paper, full paper reviewed 2: Journal paper, Abstract reviews 3: Conference/Symposium paper, full paper reviewed
4:Conference/Symposium paper, abstract reviewed 5: others(including papers in Workshops, NITK Research Bulletins, Short notes etc.)

12/12/2019

Praveen Shenoy K

Research Scholar
Name & Signature, with Date

Dr. K V Gangadharan

Research Guide
Name & Signature, with Date